# Fabrication of 2D Materials via Novel Laser Treatment Processes and their Implementation in Optoelectronic Applications

by

Khaled Ibrahim

A thesis

presented to the University of Waterloo

in fulfilment of the

thesis requirement for the degree of

Doctor of Philosophy

in

Mechanical and Mechatronics Engineering

Waterloo, Ontario, Canada, 2020

## Examining Committee Membership

The following served on the Examining Committee for this thesis. The decision of the Examining Committee is by majority vote.

| | |
|---|---|
| External Examiner | Prof George Knopf |
| Supervisor(s) | Prof Mustafa Yavuz<br>Prof Kevin Musselman |
| Internal Member | Prof John Wen |
| Internal-external Member | Prof Joseph Sanderson<br>Prof Michael Pope |

## Author declaration

I hereby declare that I am the sole author of this thesis. This is a true copy of the thesis, including any required final revisions, as accepted by my examiners.

I understand that my thesis may be made electronically available to the public.

# Abstract

Pulsed laser treatment of 2D materials is becoming increasingly popular due to the simple and efficient nature of the treatment process. In this thesis, the femtosecond laser treatment methods of 2D materials to fabricate functionalized particles and nanorods are proposed to deepen the understanding of how the femtosecond laser and the process parameters can be tuned to yield different chemical compositions and shapes, which in turn can fit different applications and devices.

A femtosecond laser process was developed to treat flakes of 2D materials (molybdenum disulfide ($MoS_2$), tungsten disulfide ($WS_2$), and boron nitride (BN) flakes) in an ethanol-containing solvent. The highly energetic laser pulses exfoliate and cleave the flakes into nanosheets with diameters of ≈3 nm and simultaneously dissociate the solvent molecules. The dissociated carbon and oxygen atoms from the solvent bond with the freshly cleaved 2D nanoparticles to satisfy edge sites, resulting in the formation of hybrid 2D nanoparticles that contain graphene-like carbon domains as well as the host material. Contrary to the current state of the art, where functionalization techniques can take several days to achieve, the hybrid nanoparticles are formed in as little as 20 min without toxic or corrosive chemicals and are multifunctional. Photoluminescence and absorption owing to both the carbon domains and the host 2D material ($MoS_2$, $WS_2$, or BN) are observed. This novel hybrid optical behavior makes these materials promising for emerging optoelectronic applications.

An adaptive recipe was consequently developed to fabricate halogenated graphene particles, aiming to address the main challenge facing large-scale commercialization of perovskite solar cells: their instability and degradation from humidity. The current state of the art studies discussing the implementation of 2D materials in perovskite solar cells to enhance their stability are limited and lack discussion about long-term degradation and efficiency retention. Highly hydrophobic iodinated and chlorinated graphene particles were fabricated using femtosecond laser and incorporated into the hole transport layer and as an encapsulating layer. While the power conversion efficiency (PCE) was retained, the long-term stability was significantly enhanced for the cells containing the graphene in both ambient conditions and highly humid conditions, in test spans of 2200 hrs and 50 hrs, respectively.

The previously unrealized ability to grow nanorods and nanotubes of 2D materials using femtosecond laser irradiation is demonstrated. In as little as 20 min, nanorods of tungsten disulfide, molybdenum disulfide, graphene, and boron nitride are grown in solutions. The technique fragments nanoparticles of the 2D materials from bulk flakes and leverages molecular-scale alignment by nonresonant intense laser pulses to direct their assembly into nanorods up to several micrometers in length. The laser treatment process is found to induce phase transformations in some of the materials, and also results in the modification of the nanorods with functional groups from the solvent atoms. Notably, the $WS_2$ nanoparticles, which are ablated from semiconducting 2H $WS_2$ crystallographic phase flakes, reassemble into nanorods consisting of the 1T metallic phase. Due to this transition, and the 1D nature of the fabricated nanorods, the $WS_2$ nanorods display substantial improvements in electrical conductivity and optical transparency when employed as transparent conductors.

## Acknowledgements

Primarily, I would like to thank Professor Kevin Musselman for everything you taught me, including how to properly write a scientific communication for impactful publication; your accessibility to me and all the team, and your willingness to make me grow, and allow me to make mistakes and learn from them. But more importantly, your work ethic, professionalism, and attentiveness have all inspired me to be a better version of myself. You are a true role model. I would also like to thank Professor Mustafa Yavuz for allowing me to accomplish my dreams here at the University of Waterloo, and for your generosity in giving me advice within the realm of my work. More importantly, thank you for the small life lessons you always gave me from your life experiences; these will remain with me.

I am very thankful to the teammates in my research group across the years since joined in 2013, especially Kissan Mistry and Ahmed Shahin. You brought knowledge, a strong work ethic, and crucial collaborative qualities to my experience as a graduate student. But more importantly, you have brought lifelong friendships; I am sure of this.

I would like to thank my funding sources—NSERC, WIN, and the Tyler Lewis Foundation—for believing in me. Their financial aid certainly played a large role in the success of the projects discussed in this thesis.

My degree wouldn’t have been completed without my friends and family. My lifelong friends from high school have my back to this day. And my aunts, uncles, and cousins have been a constant source of encouragement and have always expressed their pride in what I am doing, picking me up and helping me get through the hard times. To my lifelong friends Omar Mohy, Nouran Sabry, and their families, I am thankful for your continuous support; your true friendship was a sense of security and home for me throughout. Mohab Ahmed, my companion on this trip to learn away from home, our brotherhood has made the homesickness much easier. May Nagy, thank you for being my mentor and listening to me whenever I needed your support. Menna Khattab, your role in this is not to be forgotten nor understated. You stood by me through thick and thin, and I am thankful for your role in my journey.

Most importantly, I thank my family. My sister, Haia Ibrahim, has always inspired me with her big heart, her intelligence, and her care for me on this journey away from home. To my father, Mohamed Hussein Ibrahim, thank you for always being my rock, backbone, and constant well of support and encouragement. You never fail to provide emotional and physical support, and your generosity is a fundamental reason that I am here today. Finally, a massive thank you to my mother, Lolwa Farag, the strongest woman I have ever met, and the person who has sacrificed so much for me to be in this position today. So thank you is not enough, but I am forever in your debt.

## Dedication

To my late grandmother. Your prophecy when I was 12 years old, that I was going to become a doctor is on the verge of happening! I am sure you are looking down proud of this achievement.

# Table of Contents

**List of Figures**

## List of Tables

## List of abbreviations

- TMD: transition metal dichalcogenides
- $MoS_2$: molybdenum disulfide
- $WS_2$: tungsten disulfide
- BN: boron nitride
- PG: pristine graphene
- GO: graphene oxide
- NGO: nitrogen-doped graphene
- spiro-OMeTAD: tetrakis[N,N-di(4-methoxyphenyl)amino]-9,9′-spirobifluorene
- $TiO_2$: titanium oxide
- ETL: electron transport layer
- HTL: hole transport layer
- FTO: fluorine-doped tin oxide
- Cl-G: chlorinated graphene
- I-G: iodinated graphene
- SEM: scanning electron microscopy
- TEM: transmission electron microscopy
- AFM: atomic force microscopy
- XPS: X-ray photoelectron spectroscopy
- XRD: X-ray diffraction
- Abs: absorbance
- PL: photoluminescence
- PSC: perovskite solar cell
- PCE: power conversion efficiency
- FF: fill factor
- Voc: open circuit voltage
- Jsc: short circuit current
- CVD: chemical vapor deposition
- a.u: arbitrary unit

# 1.0 – Introduction

---

---

## 1.1 – Introduction to 2D materials and their significance

### 1.1.1 – Graphene and its properties

Graphene is a single-layer, 2D, one atom thick (~ 0.345 nm) material consisting of a honeycomb lattice of sp2 bonded carbon atoms[1]. It is one form of carbon allotrope (shown in Figure 1.1), a group that includes charcoal, graphite, and fullerenes. Since Novoselov's et al. success in isolating mono-layered graphene from graphite flakes in 2004[2], graphene has been the subject of intense research by material scientists. Novoselov's colleague Geim defined "isolated or free-standing graphene" as follows: "graphene is a single atomic plane of graphite[3], which is sufficiently isolated from its environment to be considered free-standing". Graphene exhibits unique and novel physiochemical properties, namely, high fracture toughness, thermal conductivity, Young's modulus, and electrical conductivity[3,4]. These remarkable properties endow graphene with extraordinary properties, such as high mechanical strength and high electrical conductivity. Hence, graphene nano-sheets have rapidly been adapted for a wide variety of applications, including energy storage materials, nano-devices, renewable energy technology, polymer composites, and sensing applications [5–7].

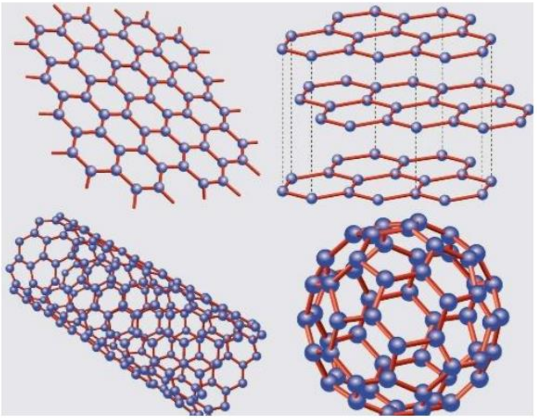

Figure 1.1 – Schematic of graphene structure (top left), graphite (top right), carbon nano-tubes (bottom left), and bucky balls (bottom right). Blue balls representing carbon atoms, red connections representing covalent bonds. Reproduced with permission from Neto et al. Drawing conclusions from graphene. *Phys. World* **19**, 33, (2006). Copyright 2006 IOP[8].

Many researchers have been trying to establish methods of graphene fabrication on a large scale dating back to 2004, thus attempts such as epitaxial growth on non-metallic substrates[9] and chemical vapor deposition techniques (CVD)[10] have been established. There are many ways for single layer and multilayer graphene fabrication such as micro mechanical cleavage, CVD on metallic substrate, intercalation of graphite and graphene oxide single layer reduction, comprising of chemical reduction of exfoliated graphene oxide, arc discharge and thermal exfoliation of graphite oxide[11].

Graphene sheets can be fabricated via the scotch tape method, which yields flat stacked graphene sheets as a result of cleavage of graphite[2]. Due to graphene sheets high specific area (atomic density per unit area), it sometimes tends to re-stack and form irreversible bulk graphite as a result of van der Waals interaction between the graphene sheets. Graphene has been prepared using chemical processes such as graphite oxidation, chemical exfoliation and reduction, given its low cost and large scale fabrication ability[12].

Due to its extraordinary electrical and mechanical properties such as large surface-to-volume ratio[13], large carrier mobility (surpassing 20000 $cm^2\ V^{-1}s^{-1}$), high thermal conductivity, high mechanical strength (e.g. 200 times greater than steel)[14,15] and tensile modulus of 1 TPa[16,17], graphene becomes a material of great interest to optoelectronic, MEMS and NEMS applications.

Excellent electrical conductivity is key for sensing applications, given its extremely high electron speed attributed to the absence of a band gap. Carbon has 6 electrons with 2 electrons in the inner shell, and 4 electrons on the outer shell. In a typical situation, an individual carbon atom usually offers its four electrons of the outer shell for bonding. On the contrary, Carbon atoms in graphene are connected to three other carbon atoms on a 2-dimensional plane in a very strong covalent bond also known as the sigma bond, hence leaving a lone electron on the third dimension performing an electronic conduction role. These freely available electrons are called π electrons that are located on the z-axis, thus orbiting above and below the graphene sheet as schematically shown in Figure 1.2. The π electrons consequently overlap with neighbouring lone electrons on the sample plane forming the pi-bond. Effectively, the bonding and anti-bonding of these lone electrons dictate the electronic properties of graphene.

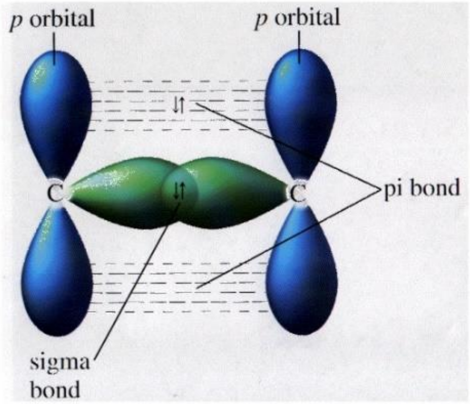

Figure 1.2 – Schematic of sigma and the overlapping pi bonding of carbon atoms. Reproduced with permission from Yang et al. Structure of graphene and its disorders: a review. *Sci. Technol. Adv. Mater.* **19**, 613–648 (2018). Copyrights 2018 Wiley-VCH[18].

### 1.1.2 – Transition metal dichalcogenides and their properties

After its discovery in 2004 by Novolesev and Geim[2], graphene has hugely impacted several scientific fields. This success ignited interest in other two-dimensional nanomaterials, including hexagonal boron nitride (h-BN), graphitic carbon nitride (g-$C_3N_4$), monoatomic buckled crystals (phosphorene), and transition metal dichalcogenides (TMD) including $MoS_2$, $MoSe_2$, $WS_2$, and $WSe_2$. TMD materials consist of a hexagonal layer of transition metal atoms (M) sandwiched between two layers of chalcogen atoms (X) and represent a stoichiometry of $MX_2$.

These materials are all known for the strong covalent intralayer bonding and weak van der Waals interlayer forces in the bulk form making them easy to exfoliate and isolate. In the 2D monolayer form however, they tend to exhibit a high degree of stability and hence illustrate distinct properties compared to that of their bulk counterparts. TMD materials for instance, exhibit an indirect gap in their bulk, few layers and even bi-layer forms, however they remarkably transition to direct bandgap materials in their monolayer forms due to the electron-hole interlayer coupling effect[19]. Despite the relative similarity in crystallographic 2D structure, these materials cover a wide range of electronic, optical, catalytic, chemical, thermal, and magnetic properties, presenting a diverse and powerful arsenal for a plethora of applications in numerous fields.

Boron nitride has also garnered significant attention due to its potential use and applications in catalysts, optoelectronics, and semiconductor devices. Unlike TMD materials, BN consists of a single atomic-thick layer of boron and nitrogen atoms covalently bonded together. Shown below in Figure 1.3 is a comparison between the atomic structure of a TMD and hexagonal-boron nitride. The layered structure exhibits attractive features such as high dielectric properties, high thermal conductivity, good chemical and thermal stability, and unique optical properties. Surprisingly, BN has similar mechanical strength and thermal conductivity as graphite. However, their optical properties differ greatly as graphene is a zero-bandgap material while BN is a large bandgap insulator (5.8 eV).

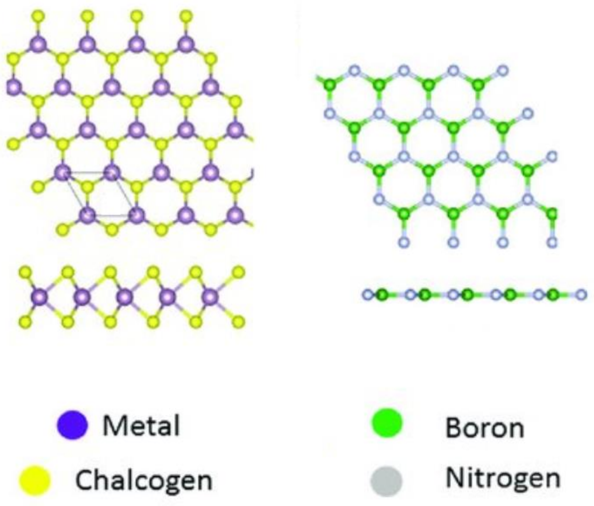

Figure 1.3 – Crystal structures of (left) a transition metal dichalcogenide, and (right) boron nitride. Reproduced Reproduced with permission from Laturia et al. Dielectric properties of hexagonal boron nitride and transition metal dichalcogenides: from monolayer to bulk. *npj 2D Mater. Appl.* **2**, 6 (2018). Copyrights 2018 Nature[20].

Versatility is a key benefit of 2D materials. They are suitable in a wide array of applications. 2D materials can be utilized as a film (e.g., in field-effect transistors), in powder form (e.g., as additive in batteries[21]), as nanoparticles (e.g., in cancer treatment and bioimaging application), and as quantum dots in aqueous solution (e.g., used in nitrogen explosive sensing applications[22]).

As the lateral size of these materials is reduced (to typically below 20 nm), they illustrate enhanced and new properties arising from edge and quantum effects, while also maintaining the parent or inherent 2D properties. TMD materials also have indirect bandgap that turns into direct bandgap as the material becomes monolayer[23,24]. Also, compared to their 2D counterparts, these quantum dot materials have larger surface-to-volume ratios, better solubility in a variety of solvents, better suitability in numerous solution environments (particularly biological environments), highly tunable physiochemical properties, are more amenable to hybridization with other nanomaterials, and can be more easily doped and functionalized.

### 1.1.3 – Femtosecond laser treatment of 2D materials

Femtosecond lasers are commonly used in numerous applications including bio, aerospace, research, and energy in recent years. Cataract surgeries for patients with eyesight issues are amongst the most popular use of femtosecond lasers. The main mechanism for femtosecond laser treatment and surface modification is the application of a multiphoton phenomenon. Femtosecond laser treatment is advantageous because the short pulse width is faster than the electron heat conduction time making it a nonthermal process, highly useful for the above applications[25]. Also, the nonthermal nature of the process paves the way to pure photo induced chemical reactions. This type of laser treatment can produce extremely uniform periodic structures in both micro and nanoscale with minimum defects and discrepancies.

Several techniques using a femtosecond laser were implemented to treat 2D materials, specifically graphene and its derivatives. Since its discovery in 2004, the femtosecond laser was the main photo-treatment tool. Methods included laser induced reduction of thermally and electrically insulating oxygen functional groups and the formation of more conductive graphene domains, making the material more viable for microelectronics and as a channel material for various devices. Shown below in Figure 1.4 are laser treated graphene oxide aimed to reduce the oxygen functional groups.

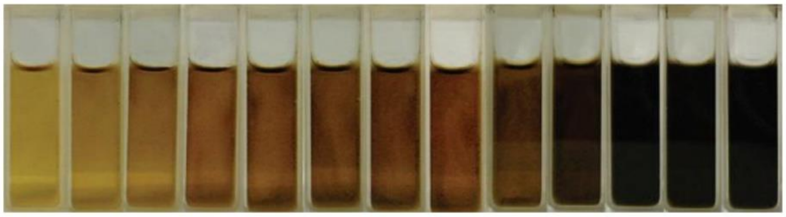

Figure 1.4 – The graphene oxide (GO) solution color changes from pale-yellow towards black. Images are captured every 5 min laser treatment interval. Reproduced with permission from Wu et al. Production of reduced graphene oxide by UV irradiation. *J. Nanosci. Nanotechnol.* **11**, 10078–10081 (2011). Copyrights 2011 American Scientific Publishers[26].

Laser treatment is also used for patterning and writing on graphene layers, forming conductive circuits and functional devices in photo reduced graphene oxide, CVD graphene and graphene bilayers[27–29]. Examples of the laser treated graphene are shown below in Figure 1.5.

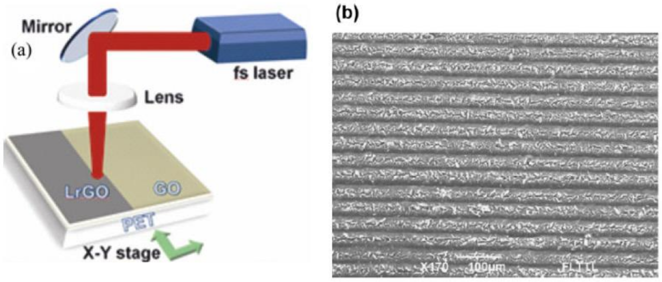

Figure 1.5 – (a) Setup for femtosecond laser treatment[30], (b) SEM pictures of laser-modified GO coating. Laser power – 50mW, scanning speed – 100 mm/s. Reproduced with permission from Trusovas, R. *et al.* Reduction of graphite oxide to graphene with laser irradiation. *Carbon N. Y.* **52**, 574–582 (2013). Copyrights 2013 El Sevier[31].

Alongside oxygen reduction, patterning, and writing; using the laser's high intensity to break flakes and nanosheets is common for fabrication of quantum dots and nanoparticles as illustrated previously[32,33]. The breakage of the graphene flakes into particles primarily happens as a result of the Coulomb explosion phenomenon. Coulomb explosion occurs when the intense field of a laser removes many electrons from the treated molecules upon interaction, resulting in the elements of the molecules becoming increasingly ionized[34]. The ionized elements (that are effectively in close proximity) then Coulomb repel[35]. During the laser pulse time span the ionized cluster of elements then extracts additional energy from the laser pulse until the Coulombic repulsive forces amid the highly charged ionized elements surpass its total cohesive energy, the cluster explodes, resulting in a sea of charged atomic ions with large kinetic energy and energetic electrons.

Coulomb explosion of atomic and molecular clusters is commonly reported to result from intensity ranges that vary from $10^9$ to $10^{20}$ W/cm$^2$, a wide wavelength range, and using laser pulses of varying pulse duration, such as nanosecond, picosecond, and femtosecond. However, the effectiveness of Coulomb explosion phenomenon is more prominent for ultrashort laser pulses of duration ≤100 fs[34].

## 1.2 – Functional two-dimensional nanoparticles

In addition to graphene, 2D materials such as $MoS_2$, $WS_2$, and BN have been produced in nanoscale form (i.e., thickness or lateral dimensions on the nanoscale, or both). Functionalization of these 2D nanomaterials is of interest for many applications in sensing[36] biomedicine[37,38], tribology[39], and photonics[40], among others. Significant progress has been made recently in fabricating and functionalizing 2D nanosheets of transition metal dichalcogenides[41]. This progress has focused on the functionalization of mono- or few-layer nanosheets with lateral dimensions greater than 100 nm by combining chemical exfoliation[42–46], micromechanical exfoliation[47], or liquid exfoliation[48] with the reaction of functionalities. The formation and functionalization of smaller 2D nanoparticles or quantum dots, on the other hand, is still in its infancy. Functionalization of these 2D nanoparticles is important because it provides the respective application the benefits of both materials making for added useful properties. In this thesis, a femtosecond laser technique will be developed for the simultaneous fabrication and functionalization of 2D nanoparticles. Laser-based procedures are particularly favorable due to the Coulomb explosion phenomenon that the laser incurs when interacting with materials. The laser focal point interacts with the 2D untreated flakes and the solvent molecules where a multiphoton-absorption ionization phenomenon occurs. The lasers intense electric field extricates the electrons from the molecule cluster, resulting in the constituents of the cluster to become highly ionized giving them a mutually repulsive state. Effectively breaking the bonds in a phenomenon known as Coulomb explosion.

## 1.3 – Two dimensional nanorods and rod-like geometry

1D nanostructures such as nano-wires, -tubes, -rods, and -fibers, have garnered great attention due to their excellent electrical, thermal, mechanical, and optical properties and their suitability in a myriad of applications and devices. Applications of 1D nanostructures exist in solar cells[49,50], LEDs[51], chemical sensors[52], transparent conducting films (TCFs), and heaters[53] to name a few.

TCFs, for example, require high conductivity and transparency thus connected networks of 1D nanomaterials[53] have been studied as a viable alternative to thin films of Indium Tin oxide, which suffer from drawbacks such as brittleness and indium scarcity[54]. Materials such as graphene and transition metal dichalcogenides (TMDs) exhibit excellent electrical properties due to their “flat” 2D chemical structure. Sheets or flakes of these materials can allow for large area coverage with high conductivity but typically at the expense of transparency[55,56]. An approach to improving transparency is utilizing these materials in 1D nanorod-like structures. Carbon nanotubes (CNTs) are the most popular 1D variant of graphene and have been utilized to form large area conducting films, although challenges remain with respect to their purification[57,58] and aggregation. In this work, a femtosecond laser technique will be developed for the synthesis of 2D nanorods, which are then employed in TCFs.

## 1.4 – Perovskite solar cells

With global warming and climate change effects currently being observed around the world, and the rising global energy consumption of fossil fuel-based energy resources, the use of clean and renewable energy resources is becoming a pressing need for development of human society. Solar energy being the most abundant energy resource, makes solar cells of all types of great interest.

Hybrid solar cells based on organic-inorganic metal halide perovskite (e.g. $CH_3NH_3PbI_3$) materials have garnered significant attention in recent years. The perovskite materials are used in numerous applications but primarily have been used as active absorbing layers in perovskite-based solar cells (PSC) due to their suitable properties such as their high extinction coefficient, high charge mobility, long carrier lifetime, and long carrier diffusion distance. The power conversion efficiency (PCE) of the PSC has increased from 3.8% to 22.1% from 2009 to 2016[59] making them a stronger generation of low-cost solar cells that could potential replace or augment traditional silicon solar cells.

The PSC working principle depends on the active layer (perovskite) initially absorbing sunlight photons and producing electron-hole pairs. The electron-hole pairs can either recombine to produce light or wasted hear or can be separated to generate current. However due to the intrinsic low carrier recombination probability of the perovskite material and higher carrier mobility, the lifetime of the respective carriers is long[60]. These properties make the PSC amongst the highest performing solar cells in the current state of the art.

The free electrons are then picked up by an electron transport layer (ETL) and the generated holes are collected by the hole transport layer (HTL) before being collected eventually by their respective electrodes. Finally, the fluorine-doped tin oxide (FTO) and metal electrode are connected, and the photocurrent is generated in the outer circuit. The PSC working principle is illustrated in the Figure 1.6.

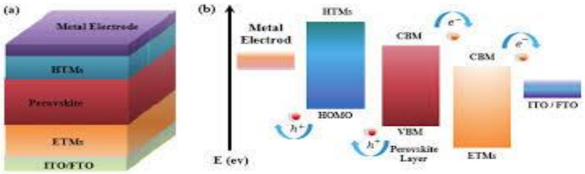

Figure 1.6 – (a) A schematic illustration of perovskite device structure, (b) Energy band diagram of PSC. Reproduced with permission from Suhaimi, S. *et al.* Critical analysis of stability and performance of organometal halide perovskite solar cells via various fabrication method (Review). *EPJ Web Conf.* **162**, (2017).Copyrights 2017 EPJ [61].

## 1.5 – Problem statement

Current state of the art techniques for the functionalization of 2D materials fail to address the effect the solvent plays on laser-based techniques (or any wet process). Examining the effect of the solvent on the produced particles is paramount for understanding the particles' solubility in various solvents, which is crucial for bio applications. The techniques presented in section 2.1 take several days to accomplish and often necessitate toxic solvents and elevated temperatures.

Despite the attention PSCs have garnered due to their rapidly rising PCE, they still face major obstacles before being commonly used industrially, namely hysteresis[62,63], light soaking[64], metal electrode migration[65–67], and long-term stability[68–71]. Hybrid organic–inorganic perovskite materials are very susceptible to moisture and humid environments because of their chemical composition. The solubility of lead salts in ambient conditions is considered the key reason for their degradation under moisture[72,73]. Additional factors, including phase transition[74,75] and thermal decomposition[76,77], may also be significant factors that affect the lifetime and stability of PSCs. Consequently, the stability of PSCs compared to other PV technologies is a major limitation. Research on efficient strategies for improving the moisture stability of PSCs is ongoing.

The intrinsic black color of the $CH_3NH_3PbI_3$ perovskite film becomes yellow due to the decomposition of $CH_3NH_3PbI_3$ into $PbI_2$, $CH_3NH_2$, and HI; see equation (1.1)[78], where this process is primarily a consequence of a humid environment.

$$CH_3NH_3PbI_3(s) + 4\ PbI_2(s) + MAI(aq.) \longleftrightarrow 4\ PbI_2(s) + CH_3NH_2(aq.) + HI(aq.) \quad (1.1)$$

In this thesis the susceptibility of PSC to moisture and ambient condition will be the primary focus. Where functionalized graphene nanoparticles are employed to improve the moisture long term stability of perovskite solar cells.

Fabrication techniques for nanorods as previewed in section 2.3.2 are lengthy, requiring as many as 147 hours. The hydrothermal technique is the most common for fabricating 2D nanorods, which typically involves elevated temperatures and toxic chemicals. Thus, a simpler procedure that can be done at room temperature procedure is preferable.

# 2.0 – Literature Review

## Synopsis

This section reviews the current state-of-the-art that acts as a basis for the studies implemented in chapters 3, 4, and 5. Section 2.1 will review hybrid 2D nanoparticles and the different mechanisms to functionalize and dope the host 2D materials. Section 2.2 covers the incorporation of 2D materials in perovskite solar cells and their effect on increasing the stability and efficiency of the perovskite solar cells. Finally, section 2.3, sheds light on the current state-of-the-art methods to fabricate 2D nanorods.

## 2.1 – Functionalization of 2D materials

### 2.1.1 – Methods for 2D nanoparticle functionalization and doping

The importance of fabricating 2D nanoparticles and their hybrid derivatives, as discussed in section 1.2 and 1.3, mainly lies in the resultant nanoparticle comprising the properties of both the host and the dopant material. Fabrication methods include hydrothermal, microwave, and exfoliation-based methods amongst others, most of which are extremely time consuming, multi-step procedures, and require the use of numerous chemicals, hence making them expensive procedures that produce significant amounts of waste. Materials of interest for the study conducted in Chapter 3.0 include molybdenum disulfide, tungsten disulfide, and boron nitride. Therefore, in this section the most note-worthy works that discuss functionalization of these materials are reviewed.

A study conducted by Haldar et al. focused on fabrication of functionalized $MoS_2$ quantum dots that are employed to detect nitro-explosives[22]. A bottom-up approach was employed where ammonium molybdate tetrahydrate $(NH_4)_6Mo_7O_{24}$-$4H_2O$ (molybdenum source) was mixed with deionized water and $Na_2S$ as the sulfur source. A transmission electron microscope (TEM) image of the particles can be observed in Figure 2.1. The particle size was found to be 5 nm making the photoluminescence (PL) emission easily fine-tuned from 423 nm to 370 nm, which is close to the absorption band of the nitro explosive analyzed in this study (trinitrophenol, TNP).

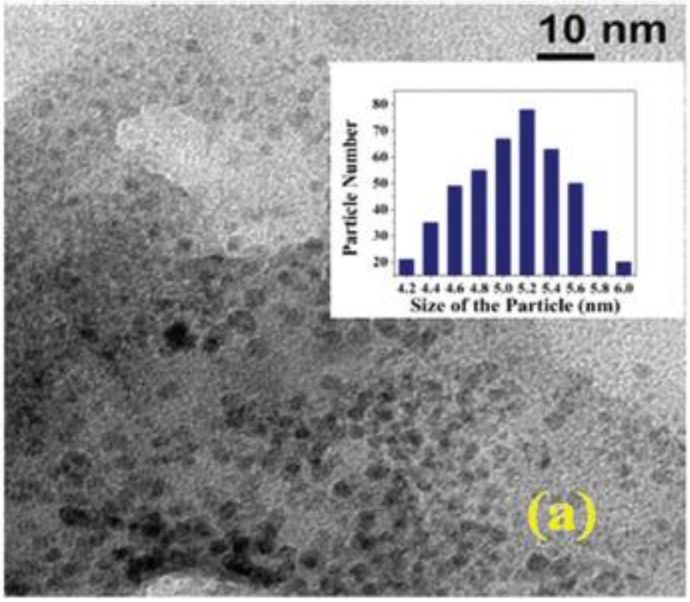

Figure 2.1 – TEM image of the fabricated diaminobutane-functionalized $MoS_2$ quantum dots. Inset shows histogram of particle size distribution. Reproduced with permission from Haldar et al. High selectivity in water soluble $MoS_2$ quantum dots for sensing nitro explosives. *J. Mater. Chem. C* **4**, 6321–6326 (2016). Copyrights 2016 RSC[22].

The fabricated quantum dots' selectivity and PL emission quenching was assessed due to an energy transfer process, which was indicative of successful sensing of nitro-explosives. A considerable 90% quenching of the PL peak was observed after TNP was added to the solution as seen in Figure 2.2 (a). Other nitro compounds including 2,6-DNT; 2-NT; 4-NT; 1,3-DNB; 1,2-DNB; 1,4-DNB, and NB did not show the same fluorescence quenching ability as the explosive nitro aromatic compounds, as illustrated in Figure 2.2 (b).

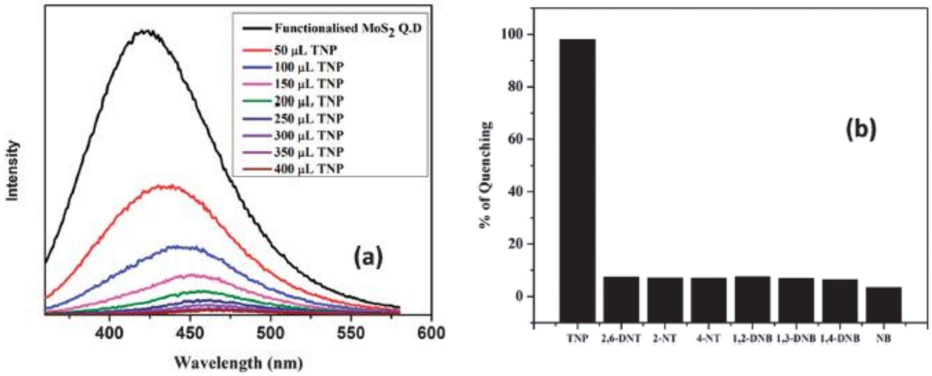

Figure 2.2 – (a) PL emission spectra of diaminobutane-functionalized $MoS_2$ quantum dots, and spectra shown after the addition of TNP illustrating sizeable quenching effect due to energy transfer. (b) Quenching effect percentage comparison between TNP and other nitro compounds Reproduced with permission from Haldar et al. High selectivity in water soluble $MoS_2$ quantum dots for sensing nitro explosives. *J. Mater. Chem. C* **4**, 6321–6326 (2016). Copyrights 2016 RSC[22].

Transition metal dichalcogenides (TMD) semiconductor materials are known to possess large surface-to-volume ratio and therefore offer exceptional capability for surface modification and functionalization that can result in charge transfer to and from the 2D layered material. The attachment of foreign noble metal atoms or adatoms can be considered an efficient way of doping 2D TMD materials, as these metals are resistant to environmental corrosion and oxidation. Doping opens a wide array of potential applications, especially gas sensing and bio sensing applications, as illustrated previously using graphene nanotubes and nanowires[79].

Sarkar et al. focused on the effect of noble metal (Au, Ag, Pd, Pt) nanoparticle doping with $MoS_2$ sheets[80]. The $MoS_2$ flakes were obtained using the micro mechanical exfoliation technique that included prolonged periods of ultrasonication, and the metallic nanoparticles were incorporated by means of electron beam deposition. Because electrical measurements are efficient at calculating the effect of doping on semiconducting materials, field-effect transistors (FETs) were fabricated on top of the doped flakes with 20/100 nm Ni/Au pads as the source and drain. A schematic of the doped flake in a FET setup is shown in Figure 2.3 (a). Pt, Pd and Au were found to exhibit the highest doping with $MoS_2$ and were also very stable.

Raman spectroscopy revealed that both the $A_{1g}$ and $E^1_{2g}$ vibration modes (which are characteristic of $MoS_2$) were blue shifted, which indicates p-type doping of the $MoS_2$ flakes by the metal nanoparticles, as shown in Figure 2.3 (b). It was shown in this study that increasing the dose of nanoparticles affects the doping intensity, and that crucially the doping effect increases as the thickness of the transition metal dichalcogenides diminishes.

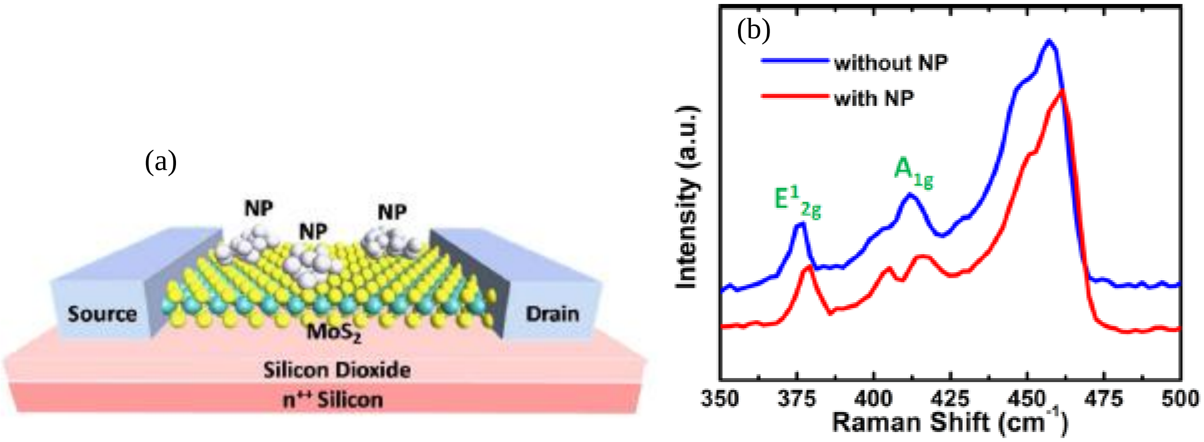

Figure 2.3 – (a) Schematic of the doped $MoS_2$ flake with metallic nanoparticles in the FET setup. (b) Raman spectra of $MoS_2$ flake before and after doping with metallic nanoparticles. Indicating p-type doping. Reproduced with permission from Sarkar, D. *et al.* Functionalization of transition metal dichalcogenides with metallic nanoparticles: Implications for doping and gas-sensing. *Nano Lett.* **15**, 2852–2862 (2015). Copyrights 2015 American Chemical Society[80].

To inspect the sensing ability, a FET using a pure $MoS_2$ flake and a FET using $MoS_2$ doped with Pd were exposed to a flow of hydrogen gas. As observed below in the time vs current curves (Figure 2.4), the $MoS_2$ without metallic nanoparticle doping did not illustrate any change in current as a result of the hydrogen flow, which was applied from 20 mins onwards. On the other hand, the doped flake was exposed to a similar hydrogen stream at 45 mins onwards and a substantial increase in current (from 0.2 μA to about 1.2 μA) was observed.

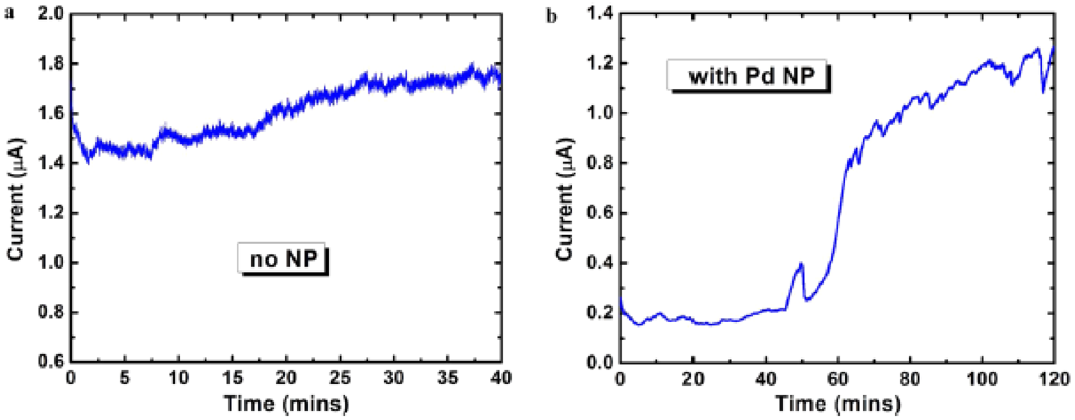

Figure 2.4 – Real-time current vs time measurements. (a) $MoS_2$ based FET without doped metallic nanoparticles. Thickness of $MoS_2$ flake is approximately 8 nm. Insignificant effect on the current is observed when the device was exposed to the hydrogen gas flow (20 min onwards). (b) Same $MoS_2$ FET after incorporation of Pd metallic nanoparticles Reproduced with permission from Sarkar, D. *et al.* Functionalization of transition metal dichalcogenides with metallic nanoparticles: Implications for doping and gas-sensing. *Nano Lett.* **15**, 2852–2862 (2015). Copyrights 2015 American Chemical Society[80].

It is common for 2D materials to bond and be chemically modified at defect sites and edge locations due to the ease of electron transfer at these sites. However, a study conducted by Voiry et al.[42] focused on defect-free functionalization of $MoS_2$. The functionalization mechanism in this case was instead facilitated by electron transfer between the 1T electron-rich metallic crystallographic phase and an organohalide. This causes functional groups to be covalently bonded to the chalcogen atoms in the transition metal dichalcogenide structure. In this study, covalent functionalization of chemically exfoliated transition metal dichalcogenides ($MoS_2$, $WS_2$ and $MoSe_2$) was of interest. These TMD bulk powders were chemically treated under argon. The functionalization was accomplished by adding Iodoacetamide to the exfoliated TMD nanoflakes suspended in the water solution.

Voiry et al. proved the covalent functionalization by observing the X-Ray Photoelectron Spectroscopy (XPS) spectra. In the $MoS_2$ and $MoSe_2$, both S-C and Se-C bonds were observed. Emergence of a N1s peak was another significant indicator of the functionalization of the TMD flakes. The 2H vs 1T crystallographic arrangement played a crucial role in the PL emission of the functionalized 2D $MoS_2$ flakes. The 2 different crystallographic orientations are shown below in Figure 2.5 (a–b). In Figure 2.5 (c), it is seen that the PL emission of the 2H crystallographic orientation exhibited a strong peak at 1.8 eV, however the 1T crystallographic orientation displayed little PL emission. Remarkably, the 1T crystallographic orientation illustrated strong PL emission after functionalization, as evident in peaks at 1.6 eV and 1.9 eV. The peak at 1.9 eV was attributed to the shifted $MoS_2$ peak, while the peak at 1.6 eV was attributed to band-structure modification due to covalent functionalization. Some studies concluded that the PL emission peak at 1.6 eV could be attributed to defects in the monolayer[81], however that was found not to be the case after it was proved that varying the amount of functionalization results in modulation of that peak.

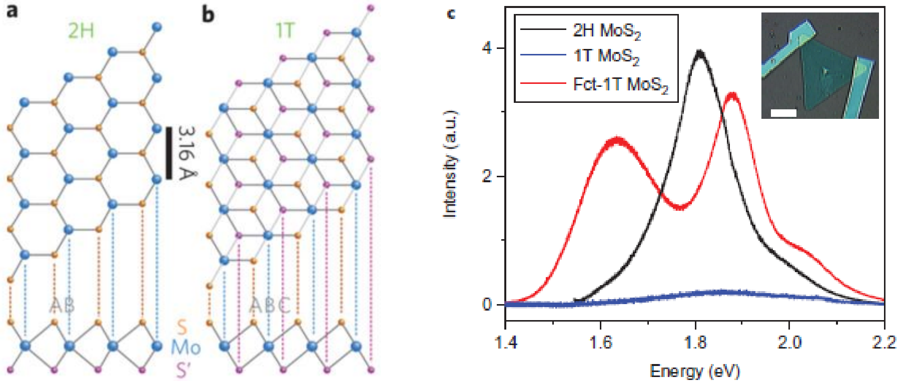

Figure 2.5 – (a) 2H and (b) 1T crystallographic orientation of TMD materials. (c) PL emission of 2H, 1T and functionalized 1T $MoS_2$. Reproduced with permission from Eda, G. *et al.* Photoluminescence from Chemically Exfoliated $MoS_2$. *Nano Lett.* **11**, 5111–5116 (2011). Copyrights 2011 American Chemical Society[82].

In 2015, Jiang et al. presented their work discussing fabrication of graphene- $MoS_2$ nanocomposites for photonic applications[83]. The graphene source was graphene oxide (GO) produced from graphite powder using a modified Hummers method that includes a mixture of $h_2so_4$, $NaNO_3$, and $KMnO_4$. The nanocomposite was fabricated using a hydrothermal method. 30 mL of brown color GO solution at 1 mg/mL concentration was prepared in an ultrasonication bath for 1 hour. 20 mL of cationic surfactant was then added to the resultant GO solution and stirred at room temperature for 12 hours to form a homogenous mixture. 20 mL of a mixture of 1.5 mmol $Na_2MoO_4 \cdot 2H_2O$ and 7.5 mmol L-cysteine were continuously stirred for 30 mins. This suspension was then moved to a 100 mL Teflon-lined stainless-steel autoclave where it was heat treated at 240°C for 24 hours before it was washed extensively with water and ethanol in order to collect the fabricated product using a centrifugation process. It was naturally cooled before drying in oven at 80°C for 12 hours. A black solid product was yielded, which was treated for 2 hours at 800°C with nitrogen flow to yield the $MoS_2$/graphene nanocomposite. An image of the graphene solution,

$MoS_2$ solution and the nanocomposite graphene/ $MoS_2$, is shown in Figure 2.6 (a), alongside the filtered nanocomposite particles.

In Figure 2.6 (b), TEM images have been captured for the nanocomposite where black stripes indicative of $MoS_2$ were observed amongst islands of graphene flakes. The electron diffraction pattern also revealed the distinct diffraction (100) and (110) owing to planes of graphene, while (100), (110), and (118) planes were also observed and attributable to $MoS_2$.

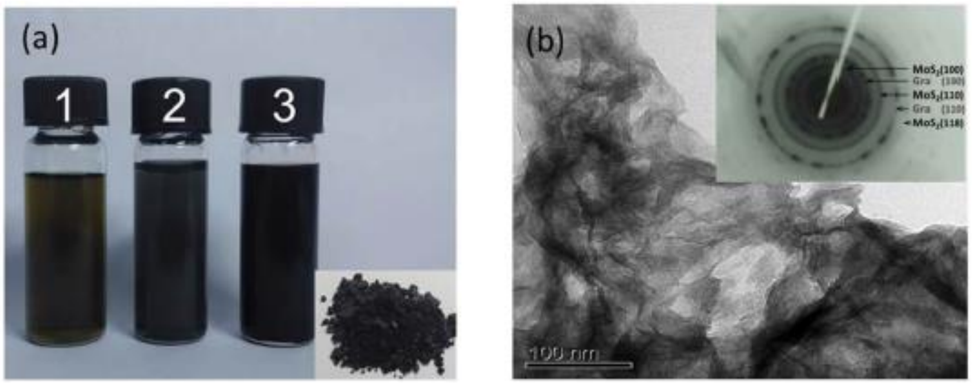

Figure 2.6 – (a) Images of the 1) graphene solution, 2) $MoS_2$ solution, and 3) nanocomposite of graphene and $MoS_2$. Inset shows nanocomposite particles before being suspended. (b) TEM image of nanocomposite and inset showing electron diffraction patternReproduced with permissions from Jiang, Y. *et al.* Broadband and enhanced nonlinear optical response of $MoS_2$/graphene nanocomposites for ultrafast photonics applications. *Sci. Rep.* **5**, 1–12 (2015). Copyrights 2015 Nature[83].

UV Visible spectroscopy measurements were performed to analyze the resultant solution from an optical standpoint. As shown below in Figure 2.7 (a), the graphene spectrum showed increased light absorption at higher energy (wavelengths shorter than 500nm) due to the intrinsic absorbance of graphene. The $MoS_2$ spectrum shows the characteristic $MoS_2$ peaks at 610 and 670 nm associated with the direct transition at the K point in the Brillouin zone. Crucially, the nanocomposite solution exhibited combinational spectral features, where characteristics of both spectra are observed, the direct transition at the K point of the $MoS_2$ Brillouin zone as well as the increased absorbance at the high energy spectral range, as seen below in Figure 2.7 (a).

Raman spectroscopy was carried out to investigate the vibration modes and to further verify the functionalization process. The Raman spectra shown in Figure 2.7 (b) show the three characteristic peaks owing to $MoS_2$ vibrations; namely $E^1_{2g}$, $A_{1g}$, and 2LA (M) situated at 380, 407, and 460 $cm^{-1}$ respectively. The $E^1_{2g}$ vibrational band results from the opposing vibrations of the two S atoms with respect to the Mo atom, whereas the $A_{1g}$ vibration is associated to the out-of-plane vibration and hence is in the opposite direction. The 2LA represents the second order longitudinal acoustic mode at the M point, which consequently indicates that $MoS_2$ structure is relatively homogenous. Also, the spectral distance between the $A_{1g}$ and $E^1_{2g}$ vibrational bands was 27 $cm^{-1}$, which suggests that the $MoS_2$ consists of a few layers. Crucially, the two peaks observed at 1342 $cm^{-1}$ and 1593 $cm^{-1}$, known as the D+G peaks (characteristic of graphene), indicate the presence of graphene domains embedded within the $MoS_2$ network.

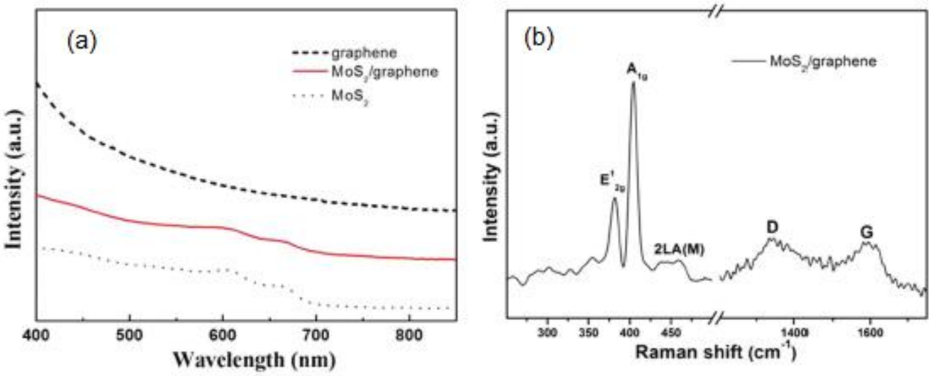

Figure 2.7 – (a) UV Visible spectra of graphene (black dashed line), $MoS_2$ black dotted line, and the $MoS_2$/graphene nanocomposite. (b) Raman spectrum of the $MoS_2$/graphene nanocompositeReproduced with permissions from Jiang, Y. *et al.* Broadband and enhanced nonlinear optical response of $MoS_2$/graphene nanocomposites for ultrafast photonics applications. *Sci. Rep.* **5**, 1–12 (2015). Copyrights 2015 Nature[83].

Graphene has been commonly used as an efficient electron acceptor, as it has proven its suitability in the role in numerous applications. In this scenario, the $MoS_2$/graphene nanocomposite consists of the covalent donor-acceptor structure. Knowing that the fermi-energy level of $MoS_2$ is higher than that of graphene, this makes $MoS_2$ a suitable electron donor by means of covalent bonding with graphene, facilitating the electron transfer process from $MoS_2$ to graphene. Figure 2.8 schematically illustrates the photo-induced electron transfer from $MoS_2$ to graphene upon photo excitation at 1.55 eV. Electrons are excited from the valence band to the conduction band, and due to the gapless bandgap of graphene and the indirect bandgap of multilayer $MoS_2$ (less than 1.48eV), the excited conduction band electrons are transferred in an efficient manner to graphene because of $MoS_2$'s slow excited state electron relaxation phenomena. This photo-induced electron transfer process disrupts and dominates the carrier relaxation process and hence significantly larger relaxation times were observed.

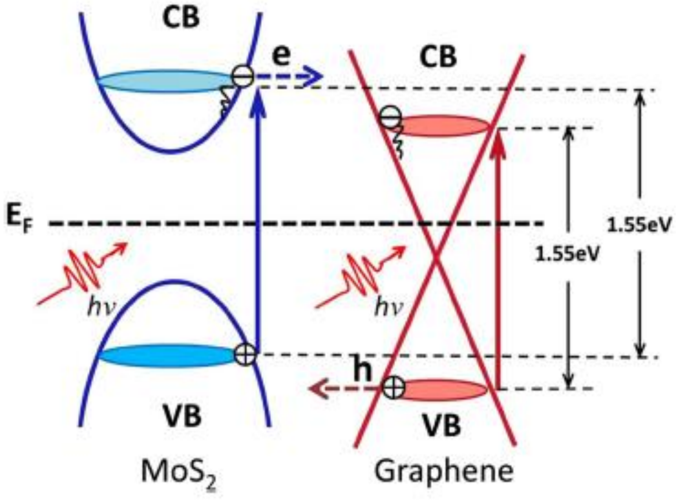

Figure 2.8 – Photo-induced electron transfer from $MoS_2$ to graphene upon photo excitation. Reproduced with permissions from Jiang, Y. *et al.* Broadband and enhanced nonlinear optical response of $MoS_2$/graphene nanocomposites for ultrafast photonics applications. *Sci. Rep.* **5**, 1–12 (2015). Copyrights 2015 Nature[83].

Studies concerning functionalization or the chemical modification of $WS_2$ nanoparticles are not abundant. However, Atkin et al. discussed the hybrid structures of $WS_2$/carbon dots with high photocatalytic activity[84]. The 2D $WS_2$ fabrication process employed included a two-solvent grinding/sonication technique that was previously reported by Carey et al[84]. To produce the hybrid material, the yielded solution was then mixed with citric acid, which serves in this study as the carbon source. The citric acid was added to a series of as-prepared 2D $WS_2$ nanoflake samples with varying concentrations including 0.05, 0.1, 0.5, 1, 5, 10, 50, 100, 500 and 1000 mM.

It was found that changing the citric acid content affected the carbon dot size, with 10 mM yielding carbon dots of 1 nm size, while the 1M citric acid concentration gave a favorable size of 5 nm, as seen in the TEM image in Figure 2.9 (a) below. Raman spectroscopy for the pristine 2D $WS_2$ revealed 2 peaks, namely the in-plane vibration $E^1_{2g}$ and out-of-plane $A_{1g}$ vibrational band located at 352.2 $cm^{-1}$ and 421.3 $cm^{-1}$ as shown below in Figure 2.9 (b). The hybrid materials however showed a slight shifting towards lower wavenumber by 0.8 $cm^{-1}$ and 0.5 $cm^{-1}$ respectively, which is indicative of $WS_2$ doping[85]. The Raman spectrum of the hybrid material also witnessed the emergence of extra peaks at 1330 $cm^{-1}$ and 1560 $cm^{-1}$, both attributable to D+G peaks of graphitic material. However, the D band in this material was found to be 80% of the G-band intensity, which suggests that the material present was graphene oxide.

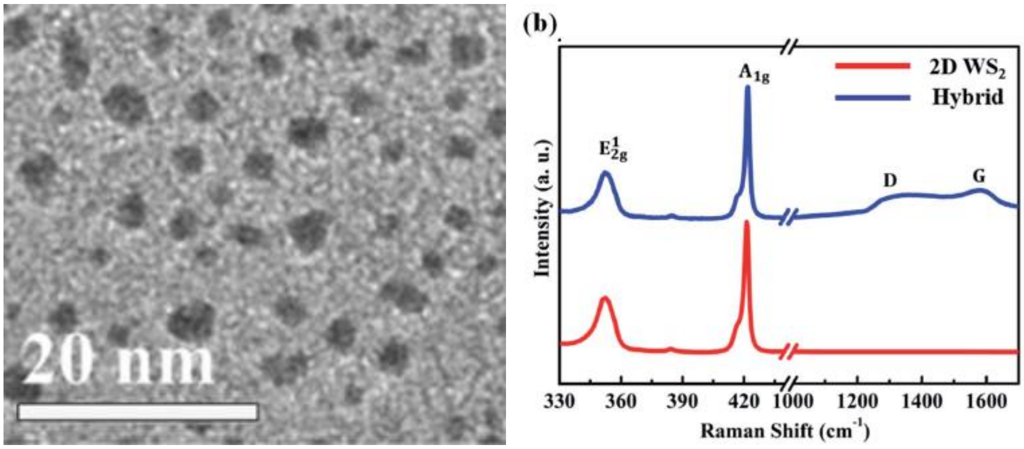

Figure 2.9 – (a) TEM image of the homogenously distributed carbon particles. (b) Raman spectra of both the pristine 2D $WS_2$ and the $WS_2$/carbon dot hybrid material. Reproduced with permission from Atkin, P. *et al.* 2D $WS_2$/carbon dot hybrids with enhanced photocatalytic activity. *J. Mater. Chem. A* **4**, 13563–13571 (2016). Coprights 2016 RSC[84].

The chemical composition of the hybrid materials was also assessed by XPS. From Figure 2.10(a) shown below, the W4f spectral range illustrated peaks situated at 33 eV, 35 eV, and 38 eV which correspond to W 4f 7/2, W 4f 5/2, and 5p 3/2 peaks, which are typical of 2D $WS_2$. These results indicated that the carbon dots are attached onto the 2D $WS_2$ by means of the weak van der Waal forces and electrostatic forces rather than by formation of any covalent bonding.

The optical properties of the pristine and hybrid $WS_2$/C dot materials were assessed using PL and UV visible spectroscopy. The PL emission did not show any differences between the pristine 2D $WS_2$ and the hybrid material, both indicating characteristic fluorescence of few-layered $WS_2$[86]. The UV visible spectra (Figure 2.10 (b)) showed a few distinct peaks at 633 nm, 525 nm, 460 nm, and 425 nm, which were attributed to the A, B, C and D excitonic peaks. Two low intensity peaks labelled E and F were also detected for the $WS_2$.

The absorbance was significantly different for the $WS_2$/carbon dot hybrid, as peaks E and F were suppressed greatly to the point of loss. This was attributed to the doping or addition of carbon, and electron transfer between $WS_2$ and carbon. Another peak located at 270 nm was observed for the $WS_2$ microwaved in the absence of citric acid.

This was identified as a plasmon peak due to the metallic nature of 2D $WS_2$ arising from surface defects. The peak at 270 nm became more prominent as the microwaving process increased the density of defects, however, after the hybrid material was formed the defects were reduced and the peak at 270 nm was quenched.

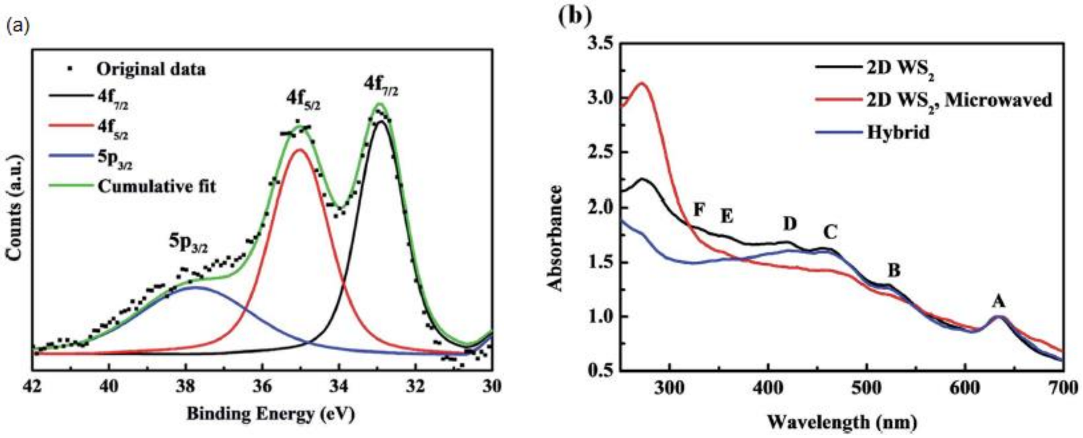

Figure 2.10 – (a) XPS spectra of the $WS_2$/C hybrid material. (b) UV visible spectra of 2D $WS_2$, Microwaved 2D $WS_2$ and hybrid material. Reproduced with permission from Atkin, P. *et al.* 2D $WS_2$/carbon dot hybrids with enhanced photocatalytic activity. *J. Mater. Chem. A* **4**, 13563–13571 (2016). Coprights 2016 RSC[84].

A common way to functionalize or chemically modify nanomaterials is inducing defects and exploiting these defects to bond with materials of interest. In some cases, materials are functionalized to perform a certain role. Jung et al.[37], for example, designed a defect-engineering method to synthesize blue-luminescent BN quantum dots with edge hydroxylation that were non-toxic, biocompatible, and well-suited for bioimaging applications. Figure 2.11 shows a schematic that illustrates the fabrication procedure. The fabrication procedure relied on purposely inflicted defects by means of heated iron nanoparticle impingement on the BN sheets. The impingement process and crack initiation are illustrated in Figure 2.11 (b–c). The sheets were mixed with iron ferrite nanoparticles in acetonitrile and were heated at 1000°C under nitrogen atmosphere, facilitating the presence of cracks and holes in the BN basal plane. It was found that the interaction between the BN sheets became weak and the microwave treatment shown in Figure 2.11 (d) was employed to propagate these cracks extensively, until eventually the BN had nanoscale dimensions. The residual iron nanoparticles were removed after completion of the impingement process using a magnet. Furthermore, the edge sites of the BN sheets were hydroxylated by means of water vapor exposure.

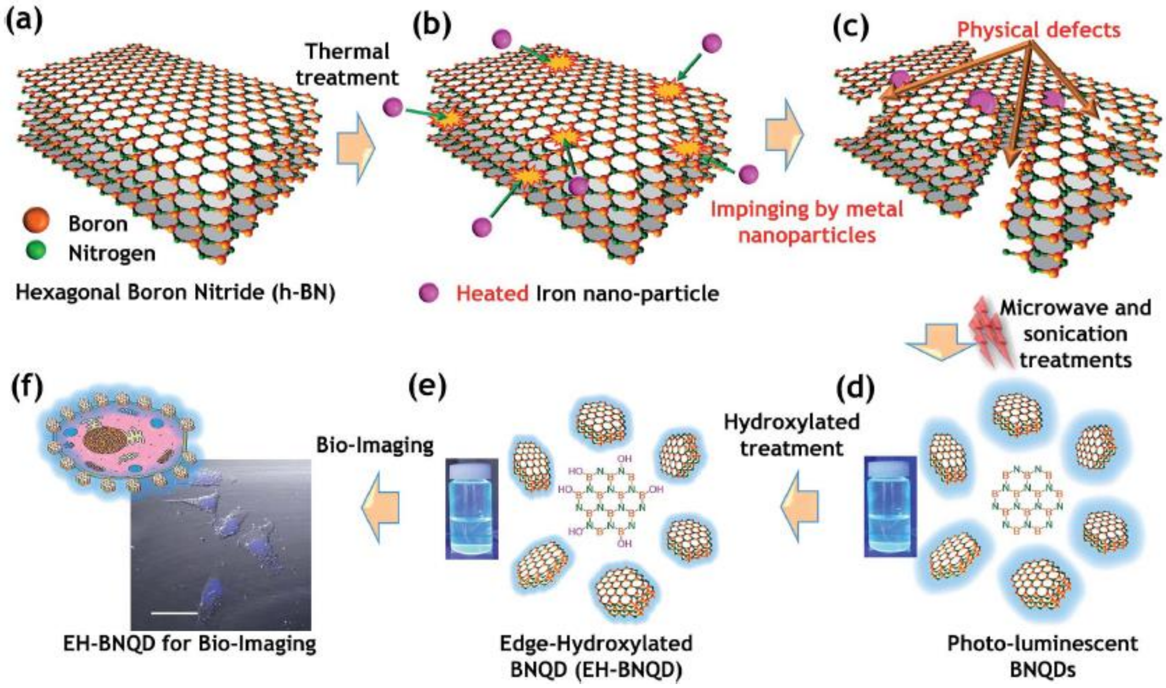

Figure 2.11 – Schematic of edge hydroxylated boron nitride quantum dot fabrication mechanism. Reproduced with permission from Jung, J. H. *et al.* Defect engineering route to boron nitride quantum dots and edge-hydroxylated functionalization for bio-imaging. *RSC Adv.* **6**, 73939–73946 (2016). Copyrights 2016 RSC[37].

The edge-hydroxylated BN QD (EH-BNQD) were tested in bio-imaging conditions. Results showed that that the edge-hydroxylation of the BNQDs facilitated their successful intracellular uptake for bio-imaging.

Fourier Transform Infrared (FTIR) and XPS spectroscopy were also performed to further clarify the chemical bonds formed after the fabrication of the BN QDs. FTIR analysis revealed a clear peak attributable to the hydroxyl (-OH) stretch in the edge hydroxylated solution, which was not present in the pristine BN and BN QDs, indicating the chemical modification of the particles. XPS was carried out at the B1s spectral range. The results indicated the strengthening of the oxidation peaks which again reaffirms the successful addition of the oxygen and hydroxyl functional groups to the BN QDs after the water vapor exposure.

A 2D map of the PL emission of the edge hydroxylated particles is shown in Figure 2.12 below. The excitation wavelengths applied ranged from 260 nm to 440 nm. The emission profiles mainly show two emission ranges when excited with up to 300 nm excitation. A PL emission at 320 nm and a wider peak at 450 nm. The peak at 320 nm is attributed to the boron and nitrogen vacancies in the BN basal plane. This peak has also been previously reported for defect rich bulk BN[87]. The PL emission peak at 450 nm however illustrated sensitivity to the acidity variation in the solvent, and hence was attributable to oxygen impurities.

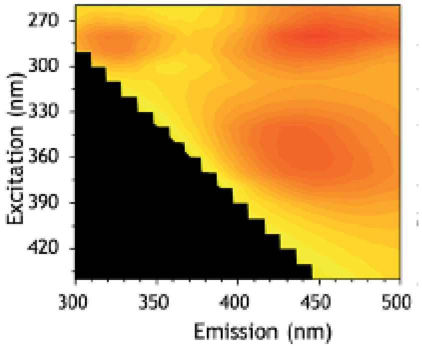

Figure 2.12 – Image of 2D map for PL spectra with various excitation wavelengths Reproduced with permission from Jung, J. H. *et al.* Defect engineering route to boron nitride quantum dots and edge-hydroxylated functionalization for bio-imaging. *RSC Adv.* **6**, 73939–73946 (2016). Copyrights 2016 RSC[37].

Tailoring the optical properties of graphene quantum dots by amino functionalization was accomplished by Tetsuka et al[88]. This allowed the electronic structure to be adjusted through the effective orbital resonance of amine moieties with the graphene core. The graphene quantum dots were fabricated by chemical oxidation before thermal exfoliation of natural graphite. The functionalized graphene quantum dots were prepared through chemical treatment of the fabricated graphene. Average quantum dot size was observed to be 2.5 nm, with the particles exhibiting a significant tunable luminescence. Figure 2.13 shows a schematic of the graphene functionalization process.

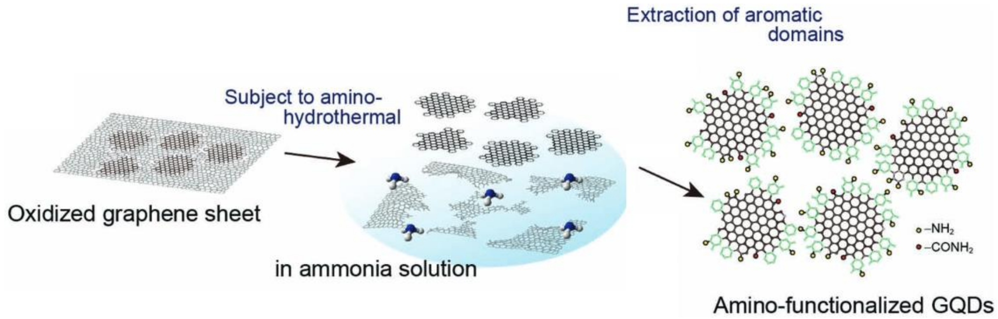

Figure 2.13 – Schematic illustration of the amino-functionalized graphene quantum dots. Reproduced with permission from Ramasubramaniam, A. Large excitonic effects in monolayers of molybdenum and tungsten dichalcogenides. *Phys. Rev. B.* **86**, 115409 (2012). Copyrights 2012 American Physical Society[88].

Zhang et al fabricated iodinated graphene oxide sheets (2-4 µm in lateral size) for photocatalytic applications[89]. A heated incubation process taking more than 24 hrs was used to functionalize the graphene sheets. It was found that the conductivity, carrier concentration, and mobility of the iodinated graphene oxide were increased by 5 orders of magnitude compared to graphene oxide. The significant improvement in the electrical properties of the iodinated graphene was attributed to the $I_3^-$ and $I_5^-$ implanted into the surface of the graphene oxide resulting in a larger Rashba spin-orbit coupling induced by heavy adatoms with active electrons occupying the p orbitals. This essentially provides tunneling of electrons between two carbon atoms and additional hopping channels. This results in an enhanced charge transfer process. The C-I bond was found to replace C-O bonds, that resulted in decreasing the surface energy. Figure 2.14 below, shows a schematic of the process, TEM images of the iodinated graphene oxide sheets, and contact angles for iodinated graphene.

Simek et al. also provided various methods including Hummers and Hoffmann methods for fabrication of iodinated graphene derivatives from a graphite oxide precursor. The yielded graphene oxide was iodinated by iodine or hydroiodic acid in an autoclave through elevated temperature and pressure for 24 hrs[90].

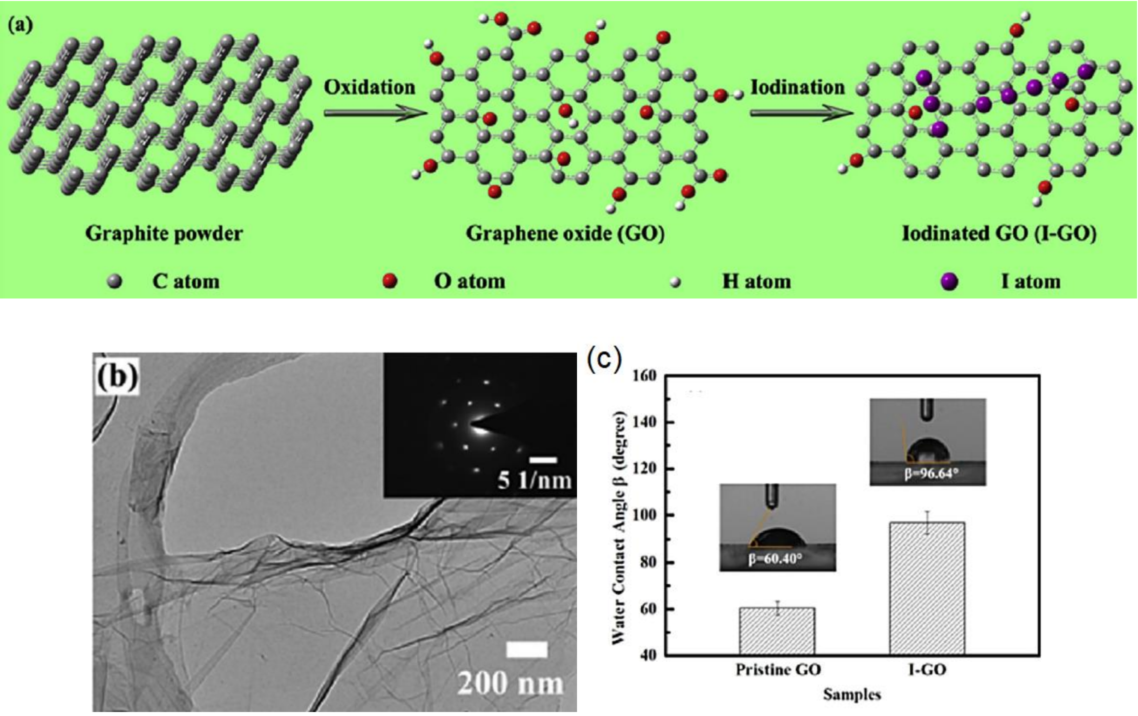

Figure 2.14 – (a) Schematic illustration of iodination process of graphene sheets and (b) TEM image of the iodinated graphene oxide sheets. Reproduced with permission from Zhang et al. The spin-orbit coupling induced spin flip and its role in the enhancement of the photocatalytic hydrogen evolution over iodinated graphene oxide. *Carbon N. Y.* **108**, 215–224 (2016). Coprights 2016 El Sevier[89].

Numerous papers discuss the functionalization of 2D monolayers or a few layer sheets. Chemical exfoliation was commonly used to fabricate these functionalized sheets as discussed before in previous works[45,91–93]. Paredes et al. for example, discuss their chemical exfoliation mechanism to obtain the $MoS_2$ sheets (50-500 nm lateral dimensions, mostly monolayer) in a nitrogen sealed environment for 2 days, followed by 1 hr sonication and dialyzing against water over 2 days. To functionalize the $MoS_2$ acetic acid, the sheets were kept in solution for 5 days and purified for 2 days. The $MoS_2$ crystal structure was converted from 1T to 2H by annealing the samples at 160°C for 4 hrs. Presoloski et al. report the functionalization of micron width $MoS_2$ flakes with thiobarbituric acid conjugates through a chemical exfoliation procedure (approximately 3 days long) with the intention of enhancing their electrochemical properties and making them more versatile in various applications. The covalent functionalization was shown to modify 50% of the surface coverage.

A key outcome in the literature for 2D sheet functionalization is making the sheets stable[45] in a variety of solvents and being colloidally stable[94] due to their common use in bio applications. Presoloski et al for example show that the covalent functionalization of the $MoS_2$ sheets enhances the solution dispersibility[45], but also improves their hydrogen evolution reaction activity, as well as DNA detection in solution. Jeong et al.[95] provide a study in which few-layered $MoS_2$ nanoflakes (a few hundred nm wide) edge functionalized with lipoic acid (LA) were confirmed to be stable in an aqueous dispersion for up to few months. Sim et al report the surface functionalization of $MoS_2$ with N-methyl-2-pyrrolidone (NMP) via a 6 hr chemical exfoliation procedure. In addition to high-yield restoration of the semiconducting 2H lattice structure, the functionalization provides an outstanding stability to the 2H- $MoS_2$ in water for more than 10 months. Figure 2.15 shows the sample stability with and without functionalization after the 10-month period.

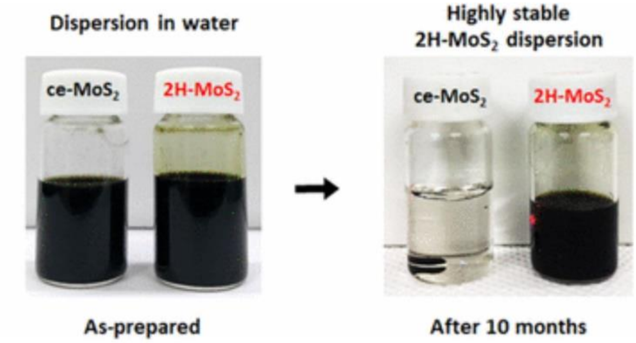

Figure 2.15 – Images illustrating the dispersion stability of 2H- $MoS_2$ (annealed in NMP) in water after 10 months. Reproduced with permission from Jeong et al. Preparation and characterization of a covalent edge-functionalized lipoic acid–$MoS_2$ conjugate. *RSC Adv.* **6**, 36248–36255 (2016). Copyrights 2016 RSC[95].

### 2.1.2 – Effect of functionalization on 2D nanoparticle properties

Doping and functionalization of 2D materials have shown to have several effects on their intrinsic properties. Satheeshkumar et al report the effect of covalent functionalization on the optical properties of exfoliated $MoS_2$ sheets functionalized with amino acids[48]. UV-visible spectroscopy shows characteristic $MoS_2$ peaks at 400, 447, 610 and 669 nm and absorptions due to amino acids below 300 nm

Also the effect of functionalization on solubility was assessed, for example BN QDs with oxygen functional groups[96], oleylamine-functionalized $MoS_2$-QDs[97], fluorinated Black Phosphorus (BP)-QDs[98], $TiL_4$-functionalized BP QDs[99], and SiC-QDs functionalized with octadecyl groups[100], carboxylic acid groups, and amines are all found to have enhanced solubility in a variety of solvents after functionalization. The ability to suspend 2D QDs in different solvents enables their use in a wider variety of applications especially bio applications where this aspect is crucial.

Shayeganfar et al.[101] used DFT simulations to investigate the effect of functionalization of BN QDs with hydroxyl $OH^-$, SH, and $NH_2$ and concluded that functionalization on both B and N zigzag edges adjusts the bandgap energy levels and semiconducting states, hence suggesting that the bandgap of the BP QDs can be manipulated by the nature of the chemical dopants attaching to it. DFT calculations have also been implemented on BP QDs, and revealed that an attachment of one or more benzene rings or anthracene can control the light absorption. This was attributed to red-shifting of the absorption caused by electron delocalization[102].

Tang et al found that trap states in BP QDs can be essentially eliminated by fluorine functionalization to obtain a coordination number of 3 or 5 for fluorinated and unfluorinated phosphorus atoms[98]. These air stable fluorine doped BP QDs illustrated enhanced defect-enhanced electronic tolerance, which is key for nanophotonics and nanoelectronics applications. DFT calculations similarly indicated that edge functionalization of $C_3N_4$ QDs with n-type materials can adjust the optical bandgap consequently enhancing the absorbance and charge transfer in nanocomposites for this material as well as graphene QDs.

Previous reports have established that functionalization can also be used to tune the PL emission of 2D QDs[103,104]. DFT simulations conducted by Shayeganfar et al. indicated that the side defect of BN QDs functionalized with hydroxyl OH, SH, and $NH_2$ attains single quantum emission in the visible range[101].

## 2.2 – Perovskite solar cell enhancement via 2D material additive engineering

2D materials have proven their versatility and suitability in a wide range of applications including electronic and optoelectronic applications such as electronic materials[105], composite materials[106], and sensors[107]. In all of these applications, 2D materials have show some improvement relative to the current state-of-the-art and their integration is still a work in progress.

Leveraging the exceptional properties of 2D materials discussed in length in Chapter 1, they have been integrated into perovskite solar cells (PSCs), both as individual layers and as additives, and have proven their ability to not only positively impact the power conversion efficiency (PCE) but also the stability of the solar cells. Their band gap tunability makes them compatible in terms of energy band alignment with other components in the solar cell, and their solution-processability makes a promising low-cost additive for PSCs. 2D materials can be engineered and synthesized in numerous ways, enabling control of their chemical composition, thickness, lateral size, optical properties, bandgap, absorbance, and thermal properties. Consequently, when integrated in PSCs they can have a significant influence on the performance.

### *TMDs in PSCs*

TMD materials have been implemented in several energy related applications[108–111] including solar cells, given their unique optical tunability, which is adjusted from indirect to direct bandgap as the TMD transitions from bulk/few layers to single layer. TMD electronic properties are also adjustable by controlling the metal and chalcogen compounds. Bernardi et al. have demonstrated that a TMD monolayer, which is thinner than 1 nm, is able to absorb as high as 5–10% of the incident sunlight. Strikingly, this corresponds to sunlight absorption that is one order of magnitude more than GaAs and Si[112].

### *Graphene in PSCs*

Being the most popular 2D material, given its appealing mechanical, electronic and thermal properties, graphene has received great attention for integration into perovskite solar cells. Knowing graphene's ultra-high carrier mobility of over 10000 $cm^2V^{-1}s^{-1}$, it can consequently embed nicely into either the electron or hole transport layer[113].

One of graphene's most commonly researched derivates; graphene oxide, has also been widely used in solution processed PSCs due to its dispersibility in water and other organic solvents, hence making film fabrication a faster and cheaper process[114–116].

### 2.2.1 – Integration of 2D materials into PSCs

2D materials have been reported as electrodes, charge transport layers (ETL and HTL), and also as interfacial layers between the perovskite and charge transport layers. The suitability of 2D materials as charge transport layers stems from their ability to separate and extract photo-generated carriers produced by the perovskite (absorber material), which is key to affecting the open circuit voltage (Voc), short circuit current (Jsc), and fill factor (FF). 2D materials have extensively been used as interfacial layers in PSC configurations. The undesirable electron-hole recombination that can occur during the charge transport process where electrons in the electron transport layer (ETL) recombine with holes in the perovskite layer, or holes in the HTL recombine with electrons in the perovskite, is detrimental to the PSC performance. Therefore, inhibiting the charge recombination via interfacial layers is a useful means to improve PSC performance[117].

### *2D materials in PSC electrodes*

A major cause of instability in PSCs is the usage of Ag or Au metal contacts which are highly likely to react with the halogen ions of the perovskite layer, consequently resulting in an efficiency drop. Therefore, using non-reactive carbon-based materials that are also heat and moisture resistant, like graphene and its derivatives, has the potential to improve PSC stability. This makes graphene and its derivatives exciting alternative charge collectors to replace the metallic contacts.

In as early as 2014, Han et al. reported carbon based electrode PSCs that illustrated 1000 hour stability in sunlight and ambient conditions[118], however PCE values for carbon based PSCs are still in the development stage ranging between 10-16%, which is significantly lower than that of noble metal electrode based PSCs[119]. This decrease in PCE can be attributed to significant energy losses relating to carrier transport and extraction of charge. Notable work has gone into minimizing the gap between the graphene-based and noble metal electrodes. You et al. have developed a PSC with a transparent graphene-based electrode strategy[120]. The device was built with a glass / FTO / $TiO_2$ / perovskite / spiro-OMeTAD / poly(3,4-ethylenedioxythiophene):poly(styrene sulfonate)(PEDOT:PSS) / graphene architecture.

The band structure of the device is shown below in Figure 2.17. The graphene contacts are deposited via chemical vapour deposition and by trial and error it was deemed that deposition of 2 layers of graphene results in the highest PCE compared to single, bi, tri, and multi layer graphene. The solar cells could be illuminated from either the FTO or graphene electrode side since the transparency of the graphene single and bilayer were more than 90%. The device with the bi-layered graphene electrode illustrated a PCE of 12.02% and 11.65% when illuminated from the FTO and the graphene electrode sides respectively. This was comparable to the PCE of 13.62% for a device with a Au electrode.

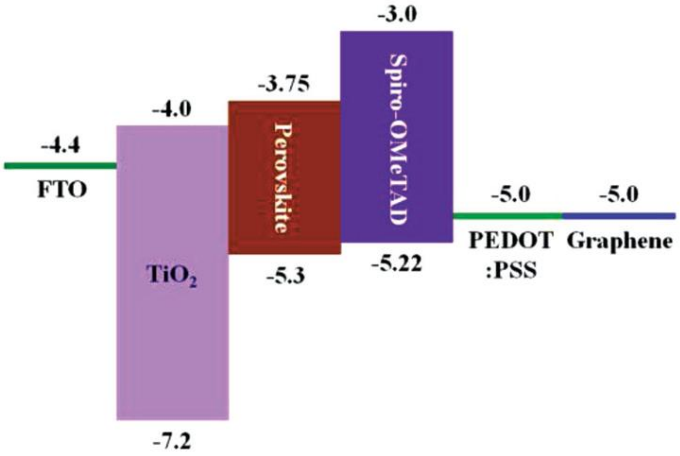

Figure 2.17 – Energy band diagram for graphene-based-electrode PSC. Reproduced with permission from You, P., Liu, Z., Tai, Q., Liu, S. & Yan, F. Efficient Semitransparent Perovskite Solar Cells with Graphene Electrodes. *Adv. Mater.* **27**, 3632–3638 (2015). Copyrights 2015 Wiley-VCH[120].

*2D Materials in PSC HTL*

It has been previously illustrated that the employment of 2D materials such as an ultra-thin layer of graphene oxide can contribute positively in not only being an efficient hole charge transport layer but also in being an electron blocking layer. That has been accomplished by doping or functionalizing the GO layer with additional materials such as fullerenes[121], organic molecules with long alkyl chains[122], and insulating polymers[123] onto conventional hole transport layers.

Reduced graphene oxide is a suitable candidate for a charge carrier transport layer as it is low cost, conductive, stable, and solution processable. Therefore Yeo et al. have employed reduced graphene oxide (rGO) reduced through chemical reduction at room temperature (p-hydrazinobenzenesulfonic acid hemihydrate) as a HTL in an inverted PSC architecture[124]. A large difference in energy levels between the absorbing layer and the charge transport layer can be detrimental for the PSC performance, and therefore rGO suits the energy diagram having a work function (WF) 0.4 eV higher than the perovskite (and a similar WF to a common HTL material PEDOT:PSS), as shown in Figure 2.18 (a)[124]. To assess the suitability of rGO as an HTL, photoluminescence (PL) tests were conducted on $CH_3NH_3PbI_3$ perovskite layers deposited on ITO/PEDOT:PSS, ITO/GO, and ITO/rGO substrates and the spectra are shown below in Figure 2.18(b). The PL quenching was found to be the lowest for the perovskite film grown on PEDOT:PSS, increased for the perovskite on GO, and was the most for the rGO based substrates. Given that the absorbance of the three films was found to be almost identical, the rGO based perovskite film exhibited the most quenching ability, indicating that the holes generated by the perovskite film are more efficiently extracted and transferred into the rGO HTL. Solar cells fabricated with the rGO had a lower series resistance and higher shunt resistance than the cells with PEDOT:PSS, indicating a better charge carrier mobility in the rGO and more efficient blocking of carrier recombination at the rGO-perovskite interface than at the PEDOT:PSS/perovskite interface.

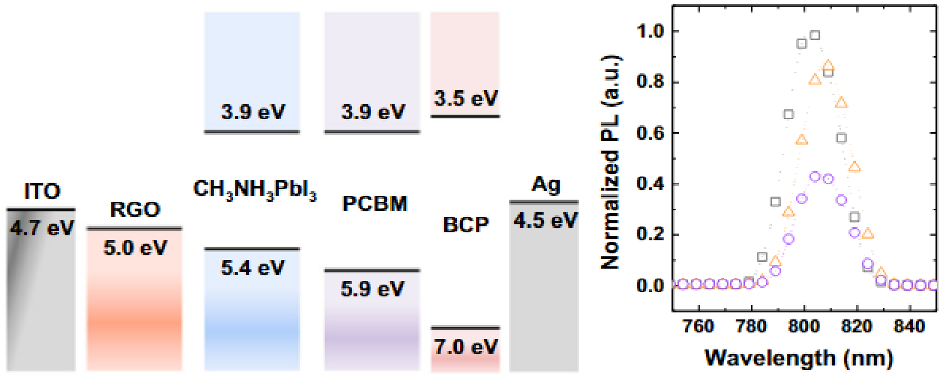

Figure 2.18 – (a) Corresponding energy level diagram of perovskite solar cell employing rGO as HTL. (b) PL spectra for photoluminescence responses of $CH_3NH_3PbI_3$ films on glass/ITO/PEDOT:PSS (black spectrum), glass/ITO/ GO (orange spectrum), and glass/ITO/RGO (purple spectrum). Reproduced with permission from Yeo, J. S. *et al.* Highly efficient and stable planar perovskite solar cells with reduced graphene oxide nanosheets as electrode interlayer. *Nano Energy* **12**, 96–104 (2015). Copyrights 2015 El Sevier[124].

The rGO based devices illustrated an enhancement of PCE by 20% relative to the PEDOT:PSS based device (from 9.1% to 10.8%), resulting from an improvement in the open circuit voltage (Voc) from 0.91V to 0.98V, short circuit current density from 14.1mA.cm$^{-2}$ to 15.4mA.cm$^{-2}$, and Fill Factor from 70.8% to 71.6%. It's worthy of mentioning that the graphene oxide based devices illustrated poor device performance compared to the devices with rGO and PEDOT:PSS. Reduced graphene oxide has properties more similar to graphene, such as high conductivity, whereas graphene oxide is rich in charge trap states and oxygen functional groups that decrease the charge carrier mobility and conductivity, consequently resulting in the observed decrease in PSC performance.

Other 2D materials such as $MoS_2$ and $WS_2$ have also been incorporated in the HTL, as summarized in Table 2.1, and resulted in an enhanced performance.

Table 2.1 – Performance of 2D materials studied through their incorporation in different layers in the PSC.

| **Function** | **2D material** | **Voc (V)** | **Jsc ($mA.cm^{-2}$)** | **FF (%)** | **PCE (%)** | **Ref.** |
|---|---|---|---|---|---|---|
| Electrode | graphene | 0.95 | 17.8 | 72 | 12.0 | 120 |
| Electrode | Multilayered rGO | 0.943 | 16.7 | 73 | 11.5 | 125 |
| ETL | graphene+ZnO | 0.93 | 20.0 | 56 | 10.3 | 126 |
| ETL | graphene+$TiO_2$ | 1.04 | 21.9 | 73 | 15.6 | 127 |
| ETL | GO (aqueous solution) | 1 | 17.46 | 71 | 12.4 | 128 |
| ETL | rGO+$TiO_2$ | 0.93 | 22.0 | 71 | 14.5 | 129 |
| ETL | rGO+$TiO_2$ | 0.84 | 16.5 | 67 | 9.3 | 130 |
| ETL | $MoO_3$ | 1.03 | 21.9 | 72 | 17.1 | 131 |
| HTL | rGO+spiro OMeTAD | 0.91 | 16.73 | 61 | 10.6 | 132 |
| HTL | rGO | 0.95 | 14.8 | 71 | 10.0 | 124 |
| HTL | $WS_2$ (1T phase rich) | 0.93 | 20.64 | 72.4 | 13.83 | 133 |
| HTL | $MoS_2$ (1T phase rich) | 0.87 | 20.35 | 77 | 13.62 | 133 |
| HTL | boron doped rGO | 0.88 | 16.74 | 60 | 8.96 | 134 |
| HTL | fluorinated GO+PEDOT:PSS | 1.04 | 18.5 | 77.1 | 14.9 | 135 |
| HTL | $MoS_2$ | 1.01 | 20.7 | 78 | 16.4 | 136 |
| Interfacial layer between Perovskite/HTL | $MoS_2$ | 0.93 | 21.5 | 67 | 13.3 | 137 |
| Interfacial layer between Perovskite/HTL | rGO | 1.11 | 21.5 | 79 | 18.7 | 138 |

*2D Materials in PSC ETL*

Due to their high conductivity and superior electron transport properties, the usage of zinc oxide films as the electron transport layer in PSCs is common. Zinc oxide has a relatively broad bandgap, with its electron mobility several orders of magnitude larger than that of commonly used $TiO_2$. However there has been numerous issues reported regarding engineering the interface of zinc oxide and graphene such as severe carrier recombination and harsh degradation as been reported before by Cao et al[116]. The increase of the PSC temperature to 90°C has proven to deprotonate the methylammonium cations by the zinc oxide, hence decomposing the perovskite film.

These deleterious issues and challenges have been reported in previous works prompting further research on enhancing the zinc oxide-perovskite interface. Cao et al. provided a thin layer of MgO that inhibits the charge recombination at the interface[116] and therefore enhances stability, and also promotes the electron extraction from the perovskite layer to the zinc oxide (inhibiting hysteresis effects).

More importantly, Chandrasekhar et al reported the incorporation of graphene nanoparticles into the zinc oxide ETL[126] as an additive creating a zinc oxide-Graphene nanocomposite (ZnO-G). The effect of varying the graphene concentration from 0 to 1 wt% and its effect on the PSC performance was investigated. Commercially available single layer graphene was added with different concentrations (0, 0.25, 0.75, 1) wt% into ZnO solution dissolved in ethanol solvent. The yielded solution was then sprayed on a pre-existing dense ZnO layer on FTO/glass substrate at elevated temperature to obtain a uniform film. Devices with glass/FTO/Dense ZnO/ZnO-G/perovskite/spiro OMeTAD/Ag architecture are shown below in Figure 2.19 (a), while the scanning electron microscope (SEM) images of the perovskite film grown on ZnO and 0.75 wt% ZnO-G are shown in Figure 2.19 (b).

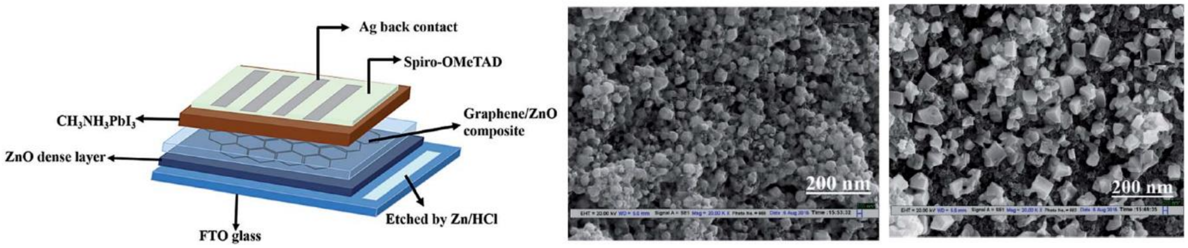

Figure 2.19 – (a) Schematic illustrating PSC device layers employing Zinc oxide-graphene nanocomposite as ETL. (b) SEM images of perovskite film grown on ZnO film (left), ZnO-G 0.75 wt% (right). Reproduced with permission from Chandrasekhar et al. Graphene/ZnO nanocomposite as an electron transport layer for perovskite solar cells; The effect of graphene concentration on photovoltaic performance. *RSC Adv.* **7**, 28610–28615 (2017). Copyrights 2017 RSC[126].

Leveraging graphene's large surface area, this resulted in the perovskite anchoring around the graphene flakes and consequently resulting in enhanced grain growth as observed in the SEM images in Figure 2.19 (b). This caused the cell with ZnO-G to have enhanced absorption, especially the 0.75 wt% ZnO-G nanocomposite. The increased absorption effectively boosted the photogenerated current and therefore the current density as observed in Figure 2.20 (a) where the 0.75 wt% ZnO-G recorded an increase of the PCE from 7.01% to 10.34% compared to the bare ZnO ETL. Another contributing factor to the enhanced performance can be attributed to the PL measurements shown in Figure 2.20 (b) where the perovskite film on ZnO showed a broad PL peak at approximately 780 nm, whereas with the addition of different graphene concentrations to the ZnO the PL is significantly quenched. This PL reduction can be attributed to efficient charge carrier extraction by the graphene network into the ZnO-G nanocomposite.

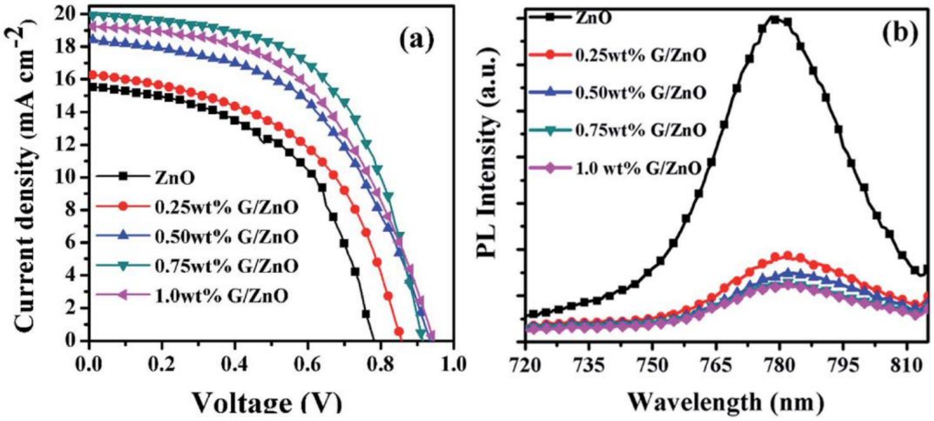

Figure 2.20 – (a) J-V curves and (b) PL spectra of perovskite film on a bare ZnO ETL and ETL with varied graphene concentrations Reproduced with permission from Chandrasekhar et al. Graphene/ZnO nanocomposite as an electron transport layer for perovskite solar cells; The effect of graphene concentration on photovoltaic performance. *RSC Adv.* **7**, 28610–28615 (2017). Copyrights 2017 RSC[126].

When the buffer layer between the dense ZnO and the perovskite was ZnO-G, this decreased the surface roughness and facilitated the growth of large perovskite grains, meaning that there were fewer grain boundaries. More grain boundaries mean that the electron transport is hindered significantly through grain boundary scattering and less conduction. The intimate interface between the graphene-ZnO nanocomposite and the perovskite, plays a crucial role in charge extraction, and efficiency enhancement. The nicely aligned energy bands between both the ZnO-G nanocomposite and graphene makes the electron transfer easier through decreased series resistance. Also, the larger grains in the perovskite that are facilitated by the graphene can also play a crucial role in scattering the incident light efficiently, increasing the photon recycling processes as reported previously by Friend et al[139].

It can be concluded that the 0.75 wt% Graphene-ZnO nanocomposite enhanced solar cell performance significantly by (i) inherently making the perovskite a better light absorber, (ii) the graphene being a great charge extraction and transport agent, and (iii) the graphene facilitating the growth of larger perovskite grains.

However, it was found that increased concentrations of graphene (i.e., 1 wt% in ZnO nanocomposite) resulted in a decreased PCE (dropping to 9.37%). This was attributed to parasitic absorption by the graphene itself.

Table 2.1 summarizes notable 2D materials and their usage in different locations in PSCs, along with their performances. Graphene, graphene oxide, and reduced graphene oxide have been employed most commonly in the ETL.

### 2.2.2 – Degradation routes of PSC

To understand the degradation routes, one must first analyze the ingredients and components of perovskite solar cells. Perovskites have a formula of $XYZ_3$, where X is typically formamidinium, methylammonium, or cesium, or a mixture of the three. Y is typically tin, lead, or a mixture of the two, whereas Z is a halogen, mostly iodine or bromine. Perovskites are considered salts, and therefore they have a strong affinity with water if not properly packaged. On the other hand, some weak bonds can be easily broken by light exposure. Light exposure can also create halogen vacancies and interstitial pairs that allow halogen migration and convert any present oxygen into highly reactive superoxide.

Temperature also plays a role in perovskite degradation, where the methylammonium lead iodide component of the perovskite film is susceptible to higher operating temperatures (e.g., 65-85°C) where slow degradation is observed. Higher rates of degradation are observed for temperatures that are commonly used when packaging the solar cells (e.g., 135-150°C)[140,141]. Perovskite films react with almost all metals and that is enhanced under illumination, as it promotes halogen mobility, and moderate temperatures, as heat makes the halides species more volatile[142–145].

However, of all of the factors that can affect the PSC, moisture and oxygen are the most pervasive. The primary route to stop their penetration is sealing and packaging. Flexible perovskite modules require flexible and impermeable sealing, which is generally high in cost, and the best packaging tends to fail after time with exposure to the conditions and outdoor elements. These reasons necessitate that the perovskite solar cells are intrinsically stable before inserting the packaging. Equation 2.1 and 2.2 show the moisture and thermal induced degradation respectively[146].

$$[(CH_3NH_3+)PbI_3]_n + H_2O \longleftrightarrow [(CH_3NH_3+)_{n-1}(PbI_3)_n][H_3O^+]+ CH_3NH_2 \quad (2.1)$$

$$MAPbI_3 \text{ (s)} \longleftrightarrow PbI_2 \text{ (s)}+Pb^0\text{(s)}+I_2\text{(g)}+CH_2NH_2\text{(g)}+CH_3I\text{(g)}+HI\text{(g)}+NH_3\text{(g)} \quad (2.2)$$

Therefore, numerous studies have worked on passivating the perovskite layer (and also passivating the grain boundaries due to their detrimental role in water adsorption). Wang et al. conducted a moisture degradation analysis on perovskites films with 678 nm and 297 nm average grain size[147]. It was found that they degraded by 15% and 95% after exposure to 85% humidity for 7 hours. Perovskite films with large grains have lower surface area to volume ratio and less defects, therefore they are less susceptible to moisture-induced degradation as it is the boundaries that are prone to degradation. It has also been reported that large grain size has a positive effect on PSC performance too, due to longer nonradiative lifetime and phonon re-scattering.

Due to the nature of the study in Chapter 4.0, which primarily focuses on enhancing the stability of the PSC against moisture and humidity using functionalized graphene, the upcoming sections in this literature survey will primarily focus on 2D materials usage for improving the stability and performance of PSCs.

#### 2.2.2.1 – Stability and PCE enhancement in PSCs via 2D material incorporation

In this section, the current state of the art with respect to the implementation of 2D materials in different layers in PSCs to enhance their ambient stability will be summarized. For instance, Yang et al. illustrated that incorporating 2D monolayers reduces trap states and enhances the metal oxide charge transport layers ability to transfer charge between interlayers and the perovskite[148].

In 2016, Lee et al incorporated graphene oxide into the conventionally used HTL material, such as PEDOT:PSS, for the first time, creating a GO-PEDOT:PSS composite as a novel HTL. The device architecture employed was glass/ITO/GO+PEDOT:PSS/perovskite/PCBM/Ag. Lee et al. compared using GO or PEDOT:PSS separately, and the GO+PEDOT:PSS composite as a HTL[121]. While GO has superior transparency and processability that make it a favorable charge transport candidate, when GO was used individually as a HTL, it was found to be problematic primarily due to the lack of film uniformity and thus an absence of full coverage and an intimate interface with the absorbing perovskite layer through the uncovered areas. These holes and gaps were problematic on many fronts. This resulted in poor hole extraction from the perovskite film and transport to the ITO, due to the direct contact between the active layer (perovskite) and the

ITO. Additionally, the lack of a full interface also causes non-homogeneous electrical properties due to the insulating properties of GO critically decreasing the reliability of the PSCs. Hence the addition of the PEDOT:PSS to the GO provided benefit from both GO and PEDOT:PSS properties. Due to the enhanced film coverage of the GO+PEDOT:PSS compared to the GO and PEDOT:PSS based devices, it was found that series resistance dropped to 2.5 ohm.cm$^2$ from 4.5 ohm.cm$^2$ and 3 ohm.cm$^2$ respectively. Also, the large bandgap of GO results in electron blocking, which prohibits unwanted recombination. A more well matched work function for the GO (assessed to be 4.9 eV) also makes the charge transport from PEDOT:PSS more efficient. All of the above factors contribute to enhancement of the PCE from 8.24% for the PEDOT:PSS HTL to 10.74% for the GO+PEDOT:PSS HTL. While just GO decreases to 6.42% due to the interfacial issues mentioned above. The stability of the device was also assessed at temperatures of 21–24°C and humidity of 38–55% for a 500 hrs testing span. The graph illustrating the PCE degradation is shown below in Figure 2.21. The GO HTL showed the best stability compared to the other two HTLs. The GO device maintained 70% of its initial PCE after the 500 hrs span while the GO+PEDOT:PSS and PEDOT:PSS fell to 20% and 0% respectively after the testing period was completed.

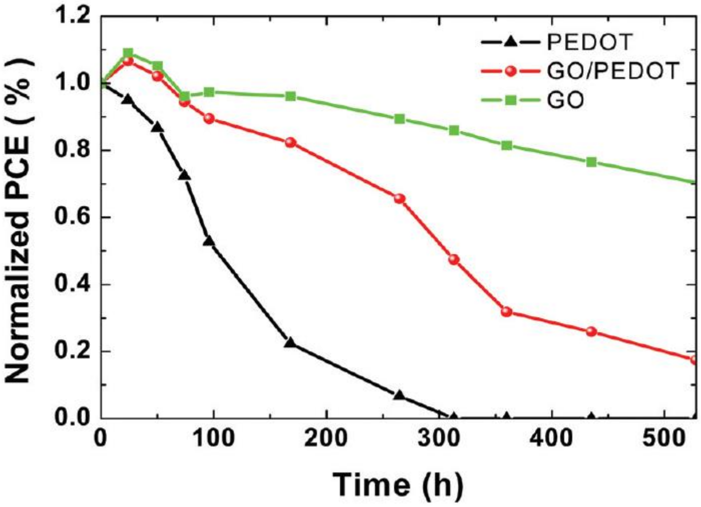

Figure 2.21 – Stability of PSC devices with PEDOT, GO+PEDOT:PSS, and PEDOT:PSS based HTL. Reproduced with permission from Lee et al. Graphene oxide/PEDOT:PSS composite hole transport layer for efficient and stable planar heterojunction perovskite solar cells. *Nanoscale* **8**, 1513–1522 (2016). Copyright 2016 RSC[121].

Agresti et al. leveraged graphene's properties including high carrier mobility of approximately 200000 cm$^2$V$^{-1}$s$^{-1}$, optical transmittance of more than 97.7%, and 1 TPA Young's modulus, which make it very useful as an interfacial material[149]. In this study, graphene was tested as an interfacial layer in several locations in the PSC as shown below in Figure 2.22. Monolayer and few layer graphene was obtained from exfoliation of graphite. The following devices were implemented, a control sample with glass/FTO/$TiO_2$/perovskite/spiro-OMeTAD/Au architecture, device B had a GO layer on top of the perovskite film, device C installed the graphene as a composite with the ETL $TiO_2$, whereas device D implemented the GO layer on top of the perovskite as well as a graphene nanocomposite with the ETL $TiO_2$.

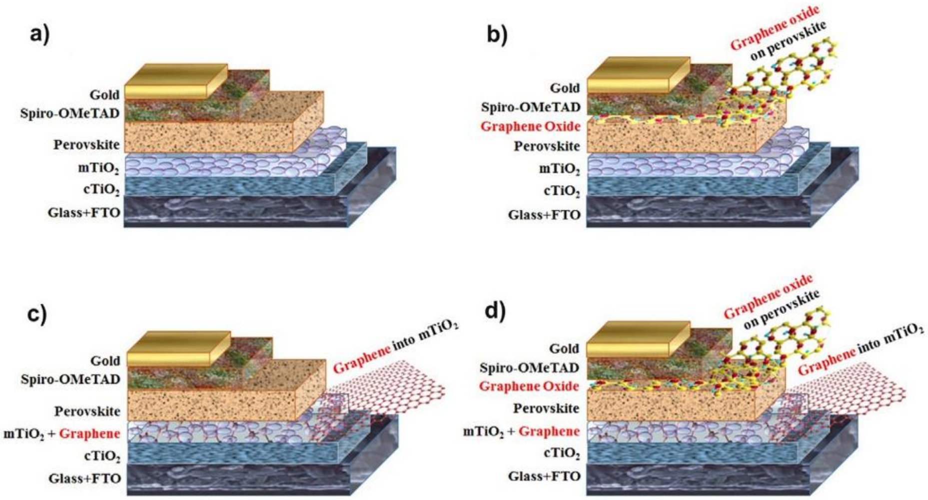

Figure 2.22 – PSC devices with different Graphene placements. (a) Reference device, (b) Device B with GO interlayer between perovskite and HTL, (c) Device C; Graphene nanocomposite in ETL $TiO_2$, (d) Device D with GO interlayer and Graphene+$TiO_2$ nanocomposite. Reproduced with permission from Agresti *et al.* Graphene–Perovskite Solar Cells Exceed 18 % Efficiency: A Stability Study. *ChemSusChem* **9**, 2609–2619 (2016). Copyrights 2016 Wiley-VCH[149].

The PCE results indicated average PCEs of 13.05%, 13.37%, 14.46%, and 15.42% for devices A, B, C, and D. The slight increase between device A and B was attributed to the increased hole injection that was assessed by the transient photovoltage measurements confirming faster Voc rise times indicating efficient regeneration of the active layer and charge transfer from the active layer to the HTL. Better incident photon-to-current conversion efficiency (IPCE) alongside the enhanced charge carrier dynamics induced by the graphene in the ETL $TiO_2$ enhanced the average PCE of devices C and D.

Several stability tests were implemented for the four devices including prolonged illumination tests, thermal stress tests, and shelf life aging tests. All are shown below in Figure 2.23. Stability illumination tests at 1 sun were conducted for a 16 hr span and are shown below in Figure 2.23 (a). Device C was found to maintain up to 88% of its initial PCE after the 16 hrs test was conducted. However, the GO based devices were interestingly found to have lower illumination stability than the control sample. It was clarified in this work that the deposition of the perovskite film here was done in ambient (air and humidity) conditions. Therefore the presence of $O_2$ and $H_2O$ in the absorbing layer triggers a hydration reaction with the perovskite crystals fueled by the illumination. This results in dissociation of the hydrogen bonding in the $CH_3NH_3$-I and the release of HI species that result in decomposition of both the perovskite and the GO layers. Shelf life testing over a 1000 hrs span and 35% average humidity shown in Figure 2.23 (b) did not indicate any significant differences in the stability behavior of any of the four devices. Devices tested against thermal stability revealed a good stability generally for all four devices (Figure 2.23 (c)). Device stability over the course of the 200 hr span revealed a retention of the PCE of more than 80% for the worst device. Interestingly, device A shows an increased PCE that is attributed to the heat induced crystallinity of the perovskite film.

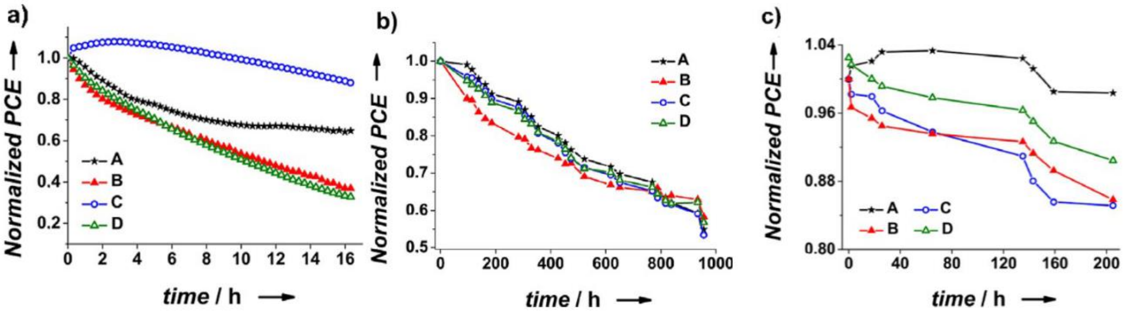

Figure 2.23 – Stability tests for various devices with PCE normalized to t:0 (a) illumination tests at 1 sun for 16 hrs, (b) shelf life stability, and (c) thermal stress tests. Reproduced with permission from Agresti *et al.* Graphene–Perovskite Solar Cells Exceed 18 % Efficiency: A Stability Study. *ChemSusChem* **9**, 2609–2619 (2016). Copyrights 2016 Wiley-VCH[149].

The useful material properties of TMDs also make them an attractive candidate as a buffer and interfacial layer. Capasso et al. employed few layer $MoS_2$ obtained through liquid exfoliation as an active buffer layer between the perovskite and the HTL[137]. The architecture implemented in this device was glass/FTO/$TiO_2$/perovskite/$MoS_2$/spiro-OMeTAD/Au. The implemented $MoS_2$ buffer layer was spin coated on top of the perovskite layer and can be seen below in Figure 2.24 (a). A planar layer of flakes was obtained through spin coating, although some uncovered areas were present on the perovskite. It was found to be a trade-off between having a uniform and continuous layer and having the thinnest buffer layer.

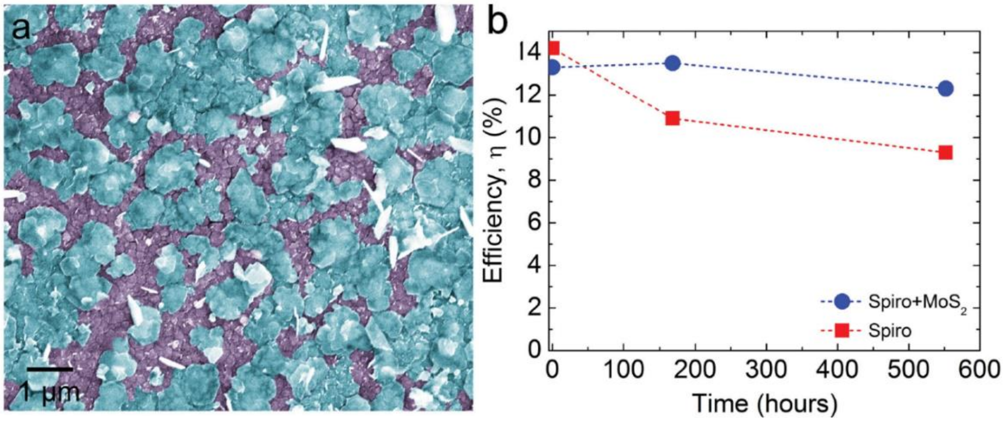

Figure 2.24 – (a) false color SEM image of the $MoS_2$ flakes deposited on top of the perovskite, (b) PCE trend over the 550 hr testing span. Reproduced with permission from Capasso, A. *et al.* Few-Layer $MoS_2$ Flakes as Active Buffer Layer for Stable Perovskite Solar Cells. *Adv. Energy Mater.* **6**, 1–12 (2016). Copyrights 2016 Wiley-VCH[137].

$MoS_2$ charge extraction ability and suitability as a HTL was assessed by constructing two devices, one with no HTL and another with the $MoS_2$ HTL. The PCE was boosted from 1.5% to 4.5% by adding the $MoS_2$ HTL. Capasso et al. concluded that the presence of $MoS_2$ as a buffer layer activates additional recombinational mechanisms compared and implemented the $MoS_2$ inside the spiro-OMeTAD HTL. The stability testing was conducted for both devices over a 550 hr testing span. It was found that the $MoS_2$+spiro-OMeTAD devices were more stable than the just spiro-OMeTAD counterparts, as a decrease of the PCE by 7% was observed compared to spiro-OMeTAD's 34% PCE decrease (Figure 2.24 (b)). This enhanced stability was attributed to the surface passivation role played by the $MoS_2$ buffer layer that stops iodine migration from the perovskite film to the HTL and also blocks the pathways created by the Au metal electrodes that decompose the perovskite film.

Thus, this study provides insight on usage of $MoS_2$ as an interfacial layer between the HTL and the perovskite to enhance its long-term stability, by creating a barrier for metal electrode migration and adding an additional energy matching layer that eases the hole transport from the perovskite to the HTL.

### 2.2.2.2 – Stability enhancement via hydrophobic materials and halogen-based additives

Yu et al, reported the introduction of double HTL stacking by adding fluorinated reduced graphene oxide (Fr-GO) to conventional HTL; PEDOT[150]. The addition of fluorinated graphene is promising due to its chemical stability, hydrophobicity, and high work function. The PEDOT and fluorinated graphene share the same solvent; 2-propanol, which facilitates sequential deposition of the fluorinated graphene on the PEDOT film. Fluorinated graphene oxide is spin coated 1, 3, or 5 times and the effect of the different number of layers is investigated versus the control sample (just PEDOT as the HTL). The average PCE was found to increase as a result of increasing the amount of spin coating layers, 10.3%, 12.5%, and 14.9% for the control sample (PEDOT device), 1 layer of fluorinated graphene oxide, and 3 layers of fluorinated graphene oxide respectively. It was however found that 5 layers reduces the PCE back to 13.0%. The device architecture employed for this study was (ITO)/ZnO/C60/$CH_3NH_3PbI_3$ ($MAPbI_3$)/HTL/$MoO_3$/Ag, as shown below in Figure 2.25 alongside the statistical PCE data for the fluorinated graphene oxide with different numbers of spin coated layers.

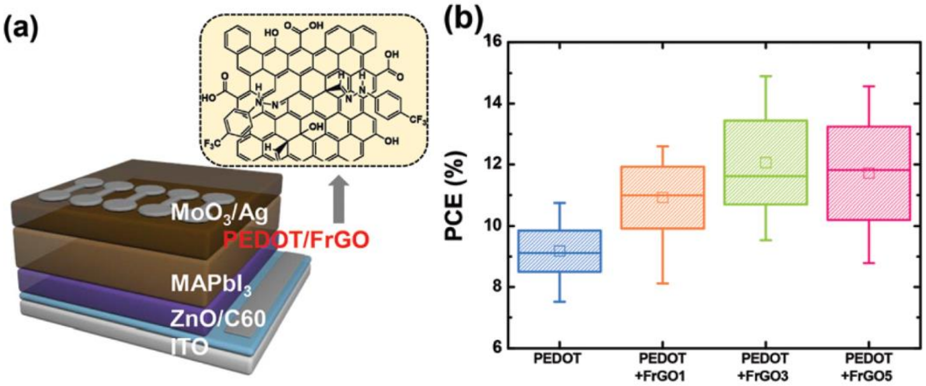

Figure 2.25 – (a) Device architecture adopting fluorinated graphene oxide as additive layer inside PEDOT:PSS HTL, (b) statistical data corresponding to several layers of spin coated Fr-graphene oxide. Reproduced with permission from Yu et al. Synergetic effects of solution-processable fluorinated graphene and PEDOT as a hole-transporting layer for highly efficient and stable normal-structure perovskite solar cells. *Nanoscale* **9**, 17167–17173 (2017). Copyrights 2015 RSC[150].

The improved PCE was attributed to numerous factors including external and internal quantum efficiency (EQE and IQE) improvements and increased surface roughness assessed by atomic force microscopy. But more importantly, shunt resistances were also found to improve with the presence of fluorinated graphene oxide, being boosted to 1119 ohm.cm$^2$ compared to 609 ohm.cm$^2$ for the cells with pristine PEDOT. Furthermore, contact angle measurements were taken for the three graphene-based films alongside the PEDOT film and the hydrophobicity was assessed. The contact angles shown below in Figure 2.26, show an increased contact angle of a water droplet from 95.2° to 96.1°, 104.1°, and 108.4°.

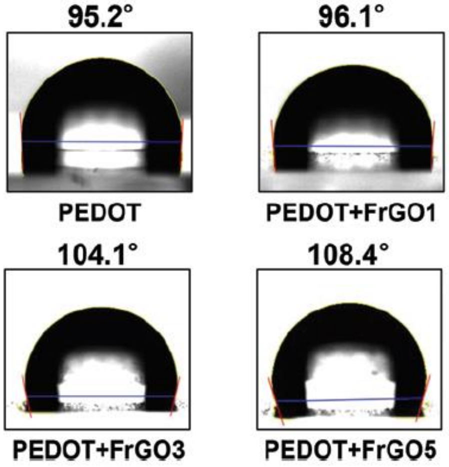

Figure 2.26 – Contact angles with a water droplet for PEDOT, and PEDOT/Fr-GO 1, 3, and 5 layers of spin coatingReproduced with permission from Yu et al. Synergetic effects of solution-processable fluorinated graphene and PEDOT as a hole-transporting layer for highly efficient and stable normal-structure perovskite solar cells. *Nanoscale* **9**, 17167–17173 (2017). Copyrights 2015 RSC[150].

A major reason for incorporating the Fr-GO in the PEDOT as an encapsulating layer alongside PCE improvement is enhancing the operational stability. A cell with Fr-GO (three layers of spin coating of Fr-GO) was exposed to ambient conditions for a 30-day span. Figure 2.27 shows the degradation of the PCE across the testing time span. It was found that the PEDOT based device was gradually degraded and illustrated very low PV parameters and PCE performance of only 36% of the initial PCE after the 30 day span was over. In contrast the Fr-GO embedded with the PEDOT showed better stability with the device maintaining 70% of its initial PCE after the 30-day testing period. This was attributed to the hydrophobic character confirmed by the contact angle measurements of the Fr-GO.

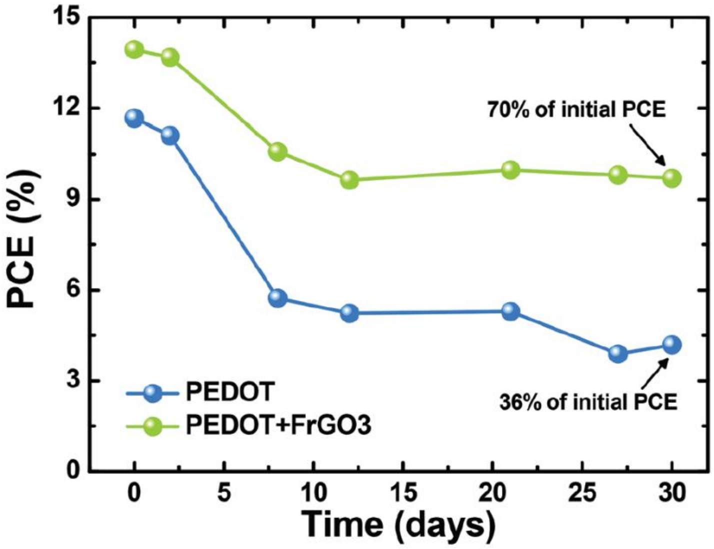

Figure 2.27 – PCE degradation after ambient exposure for 30 days for PEDOT-based and Fr-GO+PEDOT-based devicesReproduced with permission from Yu et al. Synergetic effects of solution-processable fluorinated graphene and PEDOT as a hole-transporting layer for highly efficient and stable normal-structure perovskite solar cells. *Nanoscale* **9**, 17167–17173 (2017). Copyrights 2015 RSC[150].

Graphene nanoplatelets edge-doped with fluorine and hydrogen (GNP-F/H) were developed by Kim et al to study the effect of halogens (fluorine in this study) on the stability of PSC[151]. The GNP were inserted as a thin layer capping the PSC as shown in Figure 2.28 (a). A ball milling experimental recipe was conducted in a reactant gaseous environment to dope and functionalize the edge of the graphene with the respective dopants (fluorine and hydrogen) as shown in Figure 2.28 (b). Hydrogen doping resulted in bonds such as (−OH, −C=O, −COOH) at the periphery of the graphene sheets. While the fluorine doping results in the super hydrophobic C-F bond that is known to resist chemical degradation that consequently repels water from moist air away and maintains the device stability.

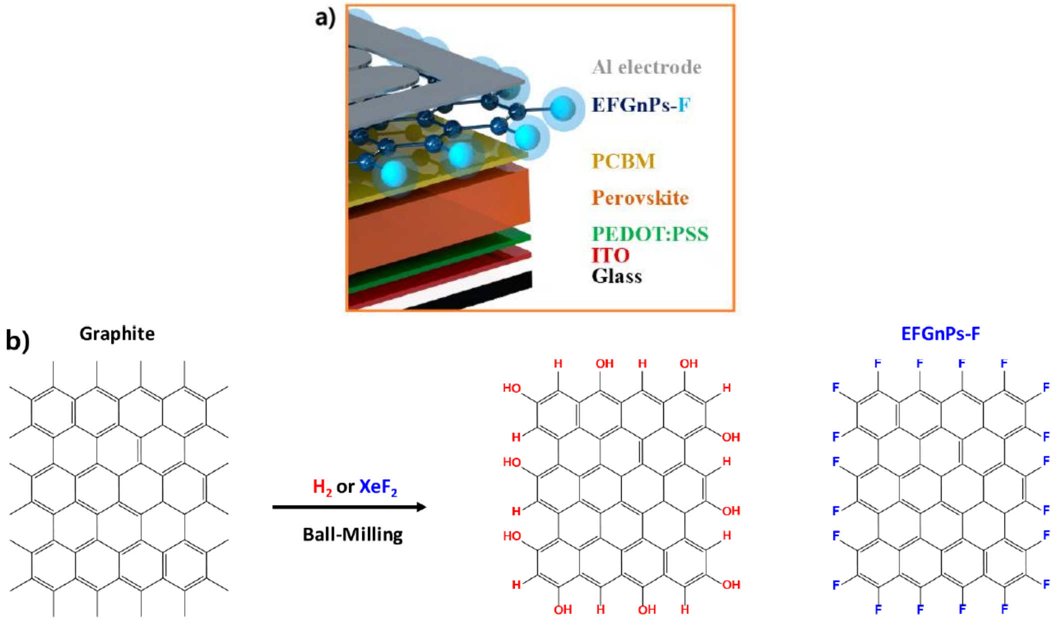

Figure 2.28 – (a) Device architecture inserting edge-functionalized fluorine graphene nanoplatelets in a glass/ITO/PEDOT:PSS/perovskite/PCBM/EGNP-F/Al architecture, (b) mechanical ball milling process resulting in edge functionalized hydrogen and fluorine doped graphene nanoplatelets. Reproduced with permission from Kim, G. H. *et al.* Fluorine Functionalized Graphene Nano Platelets for Highly Stable Inverted Perovskite Solar Cells. *Nano Lett.* **17**, 6385–6390 (2017). Copyrights 2017 American Chemical Society[151].

Many applications use the C-F bond’s hydrophobic properties such as polytetrafluoroethylene (Teflon). The EGNP-F comprised C-F bonding which imparts a repulsive property to water. Figure 2.29 shows the contact angle analysis of films of perovskite/ETL, perovskite/ETL/EGNP-F, and perovskite/ETL/EGNP-H.

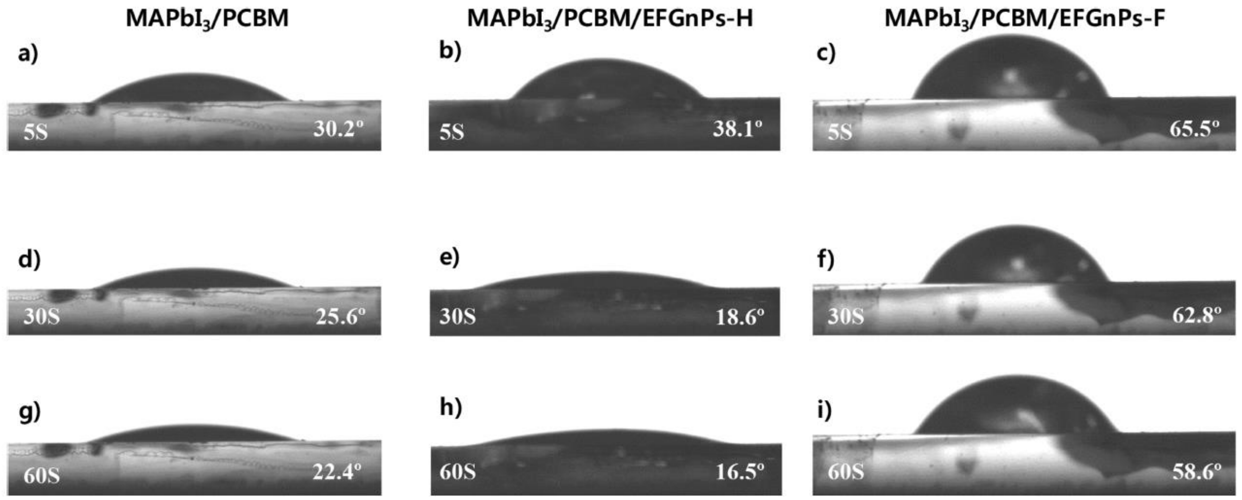

Figure 2.29 – Contact angle measurements after 5 s, 30 s, and 60 s for (a) (d) (g) perovskite/ETL, (b) (e) (h) perovskite/ETL/EGNP-H, and (c) (f) (i) perovskite/ETL/EGNP-F. Reproduced with permission from Kim, G. H. *et al.* Fluorine Functionalized Graphene Nano Platelets for Highly Stable Inverted Perovskite Solar Cells. *Nano Lett.* **17**, 6385–6390 (2017). Copyrights 2017 American Chemical Society[151].

As seen in Figure 2.29, at 5 seconds the device encapsulated with the EGNP-F has the highest contact angle at 65.5° compared to 38.1° and 30.2° for EGNP-H and perovskite/ETL devices respectively, which indicates the intrinsic hydrophobicity of the EGNP-F as the favored encapsulating material. The contact angles were assessed at 30 s and 60 s as well to examine the effect of water penetration into the film. The hydrophilic properties of the perovskite/ETL and EGNP-H based device showed a great decrease in the contact angle to 22.4° and 16.5° respectively after 60 s, while the EGNP-F based device showed a contact angle of 58.6°. These results indicate the fluorine-based particles repel water molecules and have greater stability in moist environments.

To test the full device stability, the three samples being compared were stored in ambient conditions for 30 days at approximately 50% relative humidity. The effect of moisture and air on the PCE of the PSCs is shown below in Figure 2.30. It was seen that the perovskite film with no EGNP encapsulation completely degraded (0.0 of initial PCE after 15 days) while the EGNP-F based device maintained 0.75 of its initial PCE after the testing period.

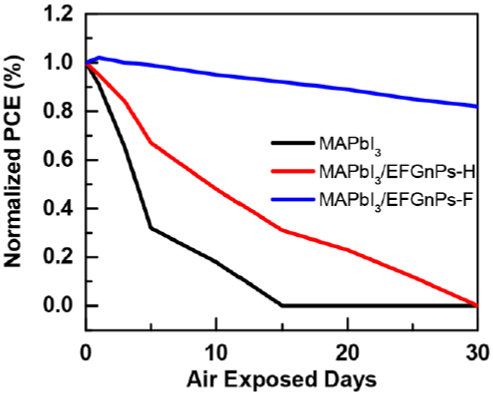

Figure 2.30 – Stability of PSC devices with EGNP-H and EGNP-F layers over 30 days. Reproduced with permission from Kim, G. H. *et al.* Fluorine Functionalized Graphene Nano Platelets for Highly Stable Inverted Perovskite Solar Cells. *Nano Lett.* **17**, 6385–6390 (2017). Copyrights 2017 American Chemical Society[151].

It has been previously reported by Luo et al that iodine can be used to enhance the conductivity of polymers and Carbon-based materials through the polyiodides that dope the carbon material or polymer[132]. They have shown to efficiently enhance charge transfer through the polyiodide chains and produce large amounts of mobile charge carriers that in turn increase the conductivity. Luo et al conducted a study to prove that common HTL materials like spiro-OMeTAD doped with lithium salt and pyridine are significantly less stable than spiro-OMeTAD that contains 2D materials (rGO doped with iodine in this case). Iodine doping was conducted with three different concentrations, to verify the best sample.

The device had an FTO/$TiO_2$/perovskite/HTL/Au architecture where the HTL is adjusted to different material combinations to assess the most efficient one. Dopant free spiro-OMeTAD was found to have lower conductivity and therefore low hole transport rate which affects the PCE. Graphene oxide's insulating nature also was detrimental for hole transport and hence PCE. Therefore, dopant free spiro-OMeTAD combined with reduced graphene oxide was used to investigate the effect on PCE. In this work they employed the conductive I-rGO in a way that hole pathways are increased and therefore the efficiency is boosted. The holes are extracted from the perovskite by the I-rGO and the dopant free spiro-OMeTAD and fed to the metallic electrode, and therefore these two synergetic routes of transporting and extracting charge from the perovskite boosted the PCE from 5.72% to 9.48% for I-rGO compared to the control sample with dopant free spiro-OMeTAD. Shown below in Figure 2.31 is the hole transport mechanism in the I-rGO+spiro-OMeTAD device.

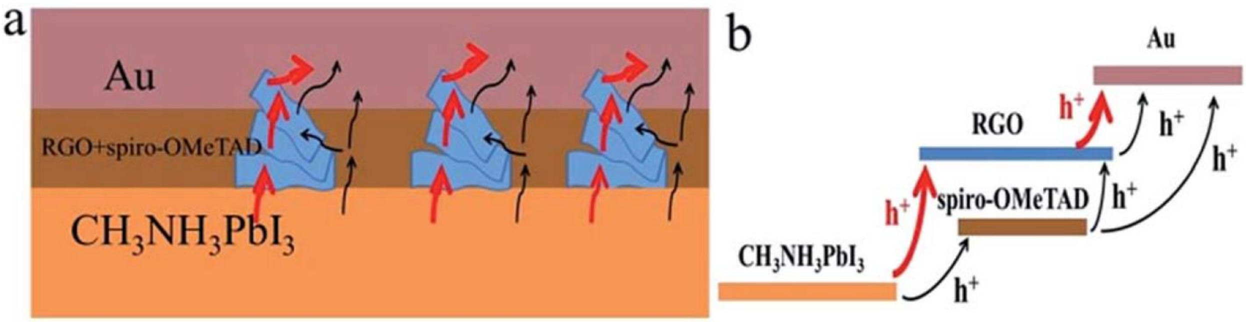

Figure 2.31 – (a) Schematic illustrating HTL-perovskite interface (b) energy levels illustrating various routes of hole transport. Reproduced with permission from Luo, Q. *et al.* Iodide-reduced graphene oxide with dopant-free spiro-OMeTAD for ambient stable and high-efficiency perovskite solar cells. *J. Mater. Chem. A* **3**, 15996–16004 (2015). Copyrights 2015 RSC[132].

Despite the doped (lithium salt + pyridine) spiro-OMeTAD illustrating a superior PCE valued at 12.56%, the long term stability was assessed in ambient atmosphere, in the dark, with an average temperature of 20± 3 °C and an average relative humidity of 40 ± 7%. The findings were surprising as the I-rGO + spiro HTL based device maintained 85% of its initial PCE while the (highly efficient) doped spiro-OMeTAD exhibited only 35% of its initial PCE after 500 h, as observed in Figure 2.32 below.

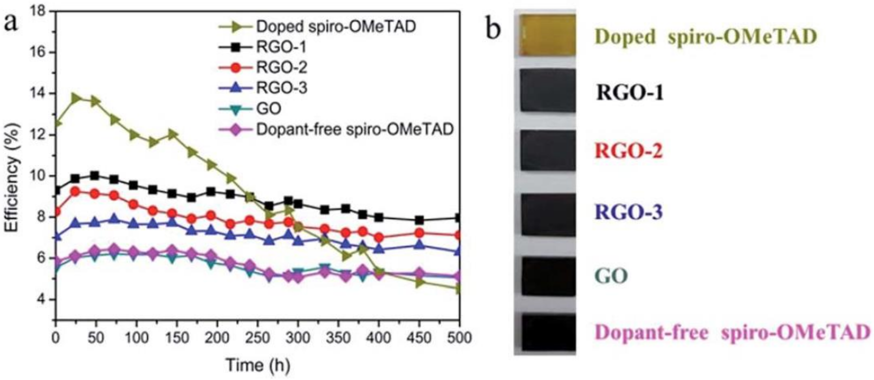

Figure 2.32 – (a) Stability of PCE across 500 hrs testing span for PSC based on different HTL, (b) Images taken after the 500 hrs testing is complete showing the degradation of the doped spiro-OMeTADReproduced with permission from Luo, Q. *et al.* Iodide-reduced graphene oxide with dopant-free spiro-OMeTAD for ambient stable and high-efficiency perovskite solar cells. *J. Mater. Chem. A* **3**, 15996–16004 (2015). Copyrights 2015 RSC[132].

DFT simulations have also been conducted to investigate the effect of using graphene and its derivatives as additives on the PSC stability, efficiency and performance. Jiao et al examined the electronic, optical, an long term stability properties of a graphene/$MAPbI_3$ nanocomposite interface[132]. The high binding energy of the interface indicate a high structural stability. Also, the simulations that calculated the imaginary part of the dielectric function proved an enhanced light absorption compared to the bare $MAPbI_3$. Additionally, the enhanced charge transfer at the graphene/$MAPbI_3$ interface resulted in inhibition of the electron-hole recombination. The stability was assessed when 36 molecules of water were simulated in the supercell with water density similar to that in room temperature and it was found that no water molecules were adsorbed to dissolve the Pb element of the perovskite film.

Liu et al also conducted DFT simulations to assess the effect of chlorine doping in lead Iodide perovskite films, where reduced electron hole recombination was proven as the photoluminescence lifetime measurements indicated a slower decay for $MAPbI_3$-Cl compared to the $MAPbI_3$ due to larger non adiabatic coupling and longer coherence time[132].

### 2.2.3 – Summary

Table 2.2 summarizes stability enhancement in PSCs via the incorporation of 2D materials in the current state of the art. Two main areas of improvement in the current state of the art are identified. First, the testing ranges were short and usually spanning 30 days. Additionally, for 50% of the provided studies, the efficiency was not retained.

Table 2.2 – Summary of notable work using 2D materials for PSC stability enhancement.

| 2D material | Fabrication | Location | Enhancement in stability | | | Change in PCE | | Ref. |
|---|---|---|---|---|---|---|---|---|
| | | | Stability testing conditions | Control sample | Material with 2D material | Control sample | Material with 2D material | |
| Fluorinated Graphene | Trifluoromethyl hydrazine reduction with graphene – 6 hrs | HTL | 30 days in ambient | 0.36 initial PCE | 0.7 initial PCE | 10.3% | 14.9% | [150] |
| GO | Commercially purchased | HTL. Composite additive with PEDOT:PSS | temperature of 21–24 °C and humidity of 38–55% - 500 hrs | 0.0 initial PCE (after 300 hrs) | 0.2 initial PCE (after 500 hrs) | 8.24% | 9.74% | [121] |
| GO and Graphene | Liquid phase exfoliation – 7 hrs | GO as interfacial layer between perovskite and HTL. Graphene as additive inside ETL. | 16 hrs under 1 sun illumination | 0.6 initial PCE | 0.3 initial PCE | 13.05% | 15.42% | [149] |
| $MoS_2$ | Liquid exfoliation – 8 hrs | Buffer layer between HTL and perovskite | 550 hrs in ambient condition | 0.63 initial PCE | 0.93 initial PCE | 14.2% | 13.3% | [137] |
| Edge fluorinated graphene | Ball milling – 5 days | Encapsulating layer over ETL in p-i-n device | 30 days in 50% relative humidity | 0.0 initial PCE (after 15 days) | 0.75 initial PCE | 14.7% | 14.3% | [151] |
| Iodine doped-reduced graphene oxide | Liquid dispersion – 4 hrs | Flakes covering the top HTL layer in normal PSC configuration | Ambient, dark, 20±3°C, relative humidity of 40 ± 7% | 0.35 initial PCE | 0.85 initial PCE | 12.56% | 9.48% | [132] |

## 2.3 – Nanorods from two dimensional materials

### 2.3.1 – Current state of the art fabrication mechanisms

Materials such as graphene and transition metal dichalcogenides (TMDs) exhibit excellent electrical properties due to their “flat” two-dimensional chemical structure. Sheets or flakes of these materials can allow for large area coverage with high conductivity but typically at the expense of transparency[55,56]. An approach to improving transparency, is by utilizing these materials in 1D nanorod-like structures. Carbon nanotubes (CNTs) are the most popular 1D variant of graphene and have been utilized to form large area conducting films. CNTs typically require lengthy purification and vacuum filtration procedures that take as long as 72 hrs as indicated in Table 2.3.[57,58] CNTs also tend to aggregate into bundles resulting in a larger sheet resistance than ITO films[53]. As an alternative to CNTs, the synthesis of carbon based nanorods has been reported by utilizing arc discharge[152] and microwave plasma chemical vapor deposition (CVD)[153] methods yielding rod lengths of 1-10 μm and diameters of 2-50 nm shown below in Figure 2.33. However, the arc discharge method requires an extensive filtering (Soxhlet extraction) and drying process, while the CVD method requires a high power and temperature (e.g., 850 °C). The growth of graphene nanoribbons has also been reported by ultra-high vacuum thermal evaporation[154] and hydrothermal techniques[155], yielding lengths of 20-450 nm and widths of 2-40 nm.

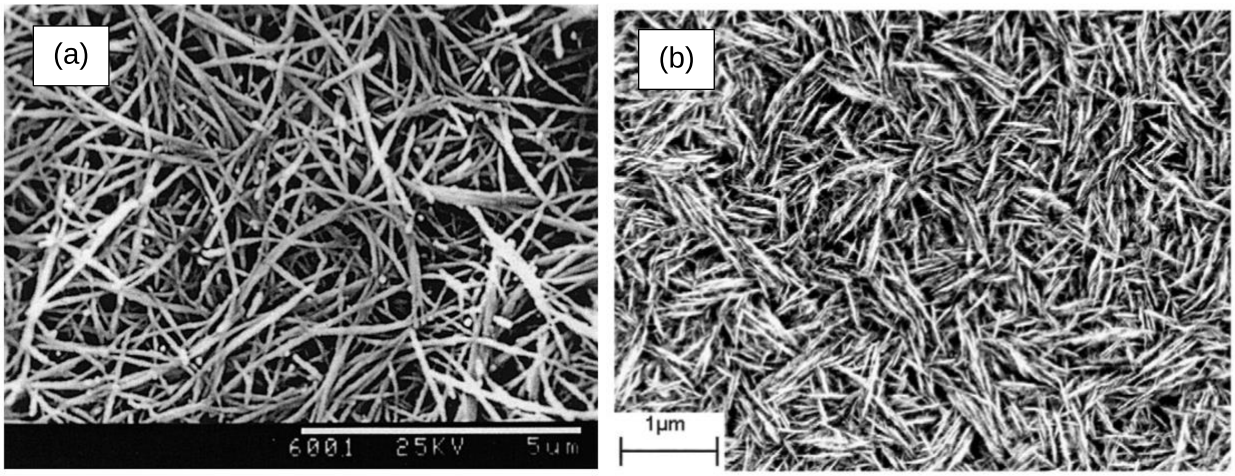

Figure 2.33 – SEM image of CNTs produced by (a) arc discharge method[152] and (b) microwave CVD. Reproduced with permission from Rakha et al. Diamond-graphite nanorods produced by microwave plasma chemical vapor deposition. *Diam. Relat. Mater.* **19**, 284–287 (2010). Copyrights 2010 El Sevier[153].

Regarding TMDs, molybdenum disulfide ($MoS_2$) nanorods with lengths of 50-150 nm and diameters of 20-40 nm have been previously synthesized utilizing a redox reaction in an aqueous solution. The process yielded a nanorod mixture of binary oxides ($Mo_xO_y$) and binary sulfides ($Mo_xS_y$) that were sensitive to the temperature, pH and amount of surfactant added to the solution[156]. Lin et al., reported a hydrothermal synthesis method that utilized the additive silicon-tungstic acid to form $MoS_2$ nanorods instead of nanoparticles[157]. The 24-hour reaction followed by washing, filtering and a 12-hour vacuum drying period yielded $MoS_2$ nanorods with lengths of 400-500 nm and diameters of 20-50 nm. SEM images of the $MoS_2$ particles with and without the silicon-tungstic acid additive are shown below in Figure 2.34.

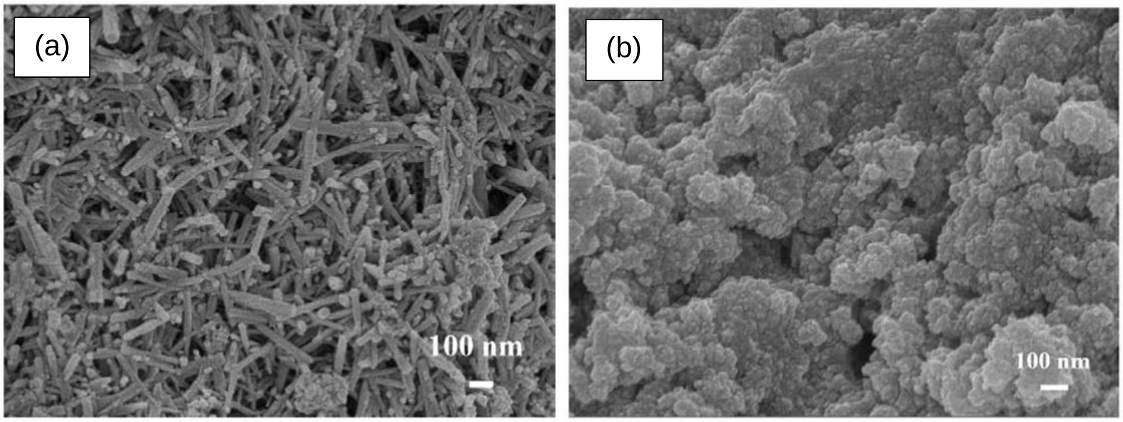

Figure 2.34 – SEM images of the $MoS_2$ particles (a) with and (b) without the silicon-tungstic acid additive. Reproduced with permission from Lin et al. Hydrothermal synthesis and characterization of $MoS_2$ nanorods. *Mater. Lett.* **64**, 1748–1750 (2010). Copyrights 2010 El Sevier[157].

Zhang et al. utilized a similarly lengthy hydrothermal method (20 hours) to produce $MoO_3$ nanorods that were converted to $MoS_2$ through an additional sulfurization step[158]. The $MoO_3$ rods were treated with a $H_2S$ gas mixture to yield $MoS_2$ rods with lengths of 4-5 μm and diameters of 200 nm. Similar to $MoS_2$, the synthesis of tungsten disulfide nanorods has been accomplished by hydrothermal[159,160] and sulfidation[161] methods. The hydrothermal methods required 24-hour reaction times and used additives such as cetylrtrimethylammonium and L-cysteine to yield nanorods with lengths of 0.1-2 μm and diameters of 20-400 nm. Zhang et al. used high energy ball milling of $WS_2$ powder for 122 hours, after which the powder was used as a precursor in a hydrothermal reaction for nanorod growth. The addition of the surfactant polyethylene glycol influenced growth in 1 direction to yield nanorod lengths of 2 μm and diameters of 10-15 nm[162]. SEM images before and after the ball milling of the $WS_2$ are shown below in Figure 2.35.

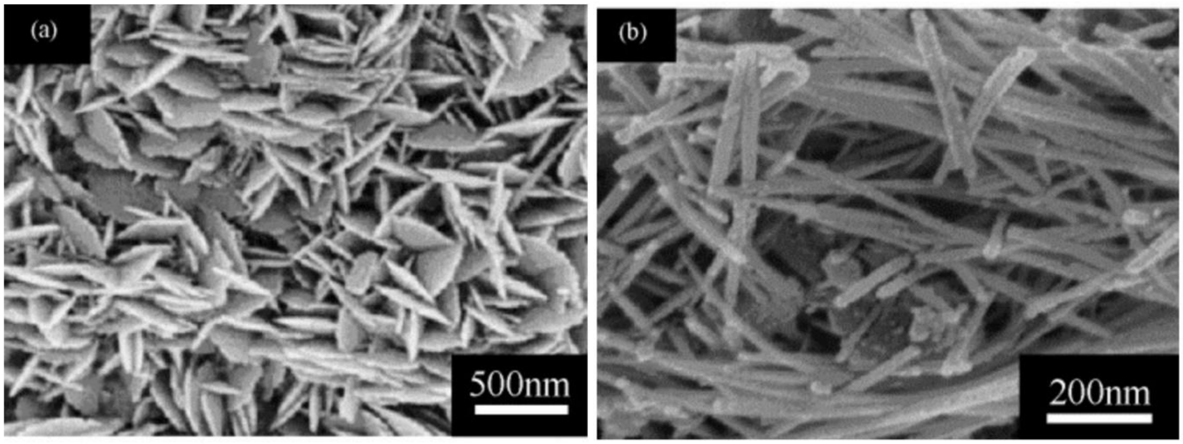

Figure 2.35 – SEM images of the $WS_2$ flakes (a) before and (b) after ball milling. Reproduced with permission from Zhang et al. $WS_2$ nanorods prepared by self-transformation process and their tribological properties as additive in base oil. *Mater. Sci. Eng. A* **454–455**, 487–491 (2007). Copyrights 2007 El Sevier[162].

Ball milling methods have also been used to produce boron nitride (BN) nanorods. Boron carbide powders were milled for 100 hours and subsequently treated with nitrogen at high temperature to produce BN nanorod lengths of 5 μm and 60 nm diameters[163–165]. Museur et al. reported the synthesis of BN nanorods through UV laser treatment of a compacted BN powder pellet. By varying the pulse width and laser fluence, they observed the recrystallization of BN particles to form rod structures embedded in amorphous boron suboxides ($B_xO_y$). A relatively high-pressure nitrogen environment was critical to the formation of rods with diameters of 15-30 nm and lengths of several microns, depending on laser treatment conditions[166].

Table 2.3 summarizes notable work on the fabrication of nanorods of 2D materials. Many of these methods require the use of high pressure or vacuum based environments, and are lengthy, multi-step procedures (often requiring more than a day to create the nanorods). Given the importance of nanorods in many disciplines, and the exciting properties of these materials with two-dimensional chemical structures, the development of simple and fast techniques to fabricate nanorods of two-dimensional materials is urgently needed. The ability to control the shape and composition of the nanorods through the processing would be particularly advantageous.

### 2.3.2 – Summary of 2D nanorod fabrication techniques

Table 2.3 – Summary of 2D nanorod fabrication techniques in the current state of the art compared to the findings discussed in Chapter 5.0.

| **Material** | **Geometry** | **Aspect ratio** | **Synthesis method** | **Synthesis conditions** | **Synthesis time** | **Ref** |
|---|---|---|---|---|---|---|
| **carbon nanorods** | W: 15-50 nm<br>L: 5-10 μm | 100-666 | arc discharge | He environment<br>50-70 kPa<br>650°C | ~24 hr | [152] |
| **graphene nanoribbons** | W: 2-3 nm<br>L: 20 nm | 6-10 | thermal evaporation + chromatography purification | Ultra high vacuum<br>440°C | ~72 hr | [154] |
| **graphene nanoribbons** | W: 20-40 nm<br>L: 200-450 nm | 5-22 | hydrothermal + annealed | Ar environment<br>1000°C | ~72 hr | [155] |
| **graphene nanorods** | **W: 800 nm**<br>**L: 8 μm** | **10** | **laser assembly** | **open atmosphere**<br>**0.25 W** | **<1 hr** | **this work** |
| **$MoS_2$ nanorods** | W: 20-40 nm<br>L: 50-150 nm | 1.25-25 | aqueous redox reaction | additive assisted | ~6 hr | [156] |
| **$MoS_2$ nanorods** | W: 20-50 nm<br>L: 400-500 nm | 8-25 | hydrothermal vacuum drying | 220°C<br>additive assisted | ~40 hr | [157] |
| **$MoS_2$ nanorods** | W: 200 nm<br>L: 4-5 μm | 20-25 | hydrothermal + sulfidation CVD | 400°C<br>$H_2S$ gas flow | ~72 hr | [158] |
| **$MoS_2$ nanorods** | **W: 1 μm**<br>**L: 6 μm** | **6** | **laser assembly** | **open atmosphere**<br>**0.25 W** | **<1 hr** | **this work** |
| **$WS_2$ nanorods** | W: 20-100 nm<br>L: 0.1-2 μm | 1-100 | hydrothermal method | additive assisted | ~36 hr | [159] |
| **$WS_2$ nanorods** | W: 420 nm<br>L: 2 μm | 5 | hydrothermal method | additive assisted | ~36 hr | [160] |
| **$WS_2$ nanorods** | W: 100 nm<br>L: 3-4 μm | 30-40 | plasma assisted sublimation + sulfurization | $H_2S$/Ar environment<br>86 Pa<br>550°C | ~3 hr | [161] |
| **$WS_2$ nanorods** | W: 10-15 nm<br>L: 0.1-2 μm | 7-200 | high energy ball milling | Ar environment<br>additive assisted | ~147 hr | [162] |
| **$WS_2$ nanorods** | **W: 700 nm**<br>**L: 3.5 μm** | **5** | **laser assembly** | **open atmosphere**<br>**0.25 W** | **<1 hr** | **this work** |
| **BN nanorods** | W: 40-75 nm<br>L: 5 μm | 66-125 | ball milling + annealing | $N_2$ environment<br>300 kPa<br>1300°C | ~110 hr | [163,164] |
| **BN nanorods** | W: 15-30 nm<br>L: 400 nm | 13-26 | laser assembly | $N_2$ environment<br>1000 kPa<br>0.5 W | ~12 hr | [166] |
| **BN nanorods** | **W: 300 nm**<br>**L: 1.5 μm** | **5** | **laser assembly** | **open atmosphere**<br>**0.25 W** | **<1 hr** | **this work** |

# 3.0 - Novel technique to simultaneously functionalize and fabricate two-dimensional nanoparticles

---

---

## 3.1 – Experiments and methodology

### *Solution Preparation*

Ultrafine powders of $MoS_2$, $WS_2$, and BN powders (bulk flakes had lateral dimensions of ≈1–3 μm) from Graphene Supermarket were dispersed in water/ethanol solvents to create 4 mL solutions. The powders were suspended in water/ethanol solvent (with ratio 1:1) at a concentration of 0.124 mg $mL^{-1}$. This concentration was used to avoid saturation of the UV–vis spectra, also to ensure sufficient laser interaction, and avoid aggregation of the flakes. Scanning Electron Microscope (SEM) images of the untreated bulk flakes are shown below in Figure 3.1.

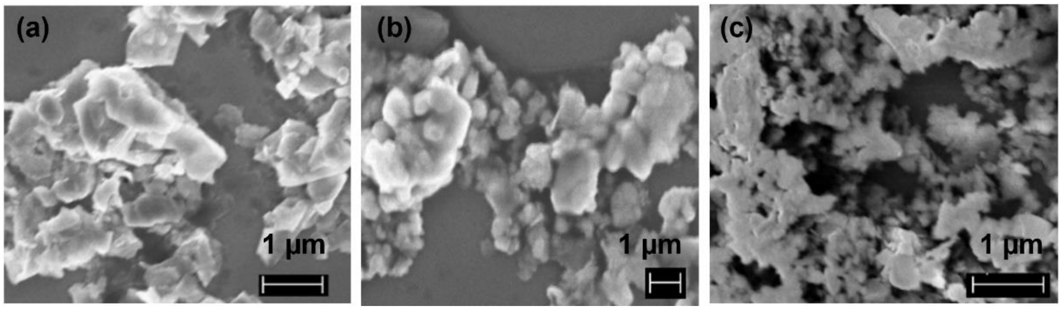

Figure 3.1 – Untreated bulk flakes of (a) $MoS_2$, (b) $WS_2$, and (c) BN. Reproduced with permission from Ibrahim *et al.* Simultaneous Fabrication and Functionalization of Nanoparticles of 2D Materials with Hybrid Optical Properties. **1701365**, 1–7 (2018). Copyrights 2018 Wiley-VCH.

### *Laser treatment*

A Spectra Physics Amplifier + Pump + Femtoliner Oscillator – ScientificPro 10 fs laser was operated with the following parameters: central wavelength of 800 nm, pulse width of 35 femtoseconds, repetition rate of 1 kHz. The beam focal point was set at a 0.5 cm depth below the air/solution interface with a focal length of 5 cm. The vial was placed on a magnetic stirrer stage and the solution was magnetically stirred at 200 rpm during treatment to ensure the homogeneity of the solution during treatment. The $MoS_2$ and BN solutions were treated for 70 mins, whereas the $WS_2$ was laser treated for 20 mins to obtain the nanoparticles. For purposes of analyzing the transition of the 2D materials from bulk flakes to nanoparticles, intermediate laser treatments were conducted (10, 20, and 35 mins for $MoS_2$ and BN whereas 1, 5, and 10 mins for $WS_2$). An image of the laser treated solutions is shown below in Figure 3.2. It is note worthy that the solution maintained its solubility, dispersibility, and stability after laser treatment up to few months. Contrary to the untreated solution

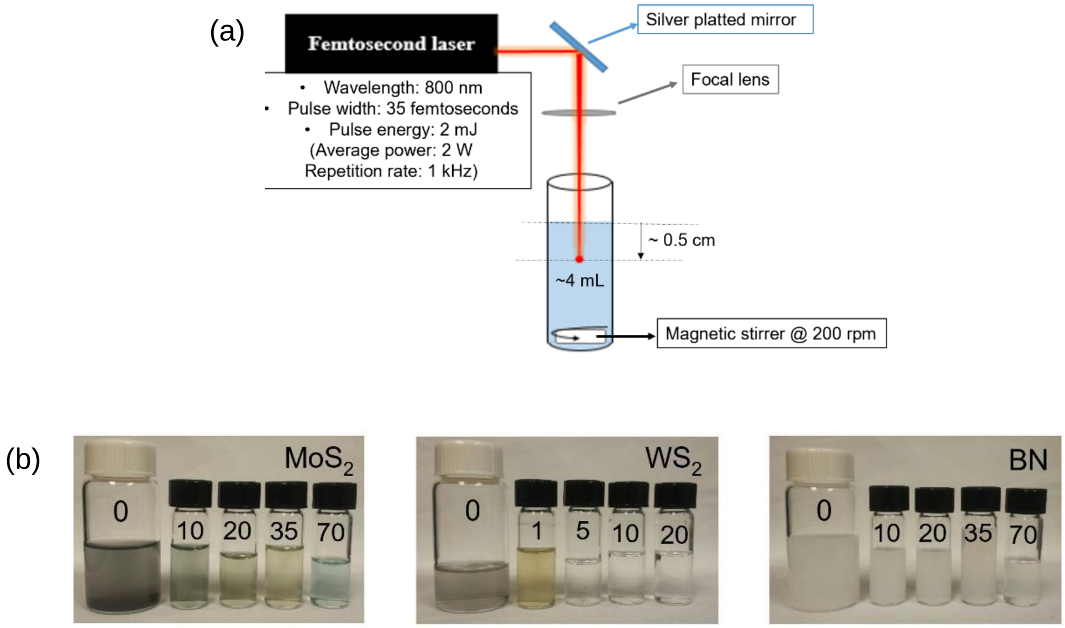

Figure 3.2 – (a) Schematic showing the femtosecond laser treatment setup. (b) Untreated and laser treated solutions of $MoS_2$, $WS_2$, and BN in a 1:1 water-ethanol mixture. Laser treatment times are indicated on the figures in minutes. Reproduced with permission from Ibrahim *et al.* Simultaneous Fabrication and Functionalization of Nanoparticles of 2D Materials with Hybrid Optical Properties. **1701365**, 1–7 (2018). Copyrights 2018 Wiley-VCH.

*Sample Characterization Preparation*

For characterization purposes, the solutions were centrifuged for 10 min at 10,000 rpm and the upper portion (1 mL) of the solution was drop casted on lacey carbon grids and silicon substrates for TEM and XPS/SEM/AFM/Raman, respectively.

The Raman spectroscopy was carried out for each sample using a Renishaw micro-Raman spectrometer with an excitation wavelength of 632.8 nm and power of 20 mW. The surface morphologies and microstructure of the drop-cast samples were studied using AFM (Dimension 3100 Scanning Probe Microscope), SEM (SEM-LEO 1530, using the Schottky-type field emission electron source), and Transmission Electron microscope (TEM) (Zeiss Libra 200MC). XPS samples were measured on silicon substrates and the Si 2p transition was used for binding energy calibration. Spectral analysis was performed by deconvoluting Gaussian multipeak fits. A double monochromator UV-2501 PC spectrophotometer (Shimadzu) with a 0.1 nm resolution was used to obtain UV–vis spectra. Photoluminescence spectra were collected using a PE LS55 PL employing 260 nm excitation.

## 3.2 - Understanding the functionalization phenomenon

The strong electric field at the laser focal point results in a phenomenon known as Coulomb explosion, breaking bonds within the 2D flakes and solvent molecules[167,168]. Scanning electron microscope (SEM) and atomic force microscope (AFM) images of BN and $MoS_2$ flakes treated at intermediate times (20 and 5 min, respectively) shown below in Figure 3.3, revealed large areas of voids, cleavage, and broken bulk flakes induced by the laser treatment.

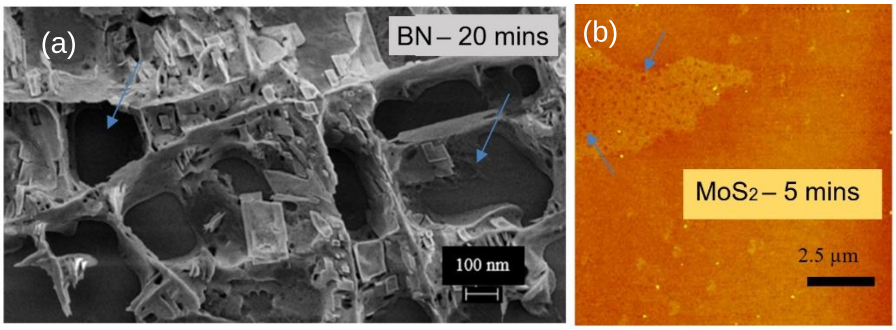

Figure 3.3 – (a) SEM and (b) AFM images of intermediate laser treatment times on BN and $MoS_2$ flakes laser treated for 20 and 5 mins respectively. The broken particles and cleavages induced by the laser treatment are pointed out with the blue arrow. Reproduced with permission from Ibrahim *et al.* Simultaneous Fabrication and Functionalization of Nanoparticles of 2D Materials with Hybrid Optical Properties. **1701365**, 1–7 (2018). Copyrights 2018 Wiley-VCH.

Continued laser treatment is expected to divide the 2D sheets into multiple 2D nanoparticles as shown in the upper portion of Figure 3.3 (a). Simultaneously, the laser focal point also inevitably laser treats the solvent ethanol and water molecules. Thus, dissociated species from the ethanol and water solvent molecules such as carbon and oxygen can bond with the freshly cleaved 2D nanoparticles, conveniently satisfying edge sites and decorating the periphery of the 2D nanoparticles, as illustrated in the lower portion of Figure 3.4. While basal plane functionalization is also possible, the mechanism proposed here is consistent with preferential edge functionalization[95].

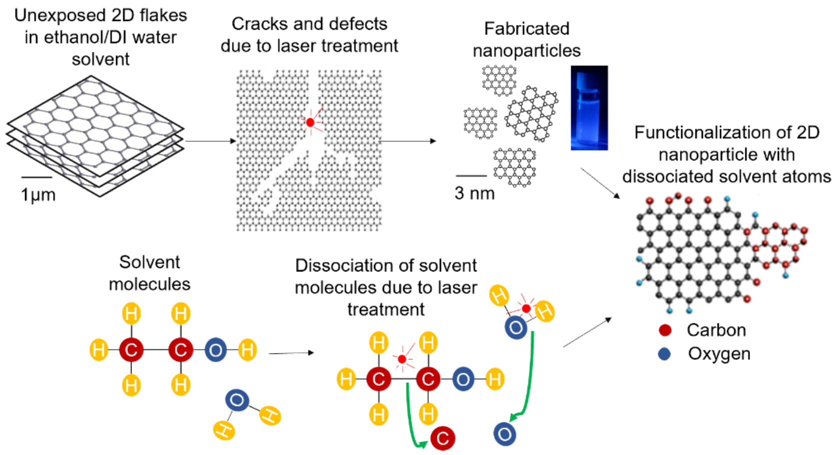

Figure 3.4 – Schematic illustrating the laser treatment simultaneously reducing the size of the flakes and dissociating the solvent molecules, in turn functionalizing the 2D nanoparticles. Reproduced with permission from Ibrahim *et al.* Simultaneous Fabrication and Functionalization of Nanoparticles of 2D Materials with Hybrid Optical Properties. **1701365**, 1–7 (2018). Copyrights 2018 Wiley-VCH.

## 3.3 – Characterization

After laser treatment is conducted for the respective times, the solutions were centrifuged for 10 min, and the upper portion of the solution was extracted (to avoid aggregates and artifacts) and drop cast onto a supporting substrate for characterization. In the upcoming sections we investigate how the laser treatment affects the yielded nanoparticles from a chemical, structural, morphological, and optical standpoint. By analyzing X-ray photoelectron spectroscopy (XPS), the nature of the chemical species attached to the 2D nanoparticles is discussed. TEM images identify the location of these attached species and identify the particle size. Raman analysis sheds light on the structure of the particles, and UV-Visible absorption measurements illustrate the tunability of the optical properties possible with the laser treatment process. The nanoparticles functionalized via laser treatment are denoted throughout using the prefix “f-“ (i.e., f-$MoS_2$, f-$WS_2$, and f-BN).

### 3.3.1 – Structural and chemical properties

#### *Microscopy analysis*

TEM analysis was conducted on the laser treated samples to specify the location of the functionalization and to quantify the size of the yielded particles. Figure 3.5 show (a) $MoS_2$, (b) $WS_2$, and (c) BN samples after 70 mins, 20 mins, and 70 mins of fs laser treatment, respectively. Nanoparticle size histograms are shown in the insets of Figure 3.5 (a)(c) and indicate a reduction in the lateral size of the nanoparticles to ≈3.5, 3.3, and 3.9 nm for $MoS_2$, $WS_2$, and BN, respectively. The centrifugation results in reasonably narrow size distributions (±1.5 nm). The shorter treatment time required to produce 3 nm nanoparticles of $WS_2$ (20 min cf. 70 min for $MoS_2$ and BN) may be attributed, in part, to the lower binding energy associated with $WS_2$. As Coulomb explosion is simply due to the repulsion of atomic ions after electrons are rapidly removed, the degree to which it occurs depends heavily on the degree to which electrons are removed. In $MoS_2$-$WS_2$ heterostructures,[42,169] $WS_2$ is typically reported as the electron donor that more readily gives up outer electrons than $MoS_2$, and BN is characterized by stronger bonding and a higher melting temperature than $MoS_2$ and $WS_2$. Therefore, electron removal and Coulomb explosion is expected to occur more readily in $WS_2$. Figure 3.5 (d) shows a TEM image of a single functionalized f-$MoS_2$ nanoparticle (treatment for 70 min). The central portion of the nanoparticle has a lattice spacing of 0.27 nm (indicated by the black line), consistent with the (100) planes of $MoS_2$. However, the edges of the particle show a wider lattice spacing of 0.35 nm (indicated by the red lines), suggesting that foreign elements bonded to the periphery of the nanoparticle. Previous studies discussing fabrication of graphene quantum dots have revealed a similar lattice spacing[170].

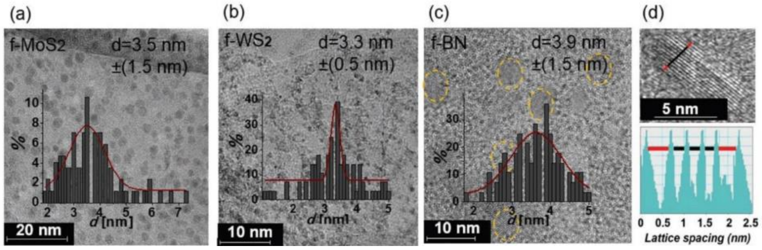

Figure 3.5 – TEM images of fabricated nanoparticles. a) f-$MoS_2$ laser treated for 70 min, b) f-$WS_2$ laser treated for 20 min, and c) f-BN laser treated for 70 min (individual nanoparticles highlighted with dashed yellow lines). Insets show nanoparticle size distribution histograms. d) f-$MoS_2$ nanoparticle laser treated for 70 min. The lattice profile indicates a wider lattice spacing on either side of the particle, suggesting the attachment of foreign elements. Reproduced with permission from Ibrahim *et al.* Simultaneous Fabrication and Functionalization of Nanoparticles of 2D Materials with Hybrid Optical Properties. **1701365**, 1–7 (2018). Copyrights 2018 Wiley-VCH.

Prolonged laser treatment (e.g., 110 min) was conducted and it was found that the particle size saturates at ≈3 nm, as measured by AFM. AFM images of the nanoparticles are shown below in Figure 3.6 and they show average particle thicknesses of 1.1, 1.2, and 1.7 nm for f-$MoS_2$, f-$WS_2$, and f-BN. This is indicative of predominantly bilayer nanoparticles accompanied by some monolayer and few-layer nanoparticles.

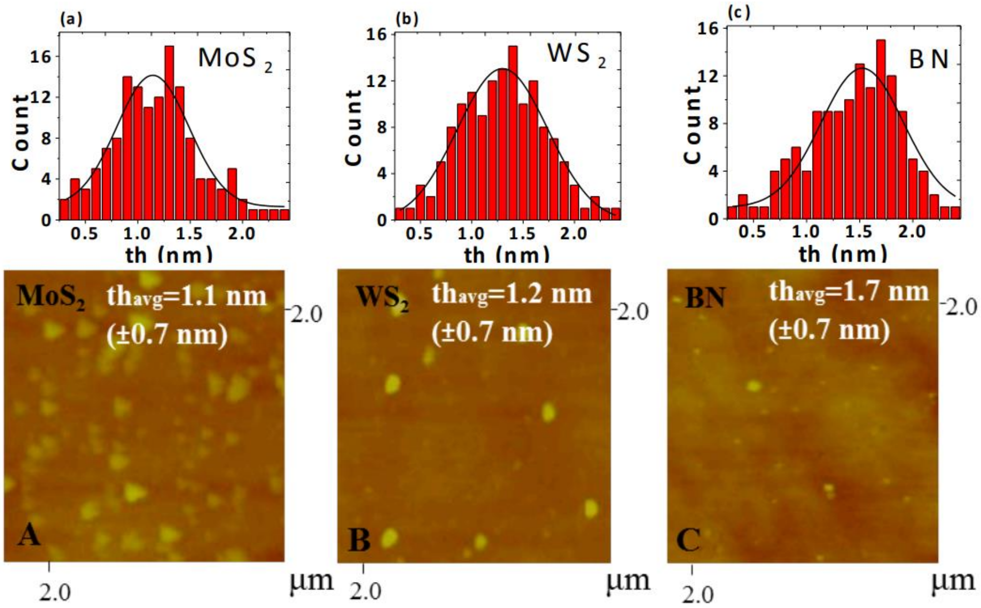

Figure 3.6 – AFM images and particle thickness histograms illustrating the average thickness of the (a) $MoS_2$ (1.1 nm), (b) $WS_2$ (1.2 nm), and (c) BN (1.7 nm) functionalized nanoparticles. Reproduced with permission from Ibrahim *et al.* Simultaneous Fabrication and Functionalization of Nanoparticles of 2D Materials with Hybrid Optical Properties. **1701365**, 1–7 (2018). Copyrights 2018 Wiley-VCH.

*Chemical composition*

To identify the effect of laser treatment on the nature of the newly bonded atoms to the host 2D materials, X-ray photoelectron spectroscopy (XPS) was performed. The upper panel of Figure 3.7 (a) shows the XPS spectrum of untreated $MoS_2$ flakes, where peaks at ≈229 and 233 eV correspond to Mo $3d_{5/2}$ and Mo $3d_{3/2}$ of 2H semiconducting lattice structure of $MoS_2$[97], and a characteristic S 2s peak is observed at 227.0 eV.

The XPS spectrum of $MoS_2$ treated for 70 min (f- $MoS_2$) is shown in the lower panel of Figure 3.7 (a). The appearance of closely spaced peaks makes assignment challenging; however, the attachment of carbon and oxygen to the molybdenum is clearly observed. Peaks at 229.7, 231.0, 231.4, 232.4, 234.2, 234.7, and 235.5 eV, are attributable to $MoO_x$, $MoO_2$, $Mo_2C$, $MoO_3$, $MoO_2$, $MoO_x$, and $MoO_3$, respectively[171,172]. In the S 2p spectrum of f-$MoS_2$ in Figure 3.7 (b), peaks corresponding to C-$SO_x$ species are observed, in addition to the intrinsic S 2p peaks[173–175].

The contributions of the various peaks are summarized in Table 3.1 and indicates that significant functionalization occurs. The weights of the Mo $3d_{5/2}$ and Mo $3d_{3/2}$ peaks are reduced to 17.8% and 15.8% respectively for the f-$MoS_2$, whereas the carbon-related $Mo_2C$ accounts for 30.9% of the signal.

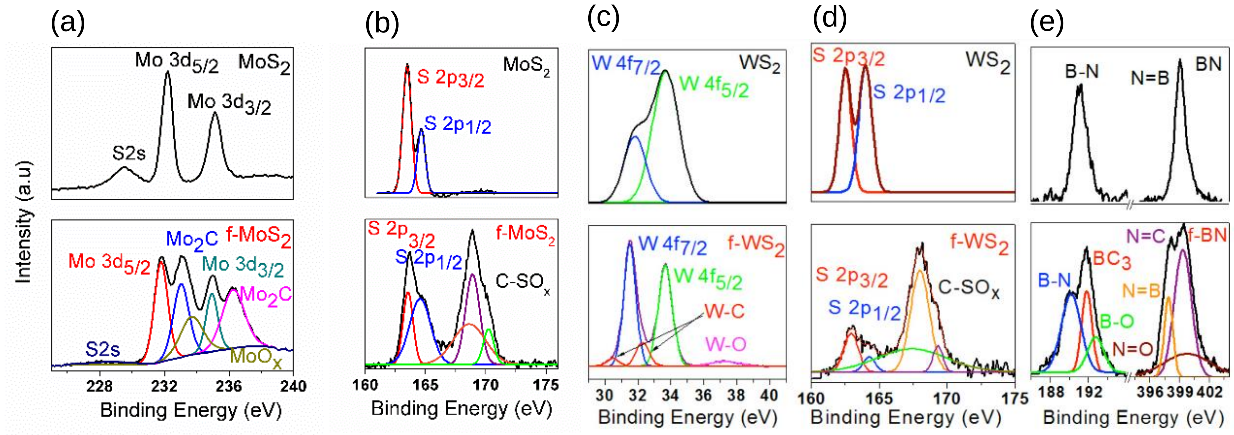

Figure 3.7 – Composition of fabricated nanoparticles. (a) Mo 3d (b) S 2p XPS spectra of $MoS_2$ flakes (c) W 4f (d) S 2p XPS spectra of $WS_2$ flakes (e) B1s and N1s XPS spectra of BN flakes. (All of the upper panel spectra for untreated bulk flakes while lower panel indicates spectra for laser treated particles). The Gaussian multipeak fitting shows the respective chemical bonds, including the incorporation of carbon and oxygen. Reproduced with permission from Ibrahim *et al.* Simultaneous Fabrication and Functionalization of Nanoparticles of 2D Materials with Hybrid Optical Properties. **1701365**, 1–7 (2018). Copyrights 2018 Wiley-VCH.

Significant incorporation of carbon as well as some oxygen is similarly seen in Figure 3.7(d)(e) and Table 3.1 for the f-$WS_2$ and f-BN nanoparticles treated for 20 and 70 min, respectively. The carbon and oxygen signals in the W 4f spectrum of the f- $WS_2$ are not as strong as in the Mo 3d spectrum of the f-$MoS_2$ or the B 1s spectrum of the f-BN, indicating a lower degree of functionalization, which is attributed to the fact that the f- $WS_2$ was treated for a shorter duration (20 min cf. 70 min).

The Gaussian multi-peak fitting shows the respective chemical bonds. In the upper portion of (c), characteristic W $4f_{7/2}$ and W $4f_{5/2}$ peaks are observed for the untreated $WS_2$ flakes. After treated, it is seen in the lower portion of Figure 3.7 (c) that both W 4f intrinsic peaks are reduced and shifted to slightly lower energies, consistent with the introduction of foreign atoms[176]. Two W-C peaks appear at 30.2 eV and 32.3 eV[177], as well as a smaller peak at 37.2 eV that is attributed to W-O bonds[178]. The sulphur in the $WS_2$ demonstrates a strong affinity to bond with atoms from the solvent. The S 2p XPS spectra of $WS_2$ and f- $WS_2$ in Figure 3.7 (d) revealed C-$SO_x$ peaks after laser treatment[173–175]. As for f-$MoS_2$, the f-$WS_2$, S $2p_{3/2}$, and S $2p_{1/2}$ peaks were found to broaden and shift to slightly lower binding energies due to interaction with carbon and oxygen[44,179,180] as observed in Figures 3.7 (b) (d). In the lower portion of Figure 3.7 (e) it is seen that for BN the fs laser treated creates additional peaks in the B1s binding energy range at 191 eV and 192 eV, which are attributable to $BC_3$ and B-O respectively[37,181,182]. Similarly, additional peaks appeared in the N1s binding energy range at 399.1 eV and 399.3 eV, which are attributed to the formation of N=O and N=C/N-C bonds in the f-BN[37,183].

Table 3.1 – Deconvolution of Gaussian peaks fitted to the XPS spectra.

| | | | | | | | | | | | |
|---|---|---|---|---|---|---|---|---|---|---|---|
| f-$MoS_2$ | Mo 3d | **S 2s** | **Mo $d_{5/2}$** | **$MoO_x$** | **$MoO_2$** | **$Mo_2C$** | **$MoO_3$** | **Mo $d_{3/2}$** | **$MoO_2$** | **$MoO_x$** | **$MoO_3$** |
| | (225-240eV) | 3% | 17.8% | 4.6% | 4.5% | 30.9% | 2.3% | 15.8% | 14.8% | 2.2% | 3.8% |
| | S 2p | **S $2p_{3/2}$** | **S $2p_{1/2}$** | **C-$SO_x$** | | | | | | | |
| | (160-175eV) | 12.1% | 29.4% | 58.5% | | | | | | | |
| f-$WS_2$ | W 4f | **W $4f_{7/2}$** | **W $4f_{5/2}$** | **W-C** | **W-O** | | | | | | |
| | (30-40eV) | 39% | 33.5% | 24% | 3.5% | | | | | | |
| | S 2s | **S $2p_{3/2}$** | **S $2p_{1/2}$** | **C-$SO_x$** | | | | | | | |
| | (160-175eV) | 14.5% | 9% | 76.5% | | | | | | | |
| f-BN | B 1s | **B-N** | **B-$C_3$** | **B-O** | | | | | | | |
| | (185-195eV) | 57% | 27% | 16% | | | | | | | |
| | N1s | **N=B** | **N=C** | **N=O** | | | | | | | |
| | (396-402eV) | 18% | 52% | 20% | | | | | | | |

*Structural analysis*

Raman spectroscopy shed light on the structural and bond properties of the laser treated nano particles, which further confirmed the functionalization of the 2D nanoparticles with carbon and oxygen. Figure 3.8 illustrates the Raman spectroscopy of the all three materials before and after laser treatment. As observed in the upper portion of Figure 3.8 (a), two characteristic modes of vibration were detected for the untreated $MoS_2$ flakes, namely in-plane ($E^1_{2g}$) and out-of-plane ($A_{1g}$) vibrations at 381 $cm^{-1}$ and 409 $cm^{-1}$, respectively.

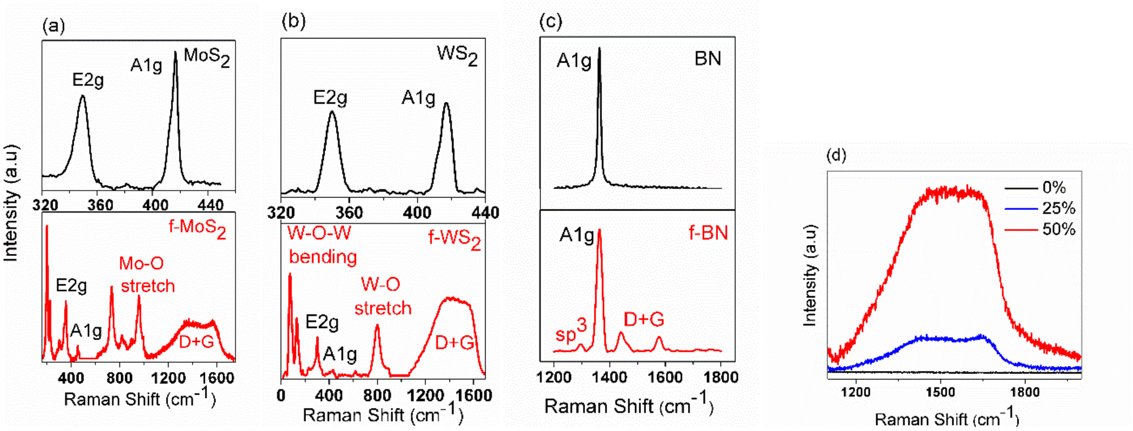

Figure 3.8 – Raman spectra of (a) $MoS_2$ (b) $WS_2$ (c) BN before (upper) and after 70 min treatment (lower) and (d) Raman spectra of $MoS_2$ after 70 min treatment in ethanol–water solutions with different ethanol concentrations (0–50%). Reproduced with permission from Ibrahim *et al.* Simultaneous Fabrication and Functionalization of Nanoparticles of 2D Materials with Hybrid Optical Properties. **1701365**, 1–7 (2018). Copyrights 2018 Wiley-VCH.

After fs laser treatment for 70 min, the out-of-plane peak redshift slightly to 406.5 $cm^{-1}$ (lower portion of Figure 3.8 (a)), which could be attributed to dopant-induced softening of the vibrational band, consistent with previous reports analyzing bilayer doped $MoS_2$[184]. This shift could also be attributed to the transition of the bulk material toward monolayer, for which a smaller Raman shift between the $E^1_{2g}$ and $A_{1g}$ modes is expected[185]. However, negligible shifting of the in-plane ($E^1_{2g}$) peak was observed at 381 $cm^{-1}$. The peaks were also found to broaden after laser treatment due to covalent functionalization, consistent with that reported previously for $MoSe_2$[44]. Crucially, prominent D + G peaks characteristic of C=C vibrations were observed at ≈1300–1580 $cm^{-1}$,[40,172] which indicate the presence of carbon domains in the 2D f- $MoS_2$ nanoparticle, consistent with the TEM and XPS analysis. The f- $MoS_2$ spectrum also shows peaks attributable to S compounds, Mo-O bending, C-S bond vibration, Mo-$O_2$ vibration, C-S bond vibration, and Mo-O stretching at 200, 335, 748, 835, 940, and 985 $cm^{-1}$, respectively[186,187], all indicative of the introduction of carbon and oxygen onto the $MoS_2$ nanoparticle.

For all three materials, the emergence of D+G and oxygen-related Raman peaks were accompanied by a reduction in the intensity of the intrinsic peaks ($A_{1g}$ and $E^1_{2g}$).

This is consistent with the mechanism outlined in Figure 3.4, where laser-induced damage to the intrinsic 2D material occurs simultaneously with functionalization of the formed nanoparticles with carbon domains as well as some oxygen atoms.

To confirm the source of carbon for the functionalization of the 2D nanoparticles, $MoS_2$ flakes were treated for 70 min in solutions with three different ethanol concentrations. Alongside a clear change in solution color, the intensities of the Raman D + G peaks, which indicate the presence of graphene-like carbon domains in the 2D nanoparticles, were observed to correlate directly with the ethanol concentration, as shown in Figure 3.8 (d), confirming the solvent as the source of the functionalities.

Hence, the solvent dictates what type of atoms are available to functionalize the 2D nanoparticles, and the degree of functionalization can be controlled via the solvent concentration, providing the opportunity to finely tune the properties of the 2D hybrid nanoparticles. The organic nature of the functionalities, namely C and O, resulted in an increased solubility of the nanoparticles in the aqueous solutions, which is beneficial for some applications (e.g., cell interactions in biomedical applications[37]). No precipitates were observed in the treated solutions after storage for several weeks.

Raman spectra of $WS_2$ before and after 20 min treatment, and BN before and after 70 min treatment, both in 1:1 water-ethanol solvents are shown in Figure 3.8 (b) (c). Untreated $WS_2$ flakes displayed in-plane ($E^1_{2g}$) and out-of-plane ($A_{1g}$) vibrations (peaks centered at 348 $cm^{-1}$ and 419 $cm^{-1}$ in the upper portion of (b)) corresponding to the 2H-phase[188], which softened after nanoparticle formation and functionalization (red shifting to 335 $cm^{-1}$ and 417.5 $cm^{-1}$ in the lower portion of (b)). D+G peaks were again detected at 1300-1580 $cm^{-1}$, indicating the presence of graphene-like domains in the f- $WS_2$[84], and peaks attributable to the bending of W-O-W at 85 $cm^{-1}$ and 130 $cm^{-1}$, as well as W-O stretching at 800 $cm^{-1}$, confirm the introduction of oxygen into the 2D f- $WS_2$ nanoparticles[84]. Untreated BN flakes displayed a single Raman peak at 1380 $cm^{-1}$, attributable to in-plane vibration of the B-N molecule (upper part of (c))[189]. This peak shifted slightly to 1385 $cm^{-1}$ following fs laser treatment (lower part of (c)), consistent with the material transitioning towards monolayer behavior[190]. The peak that emerges at 1295 $cm^{-1}$ has been observed previously for other nanostructured forms of BN and is attributed to sp3-bonding[191]. Additionally, D+G peaks are again observed in the 1200-1600 $cm^{-1}$ range for f-BN.

### 3.3.2 – Optical properties

The normalized absorbance spectra of the untreated $MoS_2$ flakes and f-$MoS_2$ nanoparticles formed after 70 min of treatment are shown in Figure 3.9. The untreated $MoS_2$ absorbance spectrum (black line) includes broad absorption at wavelengths below 500 nm (peak C), which has been observed previously and assigned to direct transitions in between the Γ and K points (point M) of the Brillouin zone[192]. Two maxima at 600 and 660 nm (known as peaks B and A) correspond to excitonic transitions at the K point of the Brillouin zone. They are known to arise from direct transitions between the splitting of the valence band and the minimum of the conduction band[193]. Another weak peak at 780 nm (peak I) is attributed to an indirect transition[194]. The f- $MoS_2$ nanoparticles (red line in Figure 3.9 (a)), in contrast, illustrate weak A and B peaks (shown in the inset) that are redshifted to 690 and 630 nm.

The reduced intensity of the A and B peaks is expected and is attributed to the transition from nanosheets to nanoparticles (introduction of lateral quantum confinement), as observed previously[195–197]. However, the observed redshift is in contradiction to the small blueshift that is expected due to quantum confinement, as observed for $MoS_2$ nanoparticles produced in pure water[82]. It is possible that the interaction of the carbon domains with the $MoS_2$ may result in a redshift of the intrinsic $MoS_2$ peaks, similar to that reported previously for n-doping of $MoS_2$[184]. An additional weak peak (peak I) is observed for the f- $MoS_2$ at 840 nm (inset of Figure 3.9(a)), which may be attributable to a small amount of indirect absorption. Transition metal dichalcogenides like $MoS_2$ and $WS_2$ are known to transition from an indirect band gap in 3D to a direct band gap in the 2D monolayer limit. The presence of a weak indirect absorption would be consistent with the formation of a mixture of mono, bi, and tri-layer nanoparticles, as suggested by the AFM analysis. Alternatively, $MoS_2$ is known to contain a higher density of trap states, compared for example with $WS_2$, such that the peak at 840 nm could also be attributed to traps in the f- $MoS_2$ nanoparticles[198].

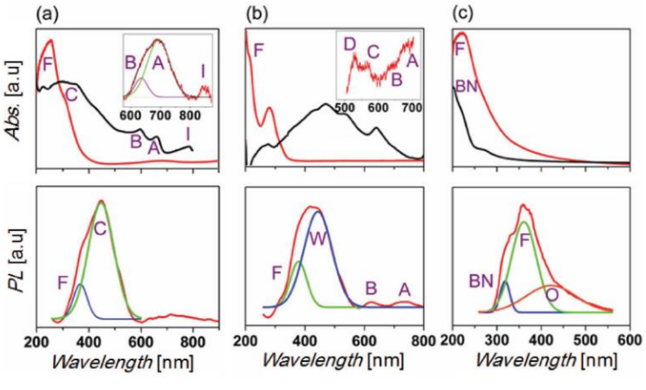

Figure 3.9 – Normalized absorbance and photoluminescence (PL) spectra. a) f-$MoS_2$ for 70 min, b) f-$WS_2$ for 20 min, and c) f-BN for 70 min. The UV–vis absorbance before (black) and after (red) laser treatment is shown in the upper panels. Photoluminescence (lower panels) was measured using 260 nm excitation. Reproduced with permission from Ibrahim *et al.* Simultaneous Fabrication and Functionalization of Nanoparticles of 2D Materials with Hybrid Optical Properties. **1701365**, 1–7 (2018). Copyrights 2018 Wiley-VCH.

The strongest absorption for the f-$MoS_2$ occurs at wavelengths below 400 nm. A broad absorption peak below 400 nm has been observed previously for $MoS_2$ quantum dots and attributed to blue shifted convoluted Z, C, and D excitonic peaks[190,199]. Previous reports have indicated that peak C blueshifts to a limit of ≈310 nm[195,200]. Indeed, Figure 3.10 shows that treatment of the $MoS_2$ flakes in water results in a maximum blueshift of peak C to 320 nm. In contrast, the f-$MoS_2$ in Figure 3.9 (a) shows an intense peak centered at 260 nm that has a different spectral shape than the $MoS_2$ treated in water as well as a shoulder at 310 nm that is consistent with the characteristic $MoS_2$ absorbance peak C. This new absorption feature at ≈260 nm in the f-$MoS_2$ (labeled F in Figure 3.9 (a)) is attributed to the carbon domains decorating the nanoparticles, as carbon nanomaterials are frequently reported to display a characteristic absorption peak in the 215–270 nm range[201–203]. The carbon absorption in the 2D hybrid nanoparticles appears to be stronger than the intrinsic $MoS_2$ absorption, which can be attributed to carbon's higher carrier density and the large amount of carbon incorporated into the particles, as observed by XPS.

Consistent with the weak absorption observed in the 600–900 nm range for the f-$MoS_2$, only weak photoluminescence is observed in this range for the f- $MoS_2$ in the lower part of Figure 3.9 (a), attributable again to a reduction in the lateral dimensions of the $MoS_2$ nanoparticles[195]. The photoluminescence of the f-$MoS_2$ is dominated by a peak at 450 nm, with a shoulder at 370 nm. The peak at 450 nm (peak C) is characteristic of the blue emission of $MoS_2$[198,204]. The emission at 370 nm (peak F) is consistent with that observed for graphene quantum dots[205], and is therefore attributed to the carbon domains. Thus, the emission at 370 nm results from the high-energy absorption that was observed in the upper portion of Figure 3.9 (a) (peak F).

This was confirmed by measuring the photoluminescence of $MoS_2$ sheets treated in water in an identical manner as shown in Figure 3.10 (b). Just as the absorption peak at 260 nm was not observed in Figure 3.10 (a) when a water solution was used, no photoluminescence shoulder at 370 nm was observed in the absence of carbon functionalization. Thus, the 2D f-$MoS_2$ nanoparticles produced with this technique display hybrid optical properties, where absorption and photoluminescence from both the $MoS_2$ and added carbon domains are observed. To our knowledge, this is the first time that this dual absorption and emission has been observed for these functionalized 2D nanoparticles.

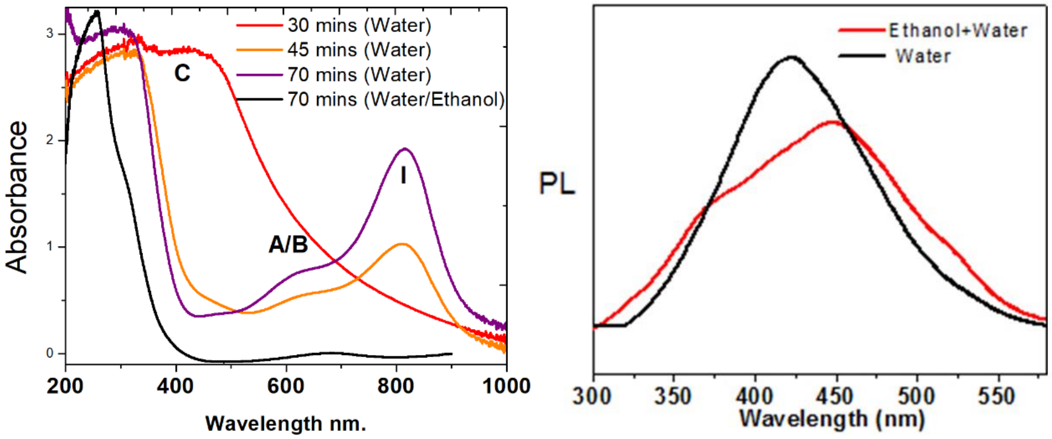

Figure 3.10 – (a) UV visible absorbance spectra comparison between laser treated f-$MoS_2$ suspended in water and water-ethanol (b) Photoluminescence spectra for $MoS_2$ treated for 70 min in water and 1:1 water-ethanol solvents. Reproduced with permission from Ibrahim *et al.* Simultaneous Fabrication and Functionalization of Nanoparticles of 2D Materials with Hybrid Optical Properties. **1701365**, 1–7 (2018). Copyrights 2018 Wiley-VCH.

Normalized absorbance spectra of $MoS_2$ treated in water for durations of 30 to 70 min and 1:1 water-ethanol for 70 min. The absorbance spectra of the $MoS_2$ treatment in water show a blue shifting of the “C” absorption peak to a minimum value of 320 nm (2.9 eV). This is attributed to quantum confinement, as reported previously[195], consistent with the $MoS_2$ size being reduced from micron-scale flakes to nanoparticles with dimensions of approximately 3 nm. In contrast, the absorption of the f-$MoS_2$ treatment in a 1:1 water/ethanol solution (also shown in Figure 3.9 (a)) is shifted to lower energies and has a different spectral shape. A slight blue shift of the A/B peaks (from 630 to 610 nm) resulting from quantum confinement is observed as well for the 45 min and 70 min water solutions. A broad peak is also observed at 820 nm for the $MoS_2$ treatment for 45 and 70 min in water, consistent with the indirect (I) absorbance discussed in the main text. These features are similar to absorbance features previously reported for $MoS_2$ nanoparticles[194,195].

The functionalized $WS_2$ and BN nanoparticles similarly showed hybrid optical properties, with characteristics of both the intrinsic materials and the added carbon domains. The absorbance spectrum for untreated $WS_2$ flakes (shown in black in the upper portion of Figure 3.9(b)) shows a series of peaks centered at 420, 480, 535, and 640 nm (known as peaks D, C, B, and A respectively), which correspond to direct transitions at the K-point of the Brillouin zone[84]. A plasmon peak at 270 nm was also observed and has previously been attributed to the metallic nature of $WS_2$ resulting from surface defects[84]. The spectrum of f- $WS_2$ treated for 20 min is shown in red in the same figure. The plasmon peak is found to increase in intensity, consistent with an increase in defect density caused by the laser. A carbon absorption peak F was located at 215 nm, consistent with previous reports[202,203]. The carbon peak position is different than that observed for f- $MoS_2$ (260 nm), which may be due to the smaller amount of carbon present in the f- $WS_2$ that was treated for only 20 min. Similar to the f- $MoS_2$, peaks A, B, C, and D are still present in the f- $WS_2$ absorption spectrum (shown in the inset of Figure 3.9 (b)) but are much weaker and redshifted to 530, 565, 620, and 670 nm, respectively, which again may be due to the addition of carbon domains to the $WS_2$ nanoparticle. The f- $WS_2$ showed a photoluminescence peak centered at 450 nm namely; peak W in the lower panel of Figure 3.9 (b), which is consistent with intrinsic $WS_2$ emission[206,207] as well as a similar shoulder emission at 380 nm resulting from the carbon domains. Two weak peaks at 630 and 730 nm (excitonic peaks B and A) are also observed for the f- $WS_2$.

Not a transition metal dichalcogenide, BN does not exhibit absorption/emission in the 600–800 nm range. Shown in the upper portion of Figure 3.9 (c) and in line with previous reports[208,209], untreated BN flakes (shown in black) exhibit a sharp peak at ≈190 nm (6.5 eV) and a shoulder at 260 nm ascribed to donor–acceptor pair transitions involving native defects in BN such as nitrogen vacancies[210]. After treatment for 70 min, the f-BN spectrum also shows absorption due to π–π transitions in the carbon domains, as seen in peak F at 225 nm. The photoluminescence spectrum of f-BN in the lower portion of Figure 3.9 (c) showed three modes of emission, a central peak F at 380 nm, again attributed to emission from the carbon domains, and one shoulder on either side. The emission at 330 nm (peak BN) is attributed to nitrogen and boron vacancies in the f-BN nanoparticle[37], and the shoulder centered at 450 nm (peak O) has been previously attributed to oxygen impurity emission[37], consistent with the introduction of oxygen atoms, as seen in the XPS and Raman measurements.

The absorbance spectrum of laser-treated ethanol (without flakes of 2D materials) was also examined to assess the possible contributions of the solvent to the observed optical properties. A carbon peak below 220 nm was observed after the treatment of ethanol, as shown in Figure 3.11. While the appearance of this peak supports the proposed mechanism in Figure 3.4 (dissociation of solvent molecules by laser treatment), the peak did not match those observed in Figure 3.9. Combined with the fact that the absorption and emission spectral features in Figure 3.9 differ for f-$MoS_2$, f-$WS_2$, and f-BN as well as the TEM, XPS, and Raman characterization that indicate the attachment of functionalities to the nanoparticles, it can be concluded that the observed optical properties are dominated by the functionalized nanoparticles.

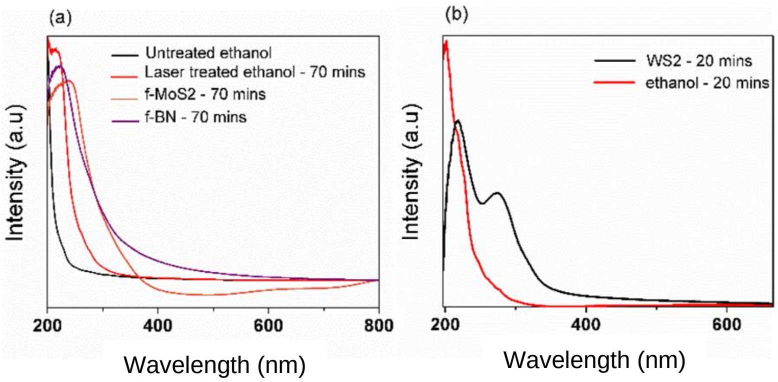

Figure 3.11 – UV Visible Absorbance spectra of (a) untreated ethanol, ethanol treated for 70 minutes, and f-$MoS_2$ and f-BN solutions treated for 70 minutes, (b) ethanol treated for 20 minutes and f-$WS_2$ treated for 20 minutes. Reproduced with permission from Ibrahim *et al.* Simultaneous Fabrication and Functionalization of Nanoparticles of 2D Materials with Hybrid Optical Properties. **1701365**, 1–7 (2018). Copyrights 2018 Wiley-VCH.

The laser-treated ethanol shows a carbon peak at approximately 220 nm compared to the untreated ethanol in Figure 3.11 (a), providing confirmation that the laser treatment creates reactive dissociated species from the solvent. The peaks observed in the f-$MoS_2$ and f-BN spectra in (a) have different positions and FWHM than the peaks observed in the laser-treated ethanol, indicating that they do not correspond to the unbonded carbon domains in solution. Similarly, in Figure 3.11 (b) the f-$WS_2$ peaks have different positions and FWHM than the peaks observed in the laser-treated ethanol, indicating that they do not correspond to the unbonded carbon domains in solution if the observed optical properties were dominated by unbonded carbon domains, a similar carbon spectral feature for the different 2D materials is expected, were laser-treated in identical ethanol solutions. Combined with the XPS, Raman, and TEM results that demonstrate bonding of the carbon to the nanoparticles, these results strongly suggest that the observed optical properties are dominated by the functionalized nanoparticles.

Thus, the laser treatment was found to introduce new absorption and photoluminescence peaks, which could prove beneficial for both sensing and light-emitting applications, among others. Importantly, the degree of functionalization can be directly tailored by adjusting the solvent concentration as shown in Figure 3.8(d) or treatment time. To demonstrate this, the absorption edge was tuned for all three materials by adjusting the treatment time, as shown in Figure 3.12.

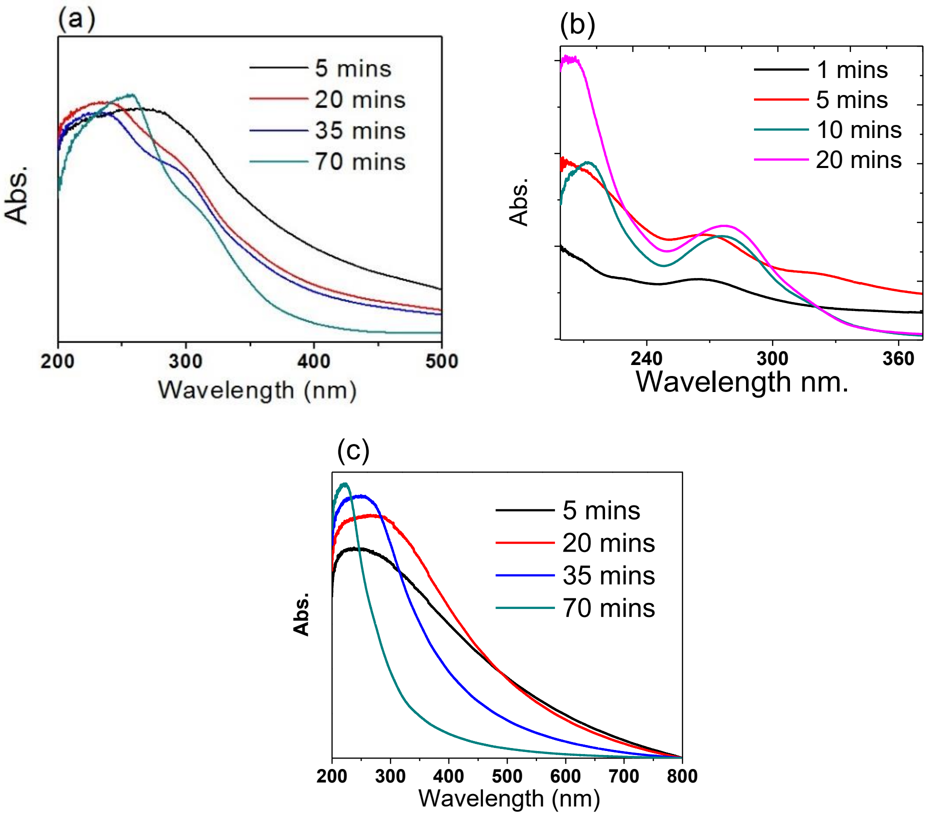

Figure 3.12 – Tuning of the absorption edge of (a) f-MoS$_2$, (b) f-WS$_2$, and (c) f-BN by treatment for different durations in a 1:1 water-ethanol solvent. Reproduced with permission from Ibrahim *et al.* Simultaneous Fabrication and Functionalization of Nanoparticles of 2D Materials with Hybrid Optical Properties. **1701365**, 1–7 (2018). Copyrights 2018 Wiley-VCH.

# 4.0 – Enhancement of PSC stability via halogenated 2D particle incorporation

---

---

## Synopsis

Herein, the method presented in chapter 3.0 of this dissertation is used to functionalize graphene with halogens before implementing them in the HTL of perovskite solar cells. Incorporation of the functionalized nanoparticles results in an enhancement in both the long-term stability and power conversion efficiency of the solar cells.

## 4.1 – Experiments and methodology

### 4.1.1 – Fabrication of functionalized graphene particles

Motivated by the hydrophobic properties exhibited by halogen-doped carbon-based materials and their ability to positively impact both the PSC efficiency and long-term stability[132], chlorinated graphene and iodinated graphene particles were fabricated using femtosecond laser treatment. Inspired by the approach developed in chapter 3.0 for creating functional materials, chlorinated and iodinated graphene were fabricated, with chlorobenzene employed as the source of chlorine and sodium iodide as the source of iodine.

For simplicity, chlorinated graphene will be referred to here as Cl-G, and iodinated graphene will be referred to as I-G. To create the Cl-G, multilayer graphene powder purchased commercially from Graphene Supermarket, 1-2 micrometers in lateral size, was dispersed in chlorobenzene at a concentration of 1 mg/mL and 4 mL of the solution was treated in a glass vial using the femtosecond laser. To create I-G, 0.01 mg/mL of sodium iodide was added to the solution used to create the Cl-G. The high intensity laser treatment was employed to aid in dissociating the chlorobenzene solvent and sodium iodide molecules. A laser energy of 1 mJ, central wavelength of 800 nm, pulse width of 35 femtoseconds, and repetition rate of 1 kHz were used. The beam focal point was set at a 0.5 cm depth below the air/solution interface with a focal length of 5 cm. The solutions were treated for 70 mins and constantly stirred using a magnetic stirrer rotating at 200 rpm to maintain their homogeneity and to ensure no sodium iodide precipitated to the bottom of the vial for the I-G solution.

As in chapter 3.0, the laser treatment is expected to break the graphene sheets into smaller particles and simultaneously dissociate the chlorobenzene and sodium iodide molecules, as shown in the schematic in Figure 4.1. The dissociated chlorine and iodine atoms can bond with the fragmented graphene in locations rich with unsatisfied bonds, resulting in functionalization of the periphery of the graphene particles.

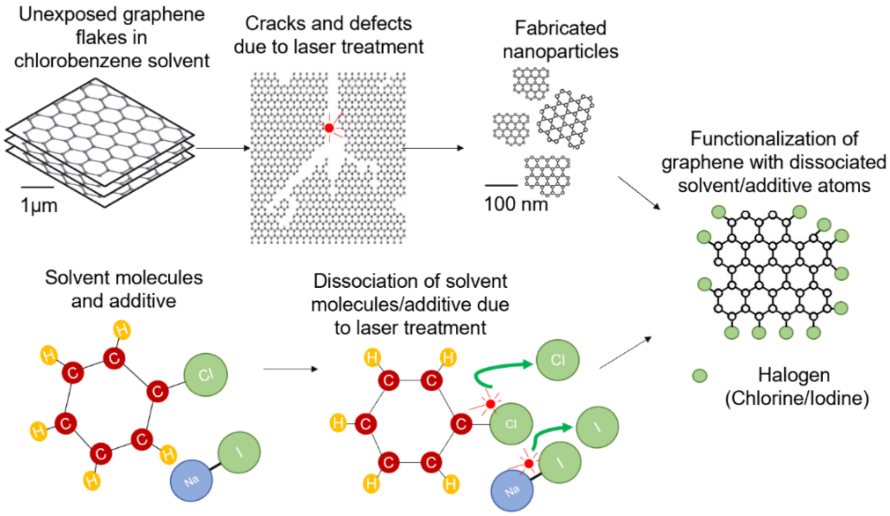

Figure 4.1 – Schematic illustrating the laser treatment simultaneously reducing the size of the graphene flakes and dissociating the chlorobenzene and sodium iodide molecules, in turn functionalizing the graphene particles.

### 4.1.2 – Perovskite fabrication

Perovskite solar cells with a glass/FTO/Li-doped $TiO_2$/perovskite/spiro-OMeTAD /Ag architecture were fabricated. The effect of adding Cl-G and I-G to the spiro-OMeTAD hole transport layer on the long-term stability and performance of the perovskite solar cells was investigated. Two strategies for stability enhancement were adopted in this study; using Cl-G and I-G as (i) additives inside the HTL with a ratio of 80-spiro-OMeTAD:20-Graphene and (ii) thin encapsulating layers covering the HTL.

The electron transport layer lithium doped titanium dioxide ($TiO_2$) was fabricated on commercial glass/FTO substrates. 73.2 µL of titanium diisopropoxide bis(acetylacetonate) was suspended in 1500 µL of butyl alcohol then 50 µL of the resultant solution was spin coated on the FTO substrate at a speed of 4000 rpm for 10 seconds three times. The samples were then annealed at 450°C for 30 mins in air and left to cool down to room temperature. To dope the layer with lithium, 50 µL of lithium salt in acetonitrile solvent (at 10 mg/mL concentration) was spin coated at 3000 rpm for 10 seconds, followed by sintering at 450 °C for 30 mins in air. After the substrates cooled down to 150 °C, they were inserted into a glovebox (nitrogen environment) to deposit the active layer; perovskite.

The perovskite solution was fabricated by mixing 76% of solution A; 25.639 mg/mL of cesium Iodide (CsI), 214.96 mg/mL of formamidinium iodide (FAI), and 645.88 mg/mL of lead iodide ($PbI_2$) (all suspended in dimethylformamide (DMF)) with 24% of solution B; 15.6 mg/mL of guanidinium iodide (GAI) in dimethyl sulfoxide (DMSO) solvent. 50 µL of the perovskite solution was deposited on the lithium doped $TiO_2$ film and spin coated for 30 seconds (1000 rpm for the first 10 seconds and 6000 for the remaining 20 seconds). 300 µL of antisolvent comprised of 50:50 chlorobenzene and chloroform was dynamically spin coated at the 26th second of the perovskite 30 second spin. The samples were then quickly moved to a hot plate at 140°C for 30 mins.

The hole transport material; Tetrakis[N,N-di(4-methoxyphenyl)amino]-9,9′-spirobifluorene (spiro-OMeTAD) was prepared by mixing 1000 µL of 85.78 mg/mL of spiro-OMeTAD in chlorobenzene, 18 µL of 60:40 solution 4-tert-butylpyridine (TBP): chlorobenzene, 18 µL of lithium salt at 287.01 mg/mL in acetonitrile, and finally 4 µL of cobalt bis(trifluoromethanesulfonyl)imide (TFSI) with a concentration of 375.8 mg/mL in acetonitrile. For the control devices, 50µL of the spiro-OMeTAD solution was dynamically spin coated for 10 seconds. For the HTLs with the I-G and Cl-G additives, a mixture of 40 µL of spiro-OMeTAD solution and 10 µL of the Cl-G or I-G solution was dynamically spin coated at 4000 rpm for 10 seconds. For the devices with the Cl-G and I-G encapsulation layers, the spiro-OMeTAD solution was spin coated (as in the preceding recipes) then 50 µL of the Cl-G or I-G solution was dynamically spin coated at 2500 rpm for 15 seconds. All of the solutions used in the above fabrication procedures were filtered using 0.4 µm micropore solution filters. Schematic of the fabricated devices are shown below in Figure 4.2.

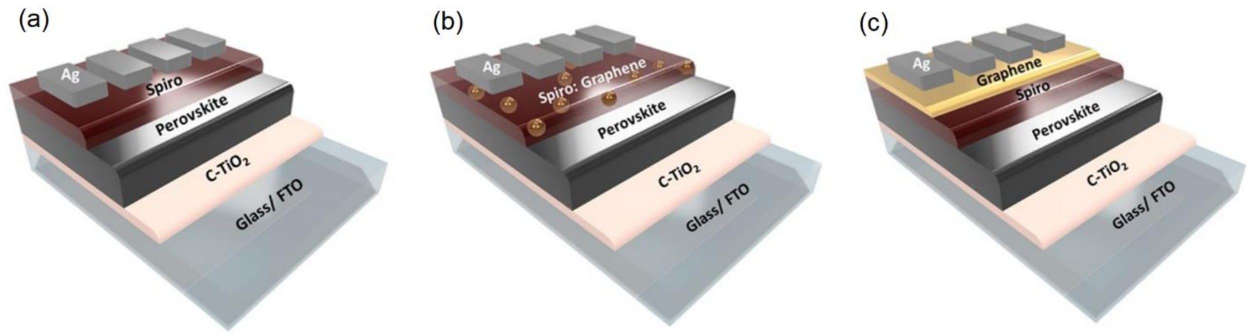

Figure 4.2 – Schematic of fabricated perovskite solar cells with (a) 100% spiro-OMeTAD (b) spiro-OMeTAD with Cl-G/I-G additives, (c) Cl-G/I-G layer.

### 4.1.3 – Material characterization

SEM images were captured using a Zeiss Leo 1530 and electron high tension (EHT) of 5 kV. XPS samples were measured on silicon substrates and the Si 2p transition was used for binding energy calibration. Spectral analysis was performed by deconvoluting Gaussian multipeak fits. Contact angle measurements were conducted by applying a droplet (~ 5 µL) of DI water on the respective graphene films dynamically spin coated at 4000 rpm, and the contact angles were measured using imageJ[211], an image processing software. PL spectra were collected with a Horiba Quantamaster by testing the full sample setup shown in Figure 4.2 without the silver electrodes. The samples were excited at 680 nm and scanned from 810 nm to 850 nm. The Raman spectroscopy was carried out for each sample using a Renishaw micro-Raman spectrometer on a drop casted film on a Silicon substrate and an excitation wavelength of 632.8 nm and power of 20 mW were used.

### 4.1.4 – Solar cell characterization

To assess the PSC stability at ambient conditions the samples were stored in a dark cabinet without encapsulation. A humidity sensor was used to record the relative humidity (RH%). For testing the stability under severe humid conditions, the samples were inserted in an enclosed chamber at ~85% RH%. An air line blowing into a DI water flask generated humid air, which was fed to a humidity sensor before supplying the chamber with the necessary humid air. The absorbance for both ambient and humid cases was then measured using an Ocean Optics spectrometer.

Using a physical mask with an area of 0.105 $cm^2$, 250 nm thick silver electrodes were thermally evaporated using an Intlvac thermal evaporator to enable device testing. A Sciencetech UHE-NL-150 Class AAA Solar Simulator was used to conduct the measurements. The solar cell area was calculated to be 0.105 $cm^2$, an irradiance of 100 $mW/cm^2$ was set using a NIST-calibrated silicon reference solar cell, and the voltage was swept from 1.5 V to -0.1V with a sweep rate of 0.1 V/s.

## 4.2 – Material characterization

XPS was carried out on the laser treated Cl-G and I-G and compared to the untreated graphene, as shown below in Figure 4.3. The C 1s spectra shown below for both halogenated samples and untreated graphene show peaks owing to C=C sp2 hybridization and C-C sp3 hybridization observed at 284.4 eV and 285.3 eV respectively[212]. Laser treatment incurred clear composition changes evident in the absence of the C-O bond[212] located at 286.2 eV (oxygen incorporation was likely due to oxygen adsorption as a result of exposure to ambient conditions) in both halogenated samples, being replaced with carbon bonded halogens. The usage of chlorobenzene solvent as a precursor for chlorine functionalization for graphene was evident in Figure 4.3 (b) as the C-Cl bond[213] emerged at 286.6 eV. Similarly, the effect of the NaI additive was clear as the C-I bond[90] was observed at 286.3 eV in Figure 4.3 (c), while the effect of the chlorobenzene solvent also provided the C-Cl bond at 286.6 eV in the iodinated sample. The change in composition is observed below in Table 4.1.

The change in chemical composition primarily happens to the C-C, where the Cl-G sample showed a significant increase for the C-Cl bond peak at the expense of C-O and the C-C bond peaks. That illustrates the laser treatment's ability to functionalize the graphene particles with the Cl. For the I-G, in the presence of the NaI the I was able to form C-I bonds at the expense of half of the composition of C-Cl and the C-O.

Table 4.1 – Chemical composition of halogenated graphene at C1s.

| Sample | C=C | C-C | C-O | C-Cl | C-I |
|---|---|---|---|---|---|
| Untreated graphene | 61.01 | 26 | 12.99 | 0 | 0 |
| Cl-G | 61.90 | 21.24 | 0 | 16.85 | 0 |
| I-G | 66.90 | 16.31 | 0 | 8.1 | 8.69 |

The rise of the C-Cl and C-I bond peaks prompted the investigation of the I 3d and Cl 2p peaks shown below in Figure 4.3 (d–f). The I 3d binding energy region showed 2 peaks owing to I 3d 5/2 and I 3d 3/2 at 621.4 eV and 633 eV respectively. The deconvolution of the respective peaks of I 3d showed 2 peaks owing to triiodide $I_3^-$ at 621.4 eV and 632.9 eV and pentaiodide $I_5^-$ at 622.9 eV and 634.2 eV[90]. Being the dominant character, $I_3^-$ is known to have a linear symmetrical molecular structure[214]. The $I_3^-$ is mainly implanted on the surface of the graphene particles and likely edge functionalization due to the large iodine atomic size[89].

Despite the fact that iodine is a large halogen and hence more polarizable[215], the difference in electronegativity between iodine (2.66) and carbon (2.55) gives a smaller partial charge on the C-I bond compared to the C-Cl bond (due to higher electronegativity of 3.16 for Cl).

These results indicate that the iodination and chlorination of the graphene particles not only provides heteroatoms on the graphene surface and generates $I_3^-$ and $I_5^-$ but also reduces the oxygen functionalities adsorbed on the surface of the graphene sheets prior to laser treatment. This reduction proves key for decreasing the surface energy and enhancing the electrical properties of graphene[89].

Figure 4.3 (e–f) show the Cl 2p peaks indicating the presence of Cl 2 $p_{3/2}$ and 2 $p_{1/2}$ C-Cl bonds at 200 and 202.5 eV respectively. This confirms the successful functionalization of graphene with Cl atoms from the chlorobenzene. The different contributions of the C-Cl bonds are summarized in Table 4.1.

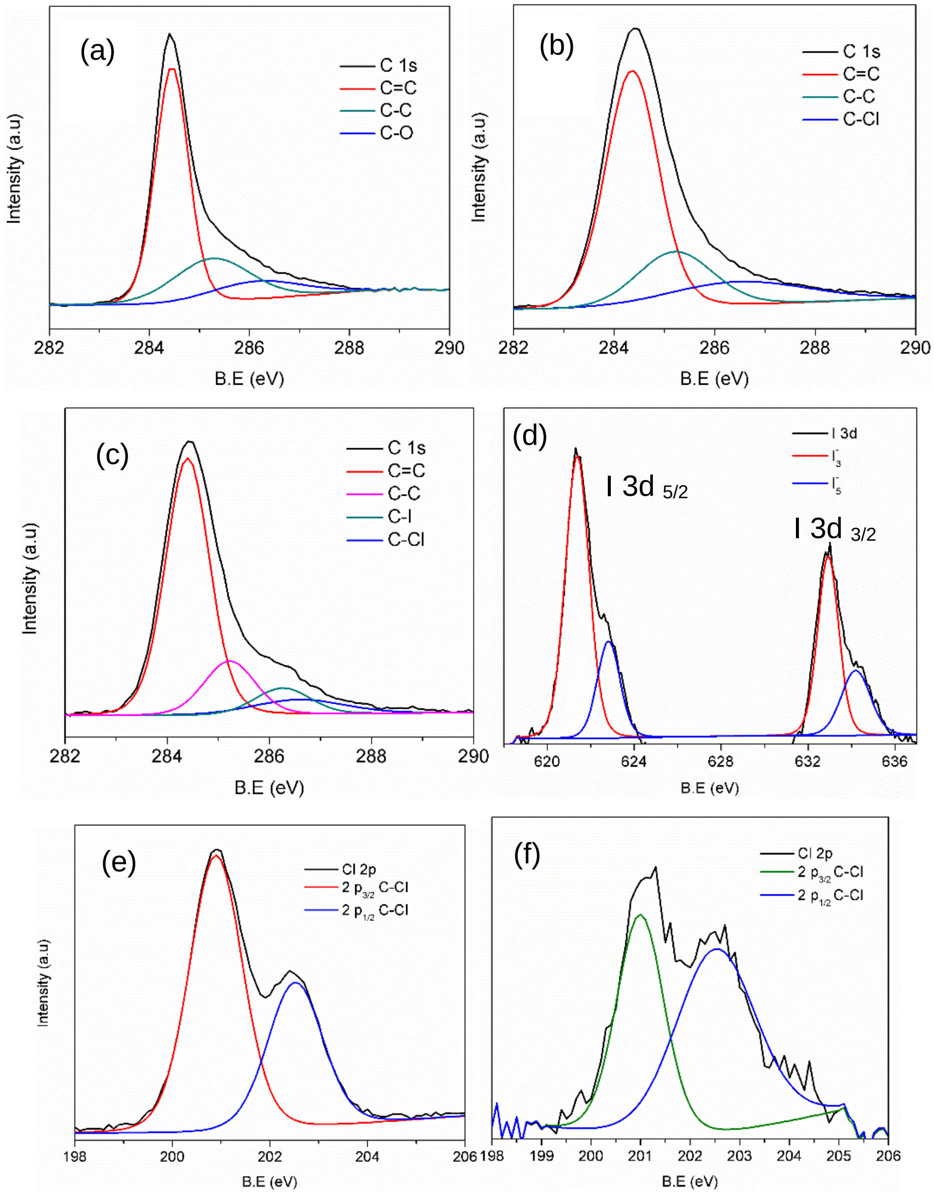

Figure 4.3 – XPS spectra for (a) C 1s peak untreated graphene (b) C 1s peak Cl-G, (c) C 1s peak I-G, (d) I 3d peak I-G, (e) Cl 2p peak Cl-G, and (f) Cl 2p peak I-G.

Raman spectroscopy was also conducted to investigate the effect of halogen functionalization on the graphene particle properties. Figure 4.4 below shows the Raman spectra for the untreated graphene sheets alongside Cl-G and I-G samples. The defect ratio ID/IG increased significantly from 0.09 for the untreated graphene to 1.41 and 1.51 for the Cl-G and I-G samples. This sharp increase is attributable to the increased functionalization by the halogen atoms and the graphene's modified properties. The broadening of the G peak for both halogenated samples is attributed to increased heteroatoms in the graphene honeycomb lattice[90]. Also the disappearance of the 2D peak is an indication of the C-Cl bonding[216] and a decrease in the number of layers. Significant blue shifting of the D peaks for both halogenated samples implies p-doping while the blue shifting of the G peak is indicative of lattice compression due to the incorporation of the halogen species[217]. The I-G sample blue shifting of the graphene peaks is indicative of possible charge transfer between the graphene particles and the guest iodine species, which coincides with previous reports of p-type doping and I-doped graphene[89].

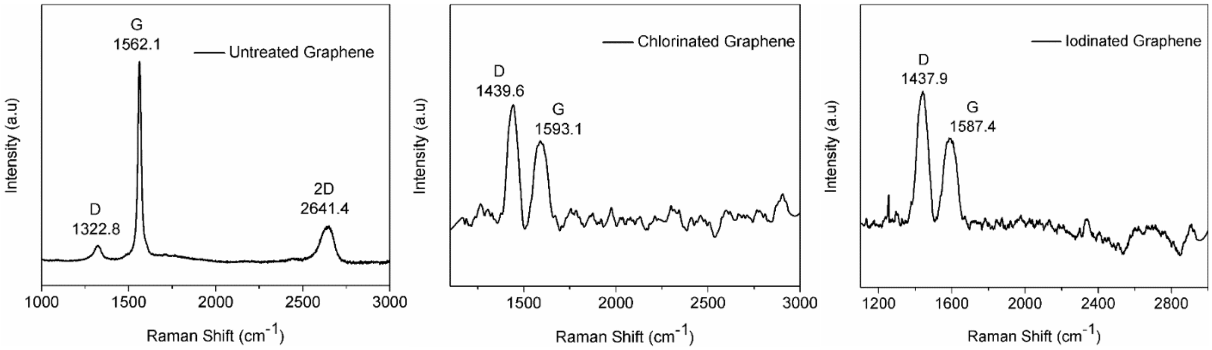

Figure 4.4 – Raman spectra for (a) untreated graphene sheets, (b) Cl-G, and (c) I-G samples.

SEM images of the three different HTL configurations are shown in Figure 4.5 (a–c) for the Cl-G. For the cells with Cl-G additives, the Cl-G particles were found to cover approximately 90% of the surface area. Areas with partial coverage are shown in Figure 4.5 (b) and (c) so that the underlying perovskite morphology can also be observed. Figure 4.5 (a) shows the perovskite grains with an average grain size of 200 nm. Figure 4.5 (b) shows the Cl-G additive-based sample, showing the Cl-G particles partially covering the surface of the perovskite grains. The fabricated particles were found to be 100-200 nm in lateral size. The Cl-G encapsulation-based sample is shown in Figure 4.5 (c), and the Cl-G particles can be seen forming the encapsulating film on the surface of the spiro-OMeTAD.  AFM images are shown in Figure 4.5 (d–f) where the average surface roughness of the additive and layer based Cl-G devices was found to be 5.7 +/- 0.5 nm and 8.8 +/- 0.8 nm respectively, compared to the device with spiro-OMeTAD only that had an average roughness of 1.4 +/- 0.2 nm.

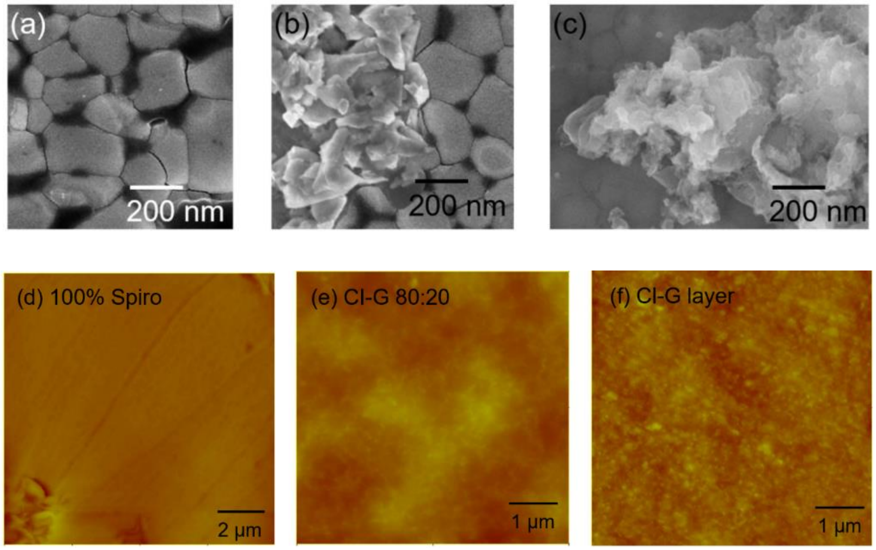

Figure 4.5 – SEM images of (a) spiro-OMeTAD on perovskite film, (b) Cl-G 80:20 additive to the spiro-OMeTAD, (c) Cl-G encapsulating layer. AFM images of (d) 100% spiro-OMeTAD, (e) Cl-G additive to the spiro-OMeTAD, (f) Cl-G as an encapsulating layer on the spiro-OMeTAD HTL.

Previous reports of halogen-doped carbon-based materials have shown an increase in water droplet contact angle indicating increased hydrophobicity[218,219]. The contact angles were measured for the fabricated particles to assess their hydrophobicity and are shown below in Figure 4.6. The contact angle of a water droplet was measured on a surface with identical film deposition parameters to that of the solar cells to simulate the real contact angle of water in the solar cell device. The contact angle of the untreated graphene was 37.2°, as shown in Figure 4.6 (a). The laser treatment's effect on the hydrophobicity the Cl-G film was evident as the contact angle increased to 145.1° by simply treating the graphene in chlorobenzene to functionalize it with chlorine, as shown in Figure 4.6 (b). Similarly, the I-G film showed super-hydrophobicity (contact angle > 150°) with a contact angle of 152.29° in Figure 4.6 (c). This can be attributed in part to the increased surface roughness for the I-G particles. The increased roughness indicates increased presence of air cavities, which play a role in increasing the hydrophobicity[220].

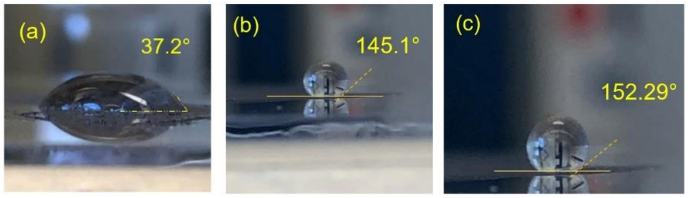

Figure 4.6 – Contact angle measurements of water droplet on (a) untreated graphene sheets, (b) Cl-G film (c) I-G film.

## 4.3 – Effect of chlorinated and iodinated graphene on perovskite solar cell stability

To test the effect of incorporating the halogen-doped particles in the PSC HTL on the long-term stability of the solar cells, we measured the absorbance degradation of the perovskite layer. As discussed in section 2.3, there are various routes for PSC degradation including illumination and metal electrode migration amongst other routes. Therefore, to attribute the degradation to a sole route, the samples were kept in the dark and with no metal electrodes deposited. The PSC decomposition was tracked by measuring the change in absorbance of the device in ambient conditions and severely humid conditions (~85% RH) without encapsulation. Figure 4.7 (a) shows the change in the perovskite's absorbance for the 100 % spiro-OMeTAD device and the Cl-G additive based device while they are kept in the moisture chamber at 85% RH. It is clear that the absorption spectra are much more stable for the Cl-G additive based device in Figure 4.7 (b), indicating minimal degradation of the perovskite layer

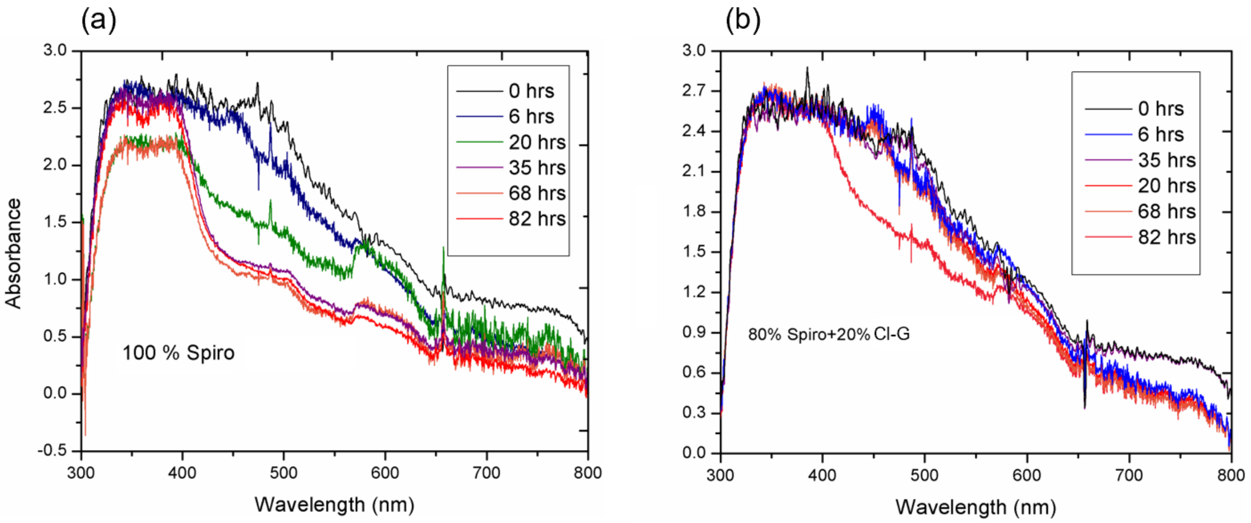

Figure 4.7 – Absorbance spectra change as a result of PSC devices being kept in 85% RH for (a) 100% spiro-OMeTAD and (b) Cl-G additive based device.

The perovskite absorption during storage in relative humidity between 30-40 RH% was observed across a ~2200 hr span. Absorbance for devices with different HTLs were compared to their initial absorbance measured at T=0 hrs, as shown below in Figure 4.8 (a). The absorbance of all the cells was found to decrease sharply in the initial 300-450 hrs of the stability test before the samples with the additives start to plateau. This contrasts with the control sample (100% spiro-

OMeTAD) where the sharp decrease continues until ~750 hrs and then plateaus at approximately 40% of the initial absorbance.

The samples with the additives showed vastly superior stability in ambient conditions in the long term, where the Cl-G and I-G encapsulated samples maintained an impressive 0.86 and 0.88 respectively of their initial absorbance. The additive based samples (80:20 Spiro: halogenated graphene) maintained 0.81 and 0.83 of their initial absorbance for Cl-G and I-G respectively. Thus the samples encapsulated with Cl-G and I-G layers showed a slightly better retention of the absorbance than the additive based samples, which can be attributed due to the fact that some areas in the HTL of the additive based samples have some uncovered areas with none of the hydrophobic graphene particles, hence making these samples decompose slightly faster. The images of the samples are shown before and after the 2200 h testing span in Figure 4.8 (b), where the degradation on the control sample compared to the graphene-based devices is evident.

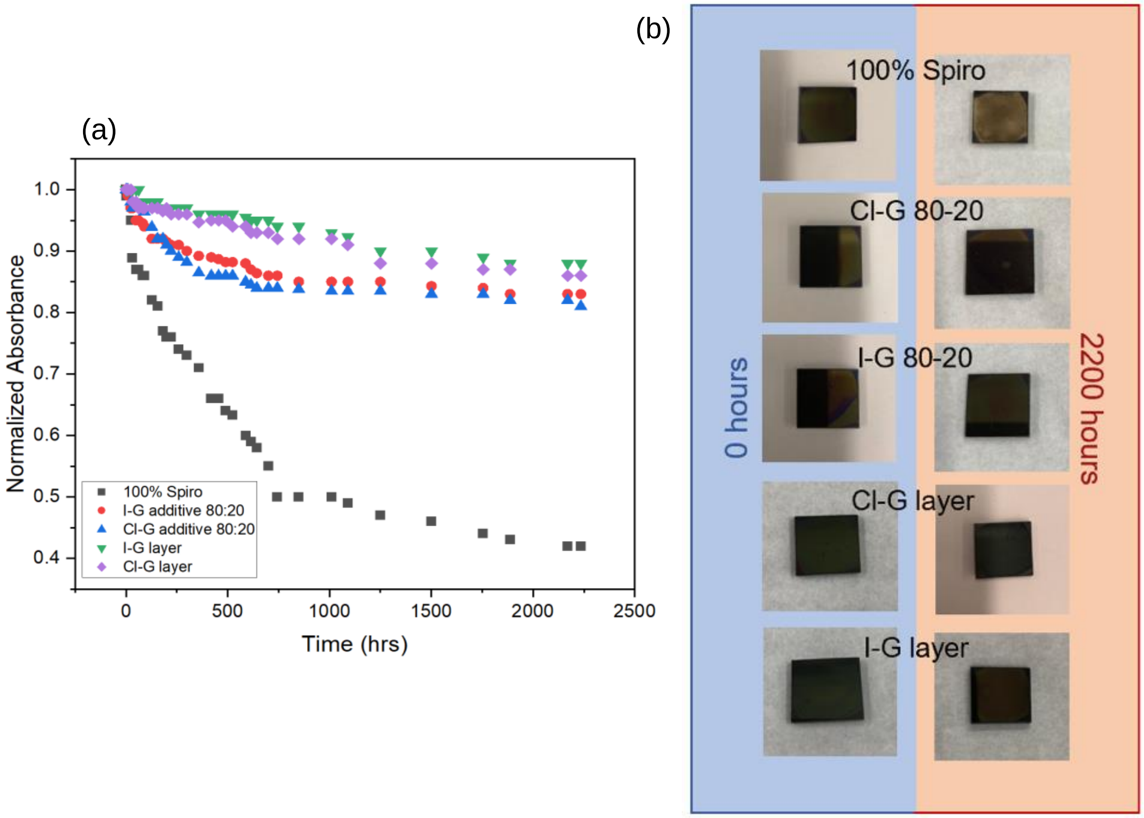

Figure 4.8 – (a) Degradation of the bare PSCs in ambient conditions over 2200 hrs testing period (absorbance at 550 nm), (b) Images of the samples at T=0 hrs and T=2200 hrs.

To further investigate the moisture stability of the fabricated PSCs, they were kept at ~85% relative humidity (RH) in an enclosed chamber and their absorbance was again monitored. Shown in Figure 4.9 (a) is the absorbance degradation of the 4 graphene-based devices compared to the control device (only spiro-OMeTAD as the HTL) in a 50-hr testing span.

The control device decomposed rapidly to almost 0.1 initial absorbance after 30 hrs, whereas the absorbance decreased to 0.68, 0.62, 0.74, and 0.79 of the initial absorbance at T=0 hrs for the I-G additive, Cl-G additive, Cl-G layer, and I-G layer PSC devices respectively. The stability performance is consistent with the contact angle measurements where the I-G based devices showed slightly higher contact angles than the Cl-G based devices. Figure 4.9 (b) shows the images of PSC devices at T=0 hrs and after the testing period at T=50 hrs. It can be observed that after the testing is complete, the control device (100% spiro-OMeTAD) is completely decomposed, whereas the Cl-G and I-G layer-based devices are in almost pristine condition.

However, the Cl-G and I-G additive based devices showed degradation in isolated spots on the surface of the samples. This is attributed to the fact that water molecules that can penetrate the sample to interact with the Lead compound in the perovskite may preferentially accumulate around the periphery of Cl/I-G particles (where its more hydrophilic). The water accumulation at these sites is susceptible to moisture penetration, specifically due to the lithium salt component in the spiro-OMeTAD. Therefore, the additive based devices degrade via this "spotting mechanism", as can be specifically seen for I-G 80-20 additive sample in Figure 4.9 (b).

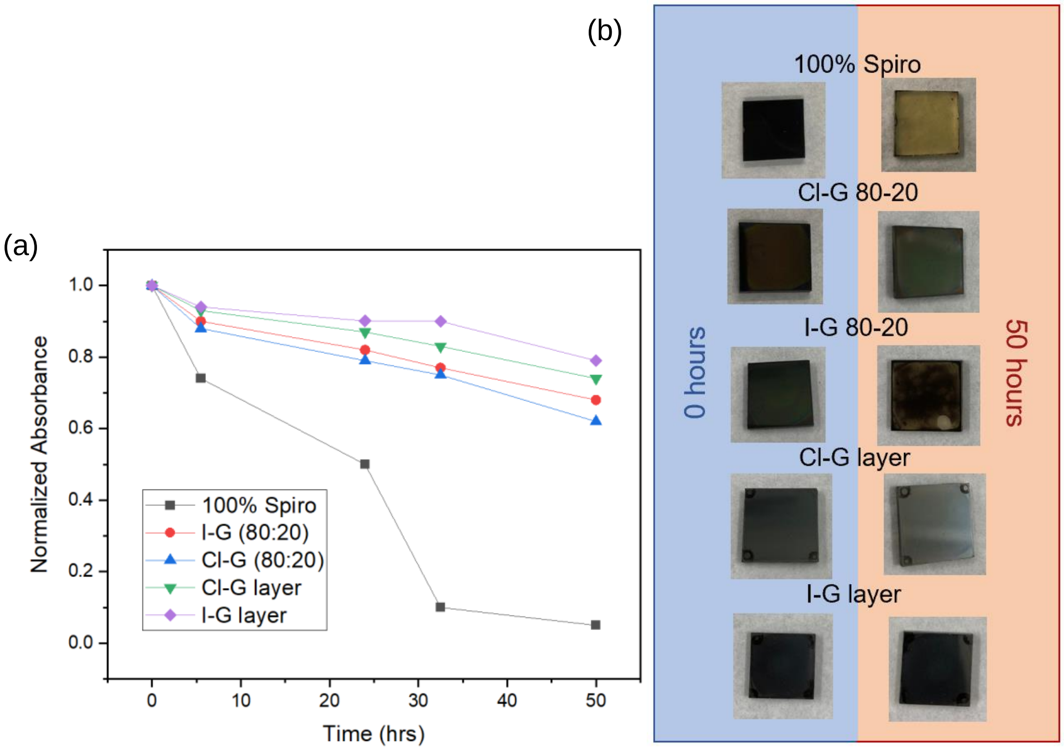

Figure 4.9 – (a) Degradation of the bare devices in a highly moist environment at 85% RH across a 50 hr testing span (absorbance at 550 nm), (b) Images of the samples before and after the 50 hr testing period.

Some previous works have provided studies discussing the edge doping of carbon-based materials with halogens (i.e. fluorine) to create hydrophobic particles and hence enhance the stability[150,151]. Generally, the incorporation of halogen graphene particles in the PSC resulted in enhanced stability in both ambient and highly humid environments. This is attributable to several factors including that the hydrophobic additives in the spiro-OMeTAD or the encapsulating layer can act as a protection layer against the moisture and oxygen preventing their inevitable ingress into the perovskite film and the highly soluble lithium salt component in the top layer (HTL: spiro-OMeTAD). The Cl and I functional groups were reported to bond with the graphene at a bond angle in the graphene sheet that removes the polar moment making them non-polar[221,222]. The PSC is most susceptible to ingress of moisture and oxygen at the grain boundaries of the spiro-OMeTAD film where there are uncovered perovskite grains. However, as observed in the SEM and AFM images in Figure 4.5, the perovskite grain boundaries are partially covered by the Cl-G particles and the spiro-OMeTAD grain boundaries are almost fully covered by the Cl-G layer. The increased surface roughness, as indicated by the AFM images in Figure 4.5, could also play a role in increasing the surface hydrophobicity[223].

## 4.4 – Effect of chlorinated and iodinated graphene on perovskite solar cell efficiency

The power conversion efficiency of the PSCs was investigated to understand the effect of the fabricated halogenated graphene particles (Cl-G and I-G) and the different configurations (additives versus encapsulating layers).

The current density-voltage (J-V) curves for the highest-performing light-soaked PSC devices; 100% spiro-OMeTAD, Cl-G 80:20 additive, I-G 80:20 additive, Cl-G encapsulating layer, and I-G encapsulating layer are compared below in Figure 4.10 (a). The corresponding photovoltaic parameters and statistical data which were obtained for five devices is summarized below in Figure 4.10 (b) and Table 4.2.

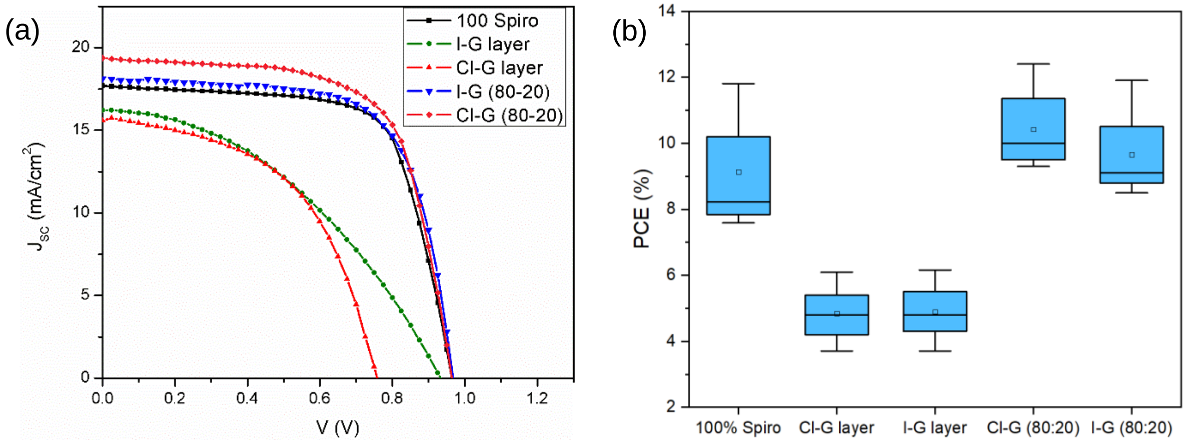

Figure 4.10 – (a) Current density-voltage (J-V) curves and, (b) statistical data for the PSCs with different HTL configurations compared to the control sample (100% spiro-OMeTAD).

Table 4.2 – Photovoltaic parameters of the PSCs using different HTL configurations.

| | **PCE %** | **Jsc (mA/cm$^2$)** | **Voc (V)** | **FF (%)** |
|---|---|---|---|---|
| 100% spiro | 11.81 | 17.7 | 0.96 | 69 |
| Cl-G layer | 6.09 | 15.5 | 0.77 | 48 |
| I-G layer | 6.16 | 16.2 | 0.93 | 40 |
| Cl-G (80-20) | 12.40 | 19.3 | 0.96 | 65 |
| I-G (80-20) | 11.91 | 18.1 | 0.96 | 67 |

Figure 4.10 (b) showed that the devices illustrated consistent performance trends. The control sample with 100% spiro-OMeTAD displayed a PCE of 11.81%, Jsc of 17.7 mA/cm$^2$, Voc =0.96 V, and FF of 69%. Encouragingly, the incorporation of the halogen-doped graphene additives (80:20 spiro-Cl/I-G) showed a positive effect on the short circuit current , which increased to 19.3 mA/cm$^2$ and 18.1 mA/cm$^2$, that consequently resulted in an increase in the PCE of the champion devices to 12.4% and 11.91% for the Cl-G and I-G based devices respectively. The increase of the device performance can be attributed to numerous factors. Firstly, graphene based materials have illustrated their capability for efficient charge extraction and transfer from the perovskite material, owing to their high charge carrier mobility[126,149]. Therefore, the Cl-G/I-G particles in the HTL that are in direct contact with the perovskite film can provide efficient charge extraction sites. It is also likely that the chlorine component in contact with the perovskite can dramatically enhance the charge transport as per previous reports[224]. It has also been illustrated that dominant hole transfer can occur between graphene and iodine atoms at the perovskite interface[225].

Figure 4.11 shows the steady state PL spectra measured on device stacks without metal electrodes (excitation was from the top of the spiro-OMeTAD layer) for the two additive based devices compared to the control device (100% spiro-OMeTAD). Crucially, the PL for the Cl-G additive-based device showed more than 86% PL quenching compared to the I-G additive device showing 57% PL quenching. This indicates that the holes generated in the perovskite film are more efficiently extracted by the Cl-G additive HTL structure[226] (followed by the I-G additive HTL) than the bare spiro-OMeTAD. That results in enhanced Jsc and in turns improved the PCE.

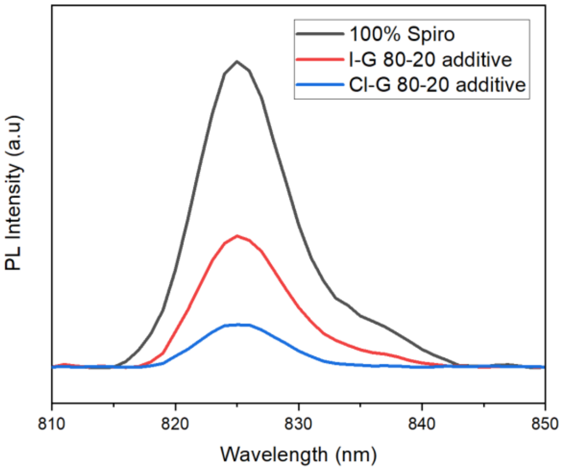

Figure 4.11 – PL spectra for control device with 100% spiro-OMeTAD HTL, I-G, and Cl-G additive-based devices. The excitation wavelength employed was 680 nm.

The improved hole extraction may follow, at least in part, from the superior hole mobility that is expected for graphene. The sp3 hybridized nitrogen atom in the spiro-OMeTAD results in an intrinsic triangular pyramid bond configuration and hence large intermolecular distances, resulting in a low hole mobility and inferior conductivity[227,228]. Therefore, with graphene's expected high conductivity and charge carrier mobility of $10^3$–$2 \times 10^5$ $cm^2\ V^{-1}\ s^{-1}$ compared to that of spiro-OMeTAD reported at $8.1 \times 10^{-5}$ $cm^2\ V^{-1}\ s^{-1}$, it can provide more efficient hole extraction[229]. The improved hole extraction observed for the Cl-G and I-G additive-based devices may also be due, in part, to laser-induced defects. The laser treated graphene particles are known to be rich with trap states (also the rough surface as observed by AFM can result in increased trap states), which can serve as additional energy levels to host holes. That in turn may alleviates the spiro-OMeTAD's poor charge mobility issue and accelerate the hole extraction process as was evident in the PL quenching. This could play an instrumental role in relieving any charge accumulation at the HTL/perovskite interface. Agresti et al has discussed the activation of trap and recombination centers and their positive role on PSC device performance[149].

Furthermore, an increased electron barrier height due to a possible increase in the bandgap of the laser treated graphene particles (due to quantum confinement) may also enhance electron blocking. Additionally, the polyiodides observed in Figure 4.3 (d) provide a tunneling channel for hopping in I-G through the iodine p-orbital interaction with the Carbon, giving rise to superior charge transfer process[89].

The PSCs with Cl-G and I-G encapsulation layers, however, both displayed lower PCEs of 6.09% and 6.16% respectively. An important observation noted on their J-V curves, was the lower slope near the Voc, which indicates a higher series resistance. As a result, their fill factors were significantly reduced compared to the other devices and their short circuit current densities were slightly smaller. This indicates that the layers of the functionalized graphene particles inhibit hole charge transport into the Ag electrode. While adjustment of the graphene layer thickness can possibly alleviate this series resistance issue in the future, it suggests that the energy levels of the Cl-G and I-G are well-suited to facilitate hole transfer from the perovskite to the spiro-OMeTAD and/or Ag electrode but not ideal for transferring holes from the spiro-OMeTAD to the Ag.

The devices were kept in a humidity chamber at 85% RH without encapsulation, and the degradation of the PCE of the devices was tracked across a 10-hr testing span as shown below in Figure 4.12.

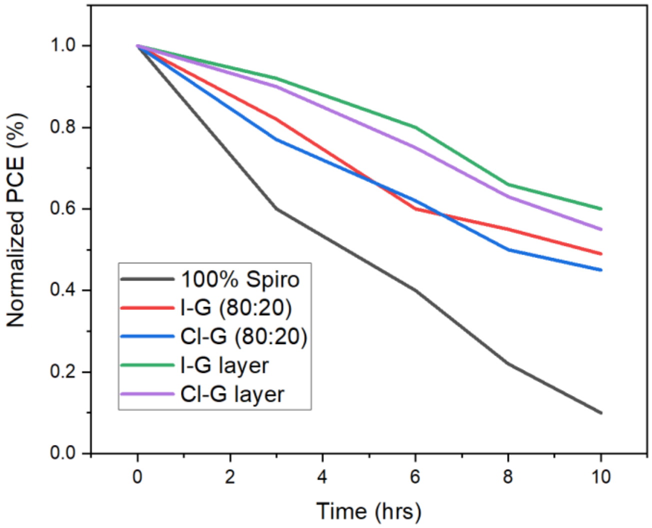

Figure 4.12 – Degradation of the PCE of PSC devices with different HTL configurations across a 10 hr testing span in 85%RH.

The Cl-G and I-G layered devices show again the better stability as they retain 0.55 and 0.6 of the initial PCE after the completion of the testing span. The additive based devices also show improved stability retaining 0.45 and 0.49 of their initial PCE for the Cl-G and I-G additive-based samples. It is important to note that these samples degrade much faster than the stability tests presented in Figures 4.8 and 4.9 due to the fact that these samples are exposed to several degradation routes; 85% relative humidity, metal electrode migration, and light decomposition, all contributing to an accelerated testing span.

Thus herein we engineered a HTL additive material that is found to have super hydrophobic properties as measured in contact angle measurements, that results in enhanced PSC device stability in both ambient and highly humid environments by repelling the penetrative water/oxygen molecules that can dissolve the Lead compound in the perovskite layer and the lithium salt in the spiro-OMeTAD. The additive is also found to extract holes more efficiently and may play a constructive role in electron blocking.

# 5.0 - Laser-directed assembly of nanorods of 2D materials

---

- 5.1 – Experiments and methodology
- 5.2 – Characterization
- 5.3 – Laser induced growth of 2D nanorods theory and morphology
- 5.4 – Physical properties of the nanorods
- 5.5 – Application of the nanorods as transparent conducting films

---

## 5.1 – Experiments and methodology

### *Solution preparation*

$MoS_2$, $WS_2$, and BN ultrafine powders (purchased from Graphene Supermarket) were dispersed in an ethanol:water (1:1 ratio) solvent (0.124 mg $mL^{-1}$). “Pristine graphene” (PG) in ethanol (1 mg $mL^{-1}$) was also purchased from Graphene Supermarket.

### *Laser treatment*

A Ti:sapphire laser with a regenerative amplifier, producing an operating wavelength of 800 nm, pulse duration of 35 fs, average power of 0.25 W, and a repetition rate of 1 kHz was used in all laser treatment processes. Each solution (3.5 mL) was treated for different time durations by the linearly polarized laser beam using a 5 cm focal length lens, creating a beam focus set at a 0.5 cm depth below the air/solution interface. During the treatment process the solutions were constantly stirred by a magnetic stirrer. To achieve a circular polarization, a quarter wave plate was inserted before the final 2 mirrors that steer the beam through the focusing lens. Each solution was treated by the laser beam with the circular polarization using the same procedure described above for 20 min (and 10 min for PG).

## 5.2 – Characterization

To ensure characterization was performed on the fabricated nanorods, filtration of aggregations was achieved by centrifuging (1.5 mL) the laser treated solution for 5 min at 3000 rpm and extracting the upper portion of the solution (0.5 mL). The Raman spectroscopy was carried out for each sample using a Renishaw micro-Raman spectrometer with an excitation wavelength of 632.8 nm and power of 20 mW. Raman analysis was carried out on thin films fabricated by drop casting the solution (250 μL) on silicon substrates that were dried at room temperature. The surface morphologies and microstructure of the drop-cast samples were studied by SEM using a

LEO 1530 with a Schottky-type field emission electron source. AFM measurements were performed using a Dimension 3100 Scanning Probe Microscope. XPS samples were measured on silicon substrates and the Si 2p transition was used for binding energy calibration. Spectral analysis was performed by deconvoluting Gaussian multipeak fits. The XRD patterns were also obtained by analyzing thin films fabricated by drop casting the solution (250 μL), and 2-theta scans were performed using an X'Pert Pro-Panalytical diffractometer system with the Kα1 wavelength of 1.542 Å at 45 kV and 35 mA. After drop casting $WS_2$ solutions (20 μL, bulk and laser treated) with the same concentrations in a similar circular area on glass substrates, their transparencies were assessed using a double monochromator UV-2501 PC spectrophotometer (Shimadzu) with a 0.1 nm resolution. For electrical characterization, simple field effect transistors were fabricated on silicon oxide substrates by depositing 10 nm chrome pads followed by 300 nm thick gold pads with a channel length of 60 μm. The solution (15 μL) was drop casted onto the channel to obtain percolation at 60 °C.

## 5.3 – Laser induced growth of 2D nanorods theory and morphology

Bulk rectangular and circular flakes of Pristine graphene (PG), $MoS_2$, $WS_2$, and BN were diluted in 4 mL vials. All solutions had a concentration of 0.124 mg $mL^{-1}$ in water-ethanol (1:1), with the exception of the PG, which had a concentration of 1 mg/mL in ethanol. These untreated bulk flakes are expected to provide the "seed" or precursor material for the nanorod formation. A scanning electron microscopy (SEM) image of the $WS_2$ flakes is shown in the inset in Figure 5.1 (a). As illustrated in Figure 5.1, the flake-containing solutions were treated using a linearly polarized femtosecond laser with a pulse energy of 0.25 mJ and 1 kHz frequency, which results in the formation of long nanorods, as shown in the inset SEM image in Figure 5.1 (d).

The high electric field in the laser focus, which is comparable in scale to the binding field of the valence electrons in a molecule or nanoparticle, will induce ionization and lead to fragmentation/Coulomb explosion[35,230]. This exfoliates and fragments the untreated flakes into smaller fragmented nanoparticles and molecules, as shown in Figure 4.10 (b). As previously reported for Cu and ZnO nanorod fabrication[231], nanoparticles that are fragmented by femtosecond laser treatment can act as nucleation sites for rod growth. It is therefore expected that the bulk, unexposed flakes act as the material source, from which the nanoparticles are created and reassemble to form the linear nanorod structures. Alignment of the nanoparticles and molecules is achieved through the interaction of the large induced dipole, with the AC electric field of the laser inside the laser focus. The ultrashort timescale of the aligning pulse (35 fs) relative to that of the rotational dynamics results in so called impulsive alignment[232], in which rotational wave packets are formed that realign periodically[233]. The crucial property of the nanoparticles when considering their tendency to align is their polarizabilities, which are measures of their dimensions. The axis with maximum polarizability will tend to align with the laser polarization direction. This can induce alignment when the fragmented nanoparticles come in contact with the beam focus due to the laser's linear polarization, as shown in Figure 5.1 (c)[234]. Alignment in the current experiment is distinctly different from most systems studied to date however, with the targets approaching the micrometer scale rather than the typical angstrom scale[235]. Additionally, the presence of a liquid will dampen the rotation and hence the nanorod formation, nevertheless, the drastically higher polarizability of the flakes in plane compared to out of plane will certainly mean that the laser pulses will exert a strong aligning influence, which yields nanorod formation, as shown for the $WS_2$ nanorods in Figure 5.1 (d).

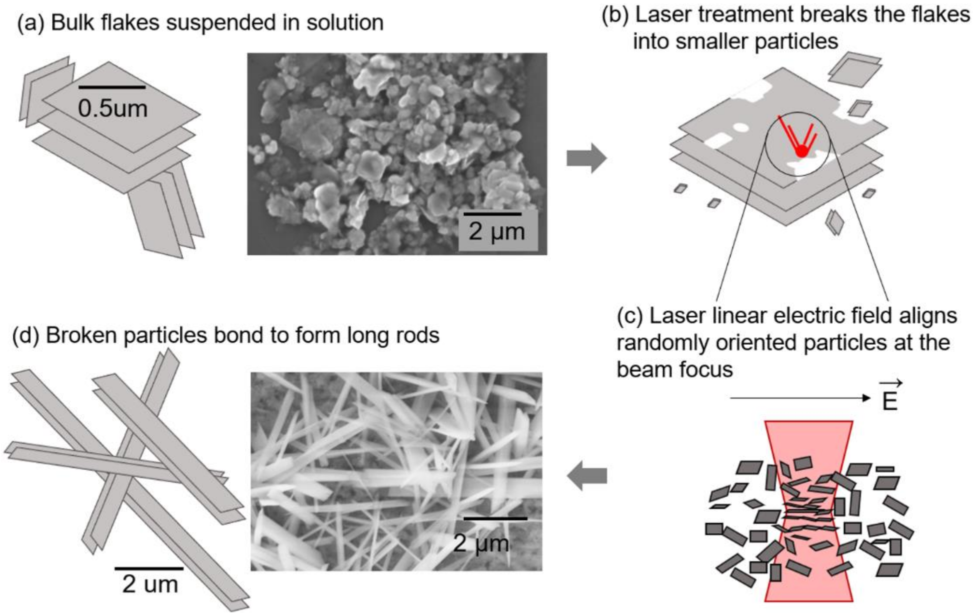

Figure 5.1 – Schematic illustrating the nanorod growth process via femtosecond laser treatment. (a) SEM image of $WS_2$ untreated bulk flakes. (b) Laser treatment fragmenting the bulk flakes into smaller nanoparticles. (c) Alignment of the fragmented nanoparticles inside the laser focus where the gray rectangles depict the particles, and d) nanorods formed by the reassembly of the fragmented nanoparticles. Reproduced with permission from Ibrahim et al. Laser-Directed Assembly of Nanorods of 2D Materials. Small 2019, 15, 1904415. Copyrights 2019 Wiley-VCH.

To investigate the influence of the laser polarization on the nanorod formation, the polarization of the laser was changed to circular, which can align molecules in the plane of the electric field but not with preferential orientation. In the presence of circular laser polarization, the nanorod formation and yield were adversely affected, indicating that an important part is played not only by alignment of the planes but by orientation of fragments with their major axis parallel to the linearly polarized field. SEM images of $WS_2$ flakes treated with circular and linear polarization are shown in Figure 5.2.

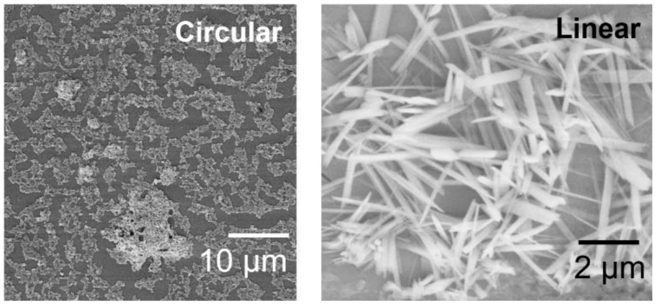

Figure 5.2 – Scanning electron microscopy (SEM) images of $WS_2$ samples after treatment using circular (left) versus linear (right) laser polarization for 20 minutes. Reproduced with permission from Ibrahim et al. Laser-Directed Assembly of Nanorods of 2D Materials. Small 2019, 15, 1904415. Copyrights 2019 Wiley-VCH.

Some of the formed nanorods were found to be hollow i.e., nanotubes. Figure 5.3 shows SEM images of $WS_2$ and BN samples after laser treatment for 20 min. A mixture of nanorods and nanotubes is observed (tube openings are highlighted with arrows). The nanotube formation is attributed to the introduction of dangling bonds by the laser treatment, causing a curving/rolling mechanism of the nanorod as reported previously[236].

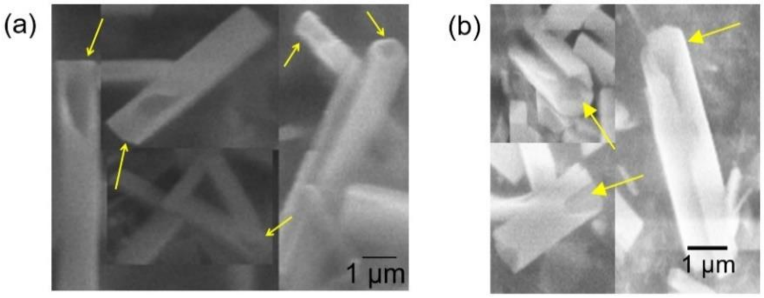

Figure 5.3 – Tubular features observed for (a) $WS_2$ and (b) BN samples after laser treatment for 20 min. Reproduced with permission from Ibrahim et al. Laser-Directed Assembly of Nanorods of 2D Materials. Small 2019, 15, 1904415. Copyrights 2019 Wiley-VCH.

Figure 5.4 shows SEM images of the BN, $WS_2$, PG, and $MoS_2$ before laser treatment (upper row) and after treatment for 20 min (lower two rows). The initial shape of the flakes was circular or rectangular. Following the laser treatment process, linear rods were formed that are longer than the original untreated bulk flakes. The longest nanorods, as observed using SEM, were achieved after 20 min of femtosecond laser treatment for BN, $WS_2$, and $MoS_2$, and after 30 min for PG. The BN, $WS_2$, PG, and $MoS_2$ rods grew to average lengths of 1.4 ± 0.6, 3.4 ± 1.0, 8 ± 3, and 6 ± 2 μm, respectively, after 20 min of laser treatment (30 min for PG). The corresponding aspect ratios were measured to be 6 ± 4, 9 ± 5, 10 ± 5, and 4 ± 2, respectively.

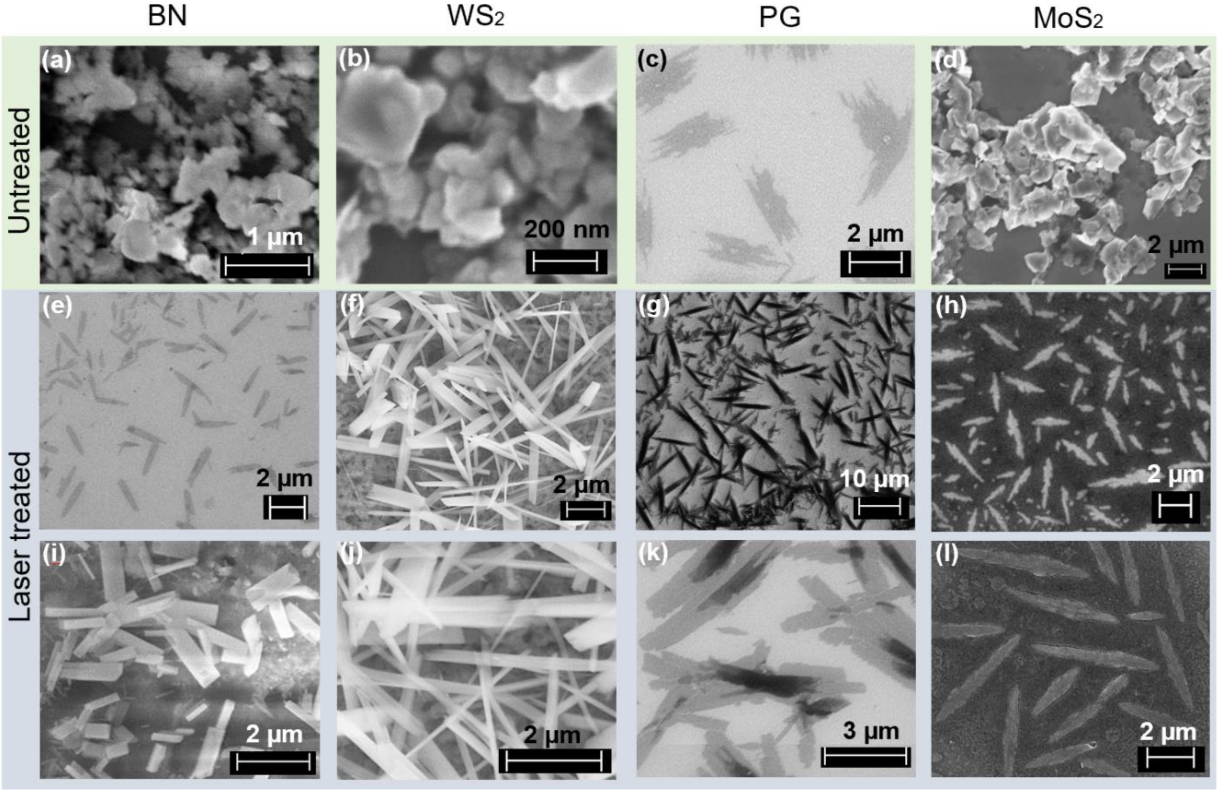

Figure 5.4 – (a–d) SEM images of untreated bulk 2D flakes and low magnification (e–h) and high magnification (i–l) SEM images nanorods formed after 20 min of laser treatment. Reproduced with permission from Ibrahim et al. Laser-Directed Assembly of Nanorods of 2D Materials. Small 2019, 15, 1904415. Copyrights 2019 Wiley-VCH.

The nanorods appear to be multilayered in the SEM images, which were confirmed by atomic force microscopy (AFM) in Figure 5.5. The AFM images indicated rod thicknesses of ≈20 nm, and steps were visible, indicating some variation in thickness along the nanorods.

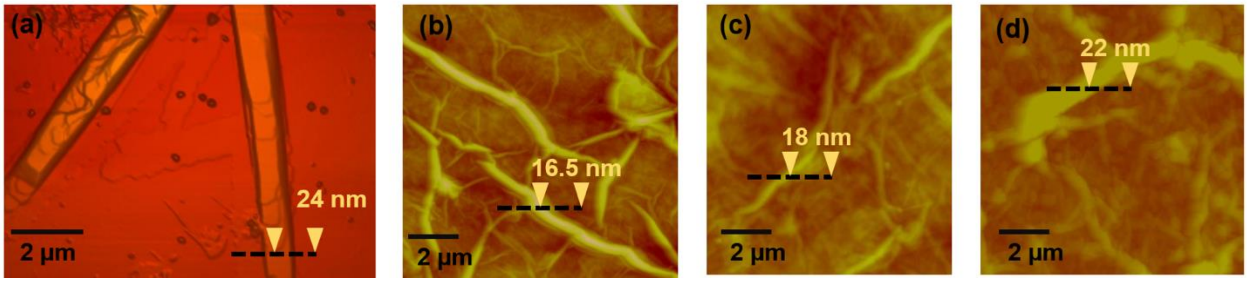

Figure 5.5 – Atomic force microscopy (AFM) images for (a) PG, (b) $WS_2$, (c) BN, and (d) $MoS_2$ nanorods. Reproduced with permission from Ibrahim et al. Laser-Directed Assembly of Nanorods of 2D Materials. Small 2019, 15, 1904415. Copyrights 2019 Wiley-VCH.

The PG, $MoS_2$, $WS_2$, and BN flakes were treated for different durations and the resulting nanorod lengths were estimated by SEM. Figure 5.6 illustrates the nanoparticle growth dependence on the duration of the femtosecond laser treatment. As noted previously, the length of the particles reached a maximum value after 20–30 min. As the laser treatment time was increased further, the average particle length decreased significantly until it eventually returned to the nanoscale with an aspect ratio of ≈1, consistent with the study presented in Chapter 3.0, where longer treatment times were used to fabricate quantum dots[35]. As mentioned above, the untreated bulk flakes provide the seed material for nanorod formation, where the fragmented nanoparticles reassemble to form the nanorods. This is denoted in Figure 5.6 (a) as the growth phase. Once most of the bulk flakes are dissociated (i.e., converted into fragmented nanoparticles), there is little seed material for further nanorod growth and the nanorods absorb most of the laser energy and consequently are dissociated into quantum dots. This is indicated as the dissociation phase in Figure 5.6 (a).

The transition from nanorod growth to nanorod dissociation was confirmed by examining the average $MoS_2$ nanorod length (after 20 min of femtosecond laser treatment) of a solution with a higher concentration of flakes (0.5 mg $mL^{-1}$ compared to 0.124 mg $mL^{-1}$) and hence a larger source of material from which the nanorods can grow. As presented in Figure 5.6 (b), the solution with the higher concentration (0.5 mg $mL^{-1}$) produced 25% longer rods (8 ± 3 µm) compared to the solution with the original concentration of 0.124 mg $mL^{-1}$ (6 ± 2 µm). Also, the PG solution has a higher concentration of 1 mg $mL^{-1}$ than its counterparts (0.124 mg $mL^{-1}$) and it is observed in Figure 5.6 (a) that the PG nanorods grow to longer lengths over longer treatment times. This is consistent with there being more bulk material available in the PG solution to be converted to nanorods, resulting in a delayed transition from the growth to dissociation phase.

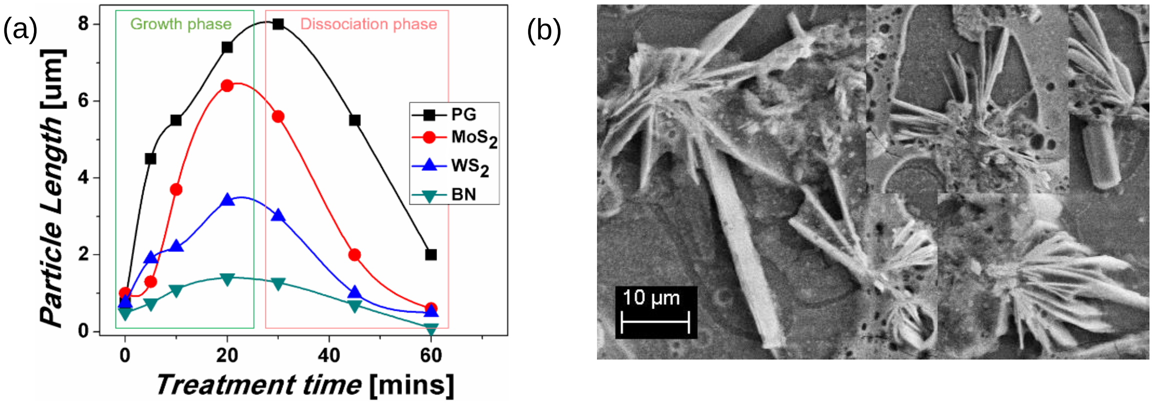

Figure 5.6 – (a) The average particle length versus the duration of the femtosecond laser treatment of the PG, $MoS_2$, $WS_2$, and BN solutions. (b) $MoS_2$ nanorods that self-assembled during laser treatment (20 mins) of a precursor solution with a concentration of 0.5 mg/mL. Longer nanorods are observed (8 ±3 μm) compared to solutions with a lower concentration of 0.124 mg/mL. Reproduced with permission from Ibrahim et al. Laser-Directed Assembly of Nanorods of 2D Materials. Small 2019, 15, 1904415. Copyrights 2019 Wiley-VCH.

## 5.4 – Physical properties of the nanorods

The structural properties of the nanorods were characterized using Raman spectroscopy, as shown in Figure 5.7. Peaks in the Raman spectrum of the untreated $WS_2$ sample in Figure 5.7 (a) can be assigned to the in-plane E 2G mode at ≈352 $cm^{-1}$ and to the out-of-plane A 1G mode at ≈417 $cm^{-1}$ of crystalline $WS_2$. Consistent with a previous report by Wang et al.[237] on $WS_2$ nanotubes, after laser treatment, the E 2G peak was observed at 351 $cm^{-1}$, a softening of the band that is attributable to the increase in lateral size. In contrast, a stiffening of the A 1G mode was observed (peak shifted to 418.5 $cm^{-1}$), consistent with previous reports[238,239] and indicative of increased thickness, which may be due to the agglomeration of the rods and their attachment through weak van der Waal forces when drop cast for analysis. The A 1G phonon peak involves sulfuric out-of-plane vibration and hence increasing the number of layers limits the movement in that direction. The intensity ratio (IA 1G/IE 2G) increases from 1.1 to 1.2 for the nanorods, which can also be attributed to increased thickness due to agglomeration[238]. Furthermore, D+G peaks at ≈1350 and ≈1590 $cm^{-1}$ were observed for the $WS_2$ nanorods, owing to graphitic domains formed by carbon atoms from the ethanol molecules (solvent) attaching to the nanorods, as reported previously[35].

The Raman spectrum of untreated $MoS_2$ in Figure 5.7 (b) shows peaks at 377 and 406 $cm^{-1}$ attributed to E 2G and A 1G vibrational modes. The $MoS_2$ rods illustrate a softening of both peaks to 376 and 402.2 $cm^{-1}$, which is attributed to the increase in the in-plane length of the rods and a reduction in thickness the $MoS_2$ nanorods are not agglomerated like their $WS_2$ counterparts, as observed in Figure 5.4 (h,l). Tensile strains induced by the increased in-plane length have previously been shown to result in red-shifting of both vibrational modes[240]. The redshift of the A 1G mode may also be attributable to doping of the $MoS_2$, as previously reported[241]. This is in agreement with the D+G bands observed for the $MoS_2$ nanorods (inset of Figure 5.7 (b)) that indicate the introduction of carbon and oxygen atoms from the solvent molecules. Previous reports of CVD fabricated $MoS_2$ have reported a full-width half maximum (FWHM) of 3.85 for the E 2G peak[242], which matches the FWHM of 3.80 obtained for the $MoS_2$ nanorods, reinforcing the hypothesis that the fragmented $MoS_2$ nanoparticles reassemble due to the linear electric field to form highly crystalline $MoS_2$.

Raman spectra for untreated bulk flakes and nanorods of BN and PG are provided in Figure 5.7 (c)(d). The characteristic Raman peak owing to hexagonal BN bonds disappears for the nanorods, indicating a change in crystal structure after laser reassembly, consistent with the altered optical absorption shown in Figure 5.8. The Raman spectra for PG, showed a slight increase in the amplitude of the D peak in the nanorod sample, which is attributed to the incorporation of oxygen and hydroxyl groups from the solvent[243].

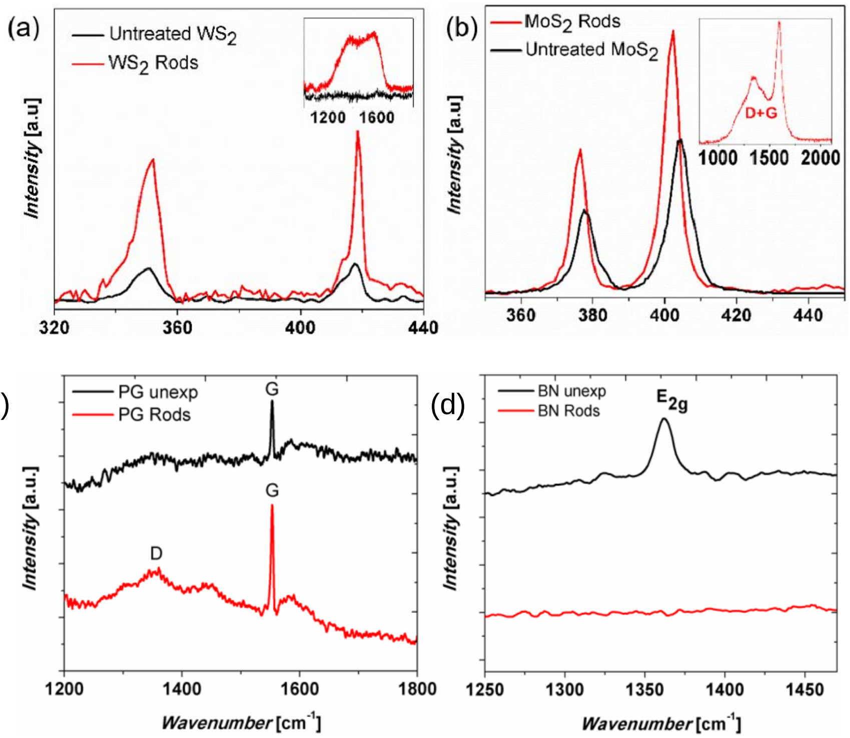

Figure 5.7 – Raman spectra for untreated flakes and nanorods of (a) $WS_2$, (b) $MoS_2$, (c) PG, and (d) BN. Reproduced with permission from Ibrahim et al. Laser-Directed Assembly of Nanorods of 2D Materials. Small 2019, 15, 1904415. Copyrights 2019 Wiley-VCH.

Carbon attachment is also optically evident in BN nanorods, as observed in Figure 5.8. An absorption measurement of the unexposed BN solution presents a characteristic hexagonal BN peak at 201 nm. After the femtosecond laser treatment, the h-BN absorption peak completely disappears and a new broad peak appears at ≈330 nm, which is attributable to the formation of carbon-doped BN[244].

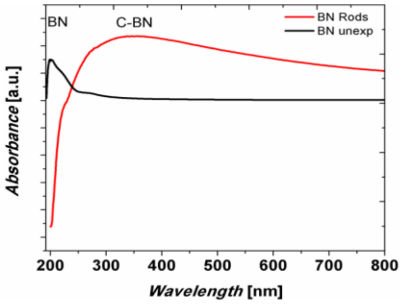

Figure 5.8 – Absorbance spectra of BN for nanorods (formed by 20 mins of laser treatment) and untreated samples. The broad peak observed for the nanorods is attributed to the attachment of carbon functional groups. Reproduced with permission from Ibrahim et al. Laser-Directed Assembly of Nanorods of 2D Materials. Small 2019, 15, 1904415. Copyrights 2019 Wiley-VCH.

The chemical composition of the BN and PG nanorods formed using 20 min of laser treatment was obtained via X-ray photoelectron spectroscopy (XPS) and is provided in Figures 5.9 and 5.10, with atomic percentages indicating that the nanorods are predominantly BN and PG, with some functional groups from the solvent incorporated.

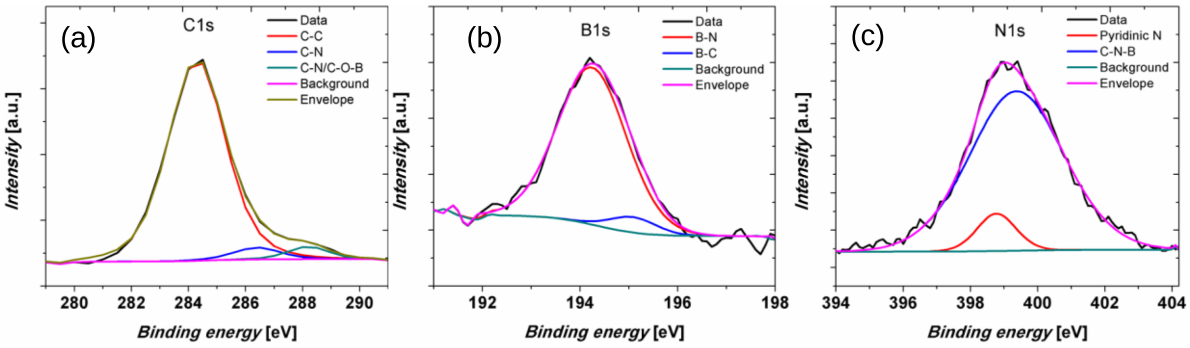

| C1s | | | B1s | | | N1s | | |
|---|---|---|---|---|---|---|---|---|
| **Name** | **Position [eV]** | **Conc.[%At]** | **Name** | **Position [eV]** | **Conc.[%At]** | **Name** | **Position [eV]** | **Conc.[%At]** |
| C-C [1] | 284.2 | 91.4 | B-N [2] | 194.2 | 93.8 | Pyridinic N [3] | 398.77 | 8.83 |
| C-N[3] | 286.4 | 4.5 | B-C [4] | 195.0 | 6.2 | C-N-B[4] | 399.37 | 91.17 |
| C-N/ C-O-B[3] | 288.19 | 4.1 | | | | | | |

Figure 5.9 – XPS for BN nanorods formed after 20 min of laser treatment. (a) C1s, (b) B1s, and (c) N1s energy levels indicating attachment of carbon and oxygen functional groups to the nanorods. Reproduced with permission from Ibrahim et al. Laser-Directed Assembly of Nanorods of 2D Materials. Small 2019, 15, 1904415. Copyrights 2019 Wiley-VCH.

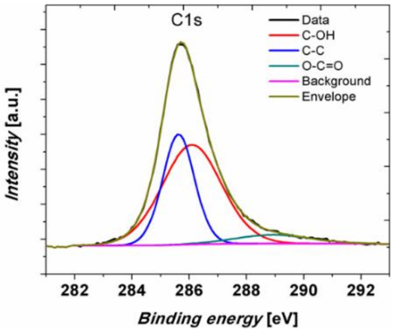

| Name | Position [eV] | Conc. [%At] |
|---|---|---|
| | | |
| C-OH[5] | 286.19 | 45.4 |
| C-C [5] | 285.71 | 49.1 |
| O-C=O[6] | 289.31 | 5.5 |

Figure 5.10 – XPS data for PG nanorods formed after 20 min of laser treatment, at C1s energy level. Reproduced with permission from Ibrahim et al. Laser-Directed Assembly of Nanorods of 2D Materials. Small 2019, 15, 1904415. Copyrights 2019 Wiley-VCH.

The XRD data for the nanorods (formed using 20 min of laser treatment) and untreated bulk flakes of $WS_2$ and $MoS_2$ are presented in Figure 5.11 (a) and (b) respectively. The untreated $WS_2$ sample shows characteristic 2H phase peaks corresponding to (002), (004), (100), and (101) planes, and a peak at 16° corresponding to the (004) plane in the 1T phase[245,246]. However, after the laser treatment, the peaks owing to reflections from the (100) and (101) planes disappear for the $WS_2$ nanorods, which is indicative of exfoliation of the bulk flakes[247]. Moreover, the peak corresponding to the (002) plane in the 2H phase disappears and the formation of a broad peak corresponding to the (002) plane in the 1T phase is observed[245], along with an increased peak intensity for the (004) plane in the 1T phase. The 1T phase is a metallic phase, so an increase in the electrical conductivity of the formed $WS_2$ rods would be expected. The XRD data of the $WS_2$ rods illustrate a broadening for all characteristic peaks, indicating a smaller crystallite size compared to the bulk $WS_2$[248]. This broadening and the shift of the rods' peaks to lower angles compared to the bulk (e.g., 1T (004) peak in Figure 5.11 (a)) could be attributable to the fact that large bulk flakes are fragmented into nanoparticles which then reassemble. The reassembled nanorods may have smaller crystallite sizes. It may also be attributable to the introduction of foreign atoms (e.g., carbon and oxygen[249]) during the laser treatment, as was observed in the Raman spectra and XPS measurements.

As the bulk flakes exfoliate and break due to the laser treatment, the ethanol and water solvent dissociates into radical carbon and oxygen species too, meaning that carbon and oxygen can be incorporated into the formed rods, as observed previously for quantum dots formed by femtosecond laser treatment[35]. This is also confirmed by the emergence of two new XRD peaks in Figure 3.32 (a), namely a $WO_x$ peak at 25°, and a peak at 28°, which is attributed to reflection from (002) graphitic carbon planes[249]. Based on the appearance of the new 1T phase, it is evident that the fragmented nanoparticles aligned in the linearly polarized electric field, are not simply interacting via van der Waal forces, but instead the atoms have sufficient energy in the intense electric field to rearrange and form new primary bonds, resulting in new crystalline phases and the formation of new materials via the incorporation of species from the solvent (e.g., oxides and graphitic domains).

The XRD of $MoS_2$ before and after laser treatment revealed that the (002), (207), and (211) peaks of the 2H crystalline phase remained present in the $MoS_2$ rods after laser treatment (Figure 5.11 (a)). However, new peaks corresponding to the 3R phase also appeared, including (004), (101), and (002)[250]. The reassembly into the 3R phase, which is more closely packed and requires less energy to vibrate, is consistent with the observed Raman redshifting of the $A_{1g}$ phonon mode. The introduction of the new crystalline 3R phase emphasizes that reassembly is occurring due to alignment of the fragmented nanoparticles in the laser's linearly polarized electric field. Moreover, functionalization of the rods with oxygen was observed in the emergence of a $MoO_2$ peak in Figure 5.11 (b).

Similarly, XRD of the BN nanorods, which is provided in Figure 5.11 (c), revealed peaks owing to the carbon bonding[251,252]. Reliable XRD data could not be obtained for the drop-cast PG nanorod samples because the graphene layer is too thin to detect a signal, but as was previously noted, XPS analysis of the PG nanorods in Figure 3.34 clearly indicated the attachment of oxygen and hydroxyl groups to the nanorods.

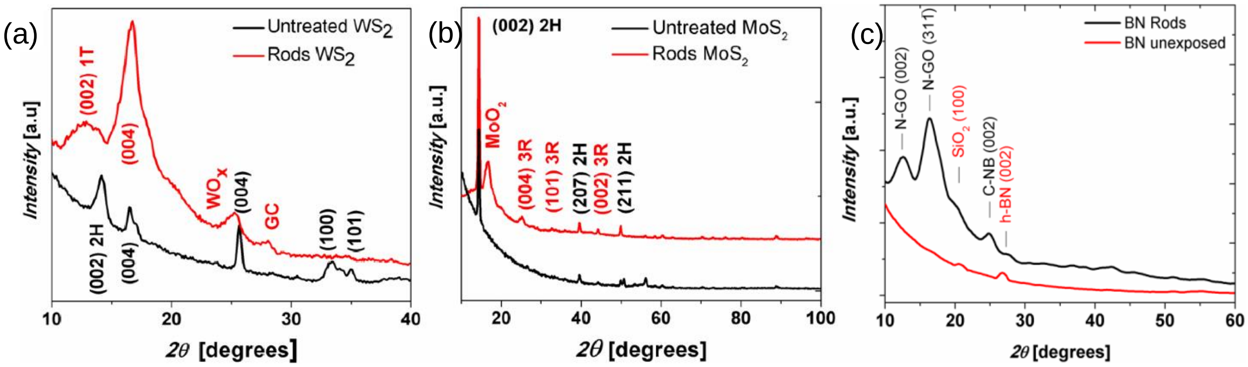

Figure 5.11 – XRD spectra for (a) $WS_2$, (b) $MoS_2$, and (c) BN. Reproduced with permission from Ibrahim et al. Laser-Directed Assembly of Nanorods of 2D Materials. Small 2019, 15, 1904415. Copyrights 2019 Wiley-VCH.

## 5.5 – Application of the nanorods as transparent conducting films

The reassembly of the $WS_2$ nanorods into the metallic 1T phase during laser treatment makes them particularly interesting for optoelectronic applications so their suitability as transparent conductors was assessed. Figure 5.12 (a) presents the transmittance spectra of thin films of the untreated bulk $WS_2$ flakes and the $WS_2$ nanorods (formed by 20 min of laser treatment) deposited on silica substrates. Both materials had similar concentrations and an identical volume of 15 μL was drop casted onto a 1 $cm^2$ area on the substrate to allow a direct comparison of the transmittance.

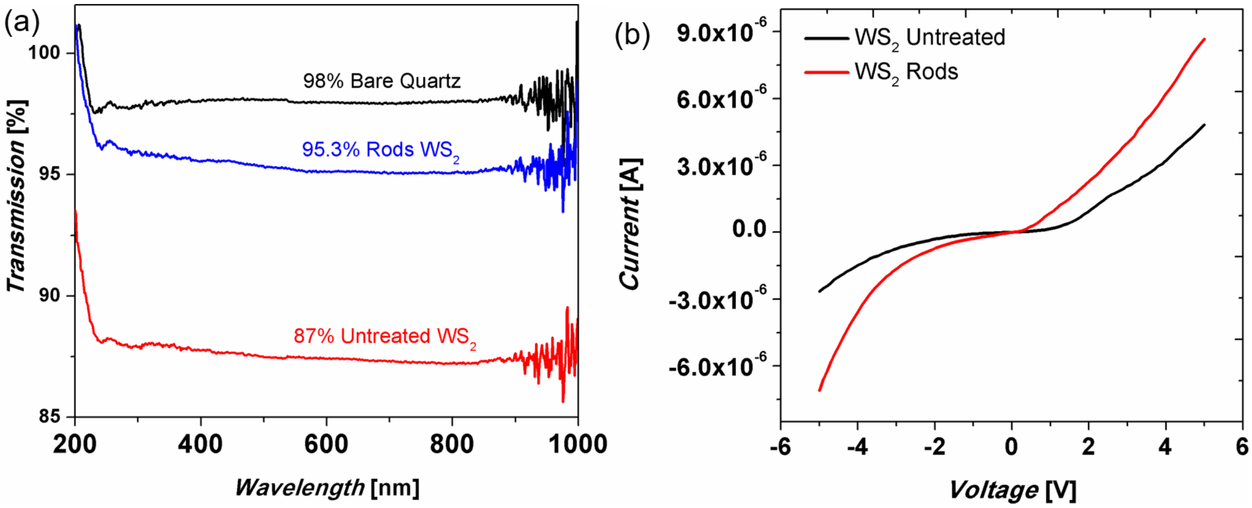

Figure 5.12 – (a) Transmission spectra of thin films of $WS_2$ untreated bulk flakes and nanorods, which were deposited on a quartz substrate. (b) Electrical conductivity measurement; I–V of the untreated $WS_2$ and the $WS_2$ nanorods deposited between gold electrodes (current is normalized by channel dimensions). Reproduced with permission from Ibrahim et al. Laser-Directed Assembly of Nanorods of 2D Materials. Small 2019, 15, 1904415. Copyrights 2019 Wiley-VCH.

The measurements revealed a higher transmittance for the nanorods at 95.3% compared to untreated bulk flakes at 87%. This result is consistent with previous work that found an increase in transmittance for increased Silver nanowire length[253]. Current voltage measurements were taken to compare the resistance of the films made from $WS_2$ nanorods and bulk untreated flakes. The samples were drop casted across a 60 μm channel length and Figure 5.12 (b) shows that the rods exhibited a higher conductivity, as expected, as the larger aspect ratio of the nanorods should result in a larger number of current percolation pathways[254]. The higher conductivity is also attributed, at least in part, to the significant increase in the amount of 1T (metallic) phase present in the nanorods, as observed by XRD. $WS_2$ in the 1T phase has a zigzag chain superlattice structure with a negligible energy gap at the fermi level, leading to a large carrier concentration and metallic nature[246].

While the transparency of the film produced from the $WS_2$ nanorods (95.3% at 550 nm) is significantly higher than that recently reported[255] for a 25.2 nm thick film of $WS_2$ (≈43% at 550 nm), the measured sheet resistance was an order of magnitude higher (800 Kohm $sq^{-1}$ compared to 84 Kohm $sq^{-1}$), which is likely due to a smaller volume of material present and the large number of interfaces between the rods[256], such that further optimization is warranted. The transparency and sheet resistance values of the $WS_2$ nanorod films fabricated in this work are also comparable to values previously reported for reduced graphene oxide[257]. Linear polarization of the incident laser, yielding rod lengths of up to ≈8 μm with only 20 min of laser treatment. Nanoparticles fragmented and broken from bulk flakes reassembled into nanorod structures via alignment in the linear electric field, however, the growth of the nanorods is limited by the availability of the bulk flakes. After depletion of the flakes, further laser treatment results in dissociation of the formed nanorods into quantum dots. It was therefore observed that solutions with higher concentrations of bulk flakes yielded longer rods.

Nanotubes were also observed in the $WS_2$ and BN samples owing to a rolling and curling mechanism. For some of the 2D materials, it was found that the particles reassembled, at least partially, into a new crystallographic phase. Notably, the XRD spectra indicated the formation of a new zig-zag chain super-lattice crystal structure for the $WS_2$ nanorods, which is metallic in nature. This is first report of laser-directed transformation of semiconducting 2D flakes into conductive metallic crystallographic phases. The nanorods were found to contain graphitic carbon domains, as identified by XRD and Raman analysis, due to the simultaneous treatment and incorporation of the solvent molecules.

Hence, this study unveils a new capability of the femtosecond laser; being the growth of 2D nanorods in aqueous solution. Notably, this is achieved in a 20 min period of time compared to the current state-of-the-art where several hours or often days are required to fabricate rods of similar materials. Comparison of thin films made from the untreated bulk flakes and nanorods of $WS_2$ indicated a significant reduction in the sheet resistance for the nanorods and an enhanced transparency, suggesting the potential to employ these nanorods in transparent conducting applications.

## 6.0 – Conclusions

In the study presented in Chapter 3.0, a simple, rapid, fs-laser treatment technique was introduced to produce hybrid 2D nanoparticles with novel optical properties. The results demonstrate that the technique is not restricted to a particular material. Flakes of $MoS_2$, $WS_2$, and BN were treated and in all cases the flakes were simultaneously reduced in size and functionalized. The nanoparticles had diameters of ≈3 nm, consisted of a few monolayers, and carbon domains (as well as some oxygen atoms) functionalized the 2D nanoparticles. Notably, these novel 2D hybrid nanoparticles were functionalized using ethanol as the carbon source, which is significantly cheaper and less hazardous than other materials used for functionalization. The hybrid nanoparticles exhibited absorption and photoluminescence owing to both the intrinsic 2D material and the carbon domains (an extra emission peak owing to oxygen was also found in the f-BN).

Importantly, the degree of functionalization (amount of carbon) could be tuned via the treatment time and solvent concentration, enabling precise control over the properties of the hybrid nanoparticles (e.g., the absorption edge). The ability to leverage the optical properties of both the intrinsic 2D material and the added carbon domains as well as tune their respective contributions is promising for a variety of applications, including biosensing and solar energy harvesting, among others. This is in addition to other advantages of functionalization such as improved solubility and biocompatibility. This approach can be applied to other starting materials and solvents in the future to synthesize a wide variety of novel hybrid nanoparticles for a broad range of applications.

Implementing this laser treatment process, graphene was laser treated to functionalize it with halogens namely, iodine and chlorine. The source of chlorination and iodination was the chlorobenzene solvent and sodium iodide additive, respectively. The hydrophobicity of both films was assessed by evaluating the contact angle of a water droplet in which super-hydrophobic angles were observed. These particles were then incorporated in the hole transport layers (top layer) of perovskite solar cells using two strategies. The particles were installed inside the HTL material (spiro-OMeTAD) in an additive capacity and as an encapsulating layer (top layer). Both ambient and high humidity degradation testing were conducted and both samples displayed improved stability. Degradation testing revealed an average retention of absorbance of all graphene-based devices of 80% across an impressive 2200 hr testing span for ambient conditions, while the highly humid conditions were monitored over a 50-hr span. This level of enhancement has not previously been realized by any 2D material incorporation in a PSC. The samples' PV parameters were also assessed and the insertion of the halogenated graphene particles in an additive capacity resulted in enhancement of the PCE from 11.8% to 12.4% that was attributable to the efficient role the graphene particles play in hole extraction. Therefore, the halogenated graphene particles were found to play a positive role in not only prolonging the stability of the PSC (an already major stumbling block towards commercialization) but also the PCE.

In chapter 5.0, a new technique to grow nanorods of two-dimensional materials using a femtosecond laser was introduced for the first time. The materials demonstrated in the manuscript include graphene, molybdenum disulfide, tungsten disulfide, and boron nitride. The nanorods are fabricated in as short as 20 minutes by utilizing the laser's ability to align nanoparticles in its electric field. Other methods studied in the literature are multistep and often require many hours and, in some cases, they require days. The field is sufficiently intense that new primary bonds can be formed to introduce new crystal structures in the nanorods, including metallic ones that enhance the conductivity and hence the usage of the rods in transparent conductors. This is the first report of laser-directed transformation of semiconducting 2D flakes into conductive metallic crystallographic phases. This approach can be leveraged in the future to study semiconductor-to-metal transitions in nanomaterials.  The technique is versatile and has proved its success on 4 materials and has the potential to be applied to many others in the future.

Leveraging all the above properties, films made from the fabricated $WS_2$ nanorods demonstrated an enhanced conductivity and transparency as discussed in section 5.5.

# 7.0 – Future and ongoing work

---

---

## Synopsis

The laser based experimental techniques presented in this research have shown their versatility in fabrication of nanoparticles that suit various applications and devices. In this section, a review of the work derived from the presented experimental techniques will be previewed. Additionally, some potential adjustments and improvements on the current research will be discussed. For the work accomplished in section 7.1.1, membrane sensors were provided by Prof Genki Yoshikawa and the application of the 2D sensing materials and preliminary testing of the sensors was conducted with PhD student Kissan Mistry. The membrane sensing materials were fabricated by me. Work discussed in section 7.1.2, including the sensing tests, was primarily conducted by masters student Ahmed Shahin, while the material characterization was conducted collaboratively.

## 7.1 – Leveraging laser treated functionalized 2D materials in future applications.

### 7.1.1 – Functionalized 2D nanoparticles for gas sensing

$MoS_2$, $WS_2$, and Graphene oxide sheets in both water and water-ethanol-50:50 solvents were laser treated to functionalize them with oxygen functional groups (from the solvent) and introduce defects that may act as active adsorption sites for analytes in gas sensing applications. While a low conductivity is expected to be induced by the defects and the oxygen functionalities via the laser treatment, which is problematic for resistive sensing, the poor conductance is rendered irrelevant in this case by employing a nanomechanical membrane stress sensor that detects a change in stress due to analyte adsorption onto the receptor layer. An image of the piezoresistive membrane sensor is shown in Figure 7.1 below.

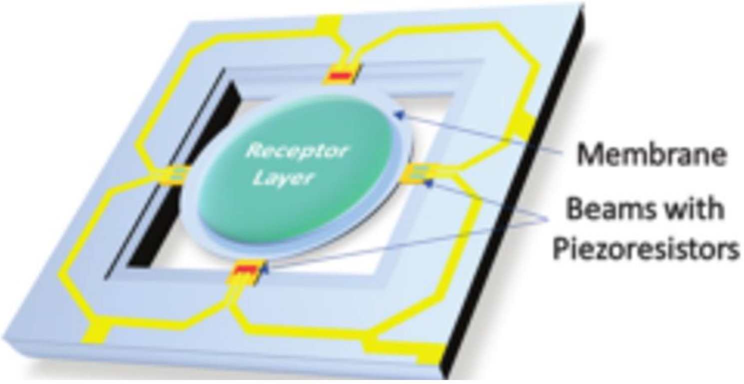

Figure 7.1 – Piezoresistive gas sensing membrane. Reproduced with permission from Osica, I. *et al.* Fabrication of Silica-Protein Hierarchical Nanoarchitecture with Gas-Phase Sensing Activity. *J. Nanosci. Nanotechnol.* **17**, 5908–5917 (2017).Copyrights 2017 American Scientific Publishers [258].

The fabricated 2D nanoparticles were deposited on the receptor layer via a micro plotting deposition technique. The relative gas sensing response for the laser treated 2D nanoparticles was found to be high, as seen in Figure 7.2 (a) (b). The fabricated $MoS_2$ particles were tested to sense a variety of volatile organic compounds and their relative response was shown to increase when the particles were laser treated in ethanol and water versus treatment in water only, as seen in Figure 7.2 (c).

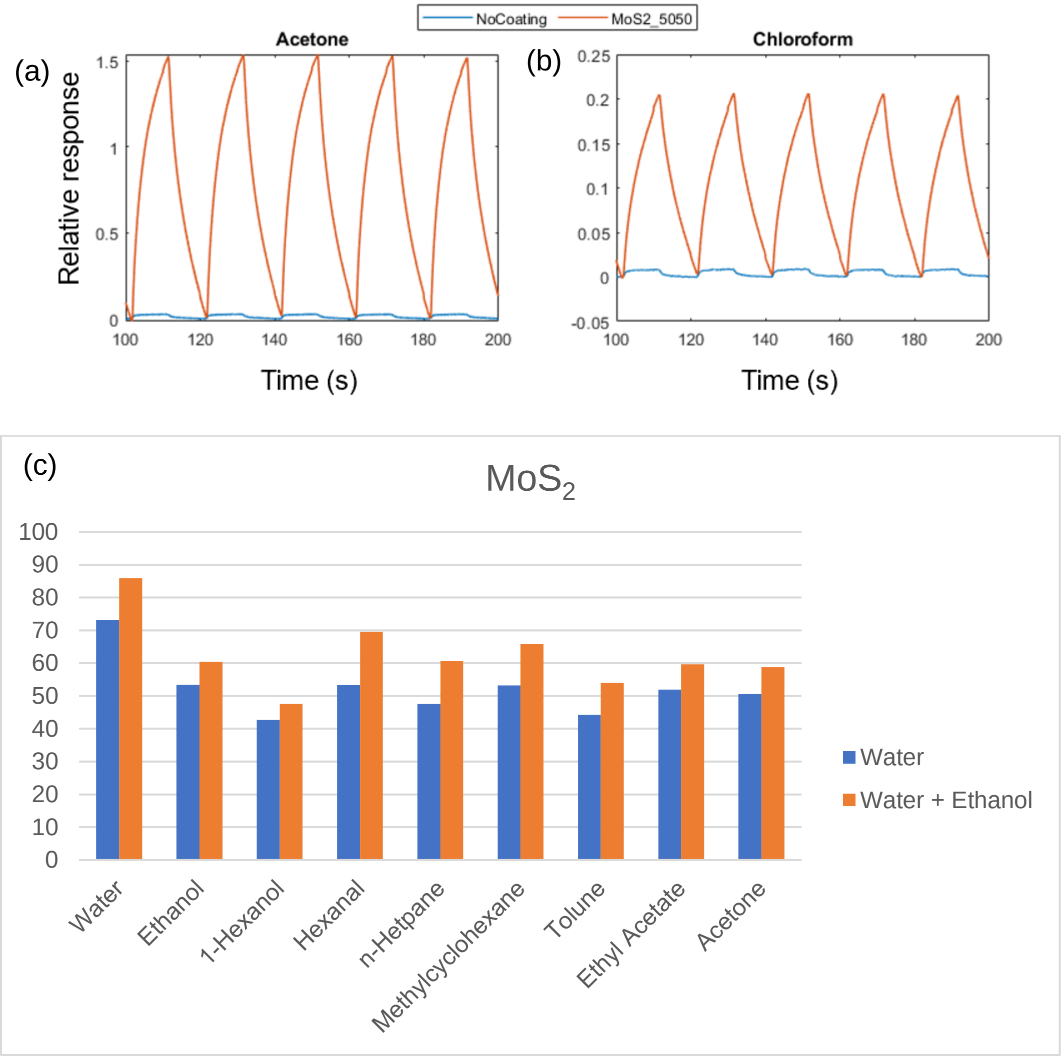

Figure 7.2 – Relative sensing response of $MoS_2$ particles laser treated in water-ethanol solvent, as compared to bare strain sensors, for (a) Acetone and (b) Chloroform. (c) Relative response to various organic compounds for $MoS_2$ laser treated in both ethanol-water and water.

It is hypothesized that the laser treatment and the functionalization of the TMD nanoparticles with apical or bridging sulfur bonds with high catalytic activity may dictate the relative response of the sensor, although studies are ongoing[259–261]. Therefore, this laser treatment process may be extremely useful for gas sensing applications, as different combinations of materials can be used to functionalize the particles. Additionally, the laser treatment process can be conducted in a suitable solvent that can maintain the particles' long-term stability. This work can be expanded in the future to examine different combinatorial materials that sense different analytes and serve different gas sensing settings such as industrial, breathalyser, and domestic applications. The prospect of using different materials can possibly play a role in enhancing the selectivity of these particles.

### 7.1.2 – Functional 2D nanoparticles used in chemical sensing

Micro pollutants are produced by humans through air emissions from coal-burning plants, smelters, waste incinerators, and process wastes from mining and industry. These pollutants have serious implications on human health, making it extremely important to sense them at the lowest concentrations. Using the same laser treatment process, different materials such as nitrogen-doped graphene oxide, black phosphorus, and $MoS_2$ were laser treated in acetonitrile and water-ethanol by MASc student Ahmed Shahin. Their ability to sense heavy metals in water such as Mercury, Lead, Cadmium, and Arsenic (typically found in very low concentrations in water) are currently being assessed.

For example, $MoS_2$ at 1 mg/mL was laser treated in acetonitrile for 70 mins and the resultant nanoparticles were used to sense Mercury. The sensing is achieved via PL quenching, as observed below in Figure 7.3. Defective nitrogen and sulfuric groups (induced by the laser treatment) are expected to play a significant role in binding with mercury or other heavy metal ions, which changes the electronic structure of the 2D materials[262]. This change induces a change in the emission spectrum of the nanoparticles.

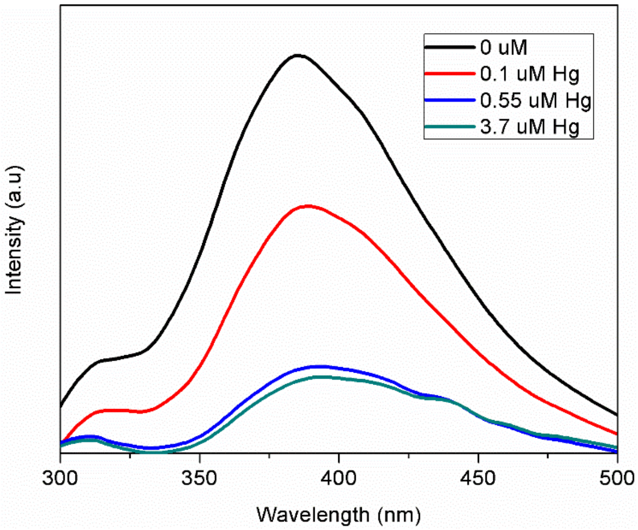

Figure 7.3 – PL spectra for $MoS_2$ nanoparticles as synthesized and after increased addition of Mercury, resulting in increased PL signal quenching.

XPS analysis revealed an increased incorporation of nitrogen and oxygen functional groups in the $MoS_2$. The limit of detection using this chemical sensor was found to be 0.02 nM, which is higher than most values found in literature, which is attributed to the high degree of functionalization via the laser treatment technique. Additionally, nitrogen-doped graphene oxide (NGO) laser treated in acetonitrile revealed a significant increase in pyloric and graphitic nitrogen functionalization (from XPS) that resulted in enhanced sensing of lead added at different concentrations, as observed in Figure 7.4.

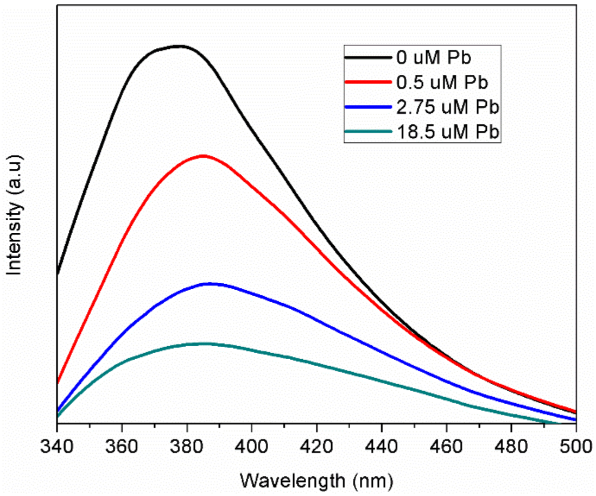

Figure 7.4 – PL spectra for as-synthesized NGO nanoparticles and after increased addition of Lead (Pb), resulting in increased PL signal quenching.

The charge transfer between the nanoparticles and the functional groups is expected to determine the selectivity of the sensors, which creates more options to tune the nanoparticles to act as chemical sensors for specific analytes with high sensitivity and selectivity.

## 7.2 – Potential for further enhancements of perovskite solar cell stability

PSC devices are generally very sensitive to fabrication conditions and layer ingredients. Therefore, minor changes are enough to induce significant changes to PV parameters and general cell performance. Thus, the precise conditions and recipe described in chapter 4.0 are open to numerous adjustments and development.

Primarily, the halogen-doped graphene spin coated as an encapsulating layer on top of the HTL may be further optimized. The graphene layer was spin coated at a spin coating speed of 2500 rpm, and it was concluded that the thickness of this layer was inhibiting hole transport to the metal electrode. Higher spin coating speeds such as 3500 rpm, 4500 rpm, and 5500 rpm to yield a thinner encapsulation layer can be implemented to increase hole transport.

As noted in the results chapter 4.0, the halogenated graphene layers have proven their efficiency in transferring holes from the perovskite to spiro-OMeTAD. A possible adjustment possible to the proposed recipe in chapter 4.0 is to spin coat the Cl-G or I-G encapsulation layer on top of the perovskite directly. The perovskite/spiro interface might be an ideal location for this layer. Alternatively, the size of the particles could be varied to tune the valence band position so that they can provide superior holes transfer when placed on top of the spiro-OMeTAD.

For the additive based samples, the graphene particles were premixed with the spiro-OMeTAD solution prior to spin coating with a ratio of 80:20 (spiro:graphene). Given the enhanced PCE performance observed for the additive based devices compared to the control devices, it is suggested to investigate the effect of varying the mixing ratio to 70:30 and 90:10 to understand the effect of increased addition of graphene particles.

The halogen doped graphene with chlorine and iodine resulted in the highest water contact angle indicating a great hydrophobic character. The combinatorial technique discussed in chapter 3.0 could potentially be employed to combine other materials that are thought to serve the long-term stability and device PV performance. For example, silica nanoparticles are notorious for their hydrophobicity due to their highly non-polar bonds. Silica-doped graphene particles could possibly be tested as an HTL additive, combining the positive roles played by both graphene in hole extraction and mobility and silica as a water repellent.

The graphene nanorods fabricated in chapter 5.0, could also potentially be a useful additive to the HTL if nanorods with suitable dimensions can be produced. They have high conductivity, transparency, and a geometry that could facilitate directional charge transport. The high transparency may avoid possible parasitic absorbance that occurs for the larger particles.

## 7.3 – Two dimensional nanorods; an outlook on method versatility and future applications

Two of the main outcomes of this work are the technique's ability to change the crystal structure of $WS_2$ from 2H semiconducting to the 1T metallic arrangement, and the process' versatility and ease. These outcomes could be leveraged in numerous studies.

For example, one dimensional semiconducting rod like structures have been reported previously for neuromorphic memristive applications[263,264]. A potential future project leveraging the produced nanorods is to be used as belts connecting metallic electrodes and to have their memristive performance assessed. Xiao et al. have reported the usage of ZnO nanowires for memristor applications, as shown below in Figure 7.5. However, they report that the surface states of semiconducting nanowires (dependent on wire morphology, geometry, and dangling bonds) influence the charge transport behaviour, possibly influencing the band bending between the semiconducting wire and the metal electrodes. Given the ability of the laser treatment process to control the nature of the crystal structure, the surface chemical functional groups, and the particle geometry, the laser based nanorod fabrication of 2D materials is an attractive prospect to test in these devices.

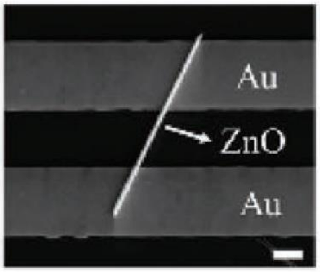

Figure 7.5 – SEM image of a ZnO nanowire device, scale bar is 2 µm. Reproduced with permission from Xiao, M. *et al.* Ultrathin TiOx Interface-Mediated ZnO-Nanowire Memristive Devices Emulating Synaptic Behaviors. *Adv. Electron. Mater.* **5**, 1900142 (2019). Copyrights 2019 Wiley-VCH[265].

The implementation of the 2D nanorods presented in Chapter 5.0 could also prove beneficial for flexible electronics, given the strong conductivity, transparency, and ease of fabrication of the nanorods.

Monolayer and few layer $MoS_2$ have exhibited high sensitivity toward a large number of chemical and biological species, pollutants, tactile pressure, and human body motions. Consequently,

$MoS_2$ films have been investigated for developing different types of flexible sensors[266]. The $MoS_2$ nanorods proposed could prove beneficial in biosensing applications given the ease of fabrication (being a single step method). The laser-based procedures have proven their success as illustrated in section 7.1 due to the laser's ability to create adsorption sites through defect engineering for a variety of analytes.

## Bibliography

1. Wolf, E. L. *Graphene: A New Paradigm in Condensed Matter and Device Physics*. (Oxford University Press, 2013).

2. Novoselov, K. S. *et al.* Electric Field Effect in Atomically Thin Carbon Films. *Science.* **306**, 666 – 669 (2004).

3. Geim, A. K. Graphene: Status and Prospects. *Science.* **324**, 1530 LP – 1534 (2009).

4. Geim, A. K. & Novoselov, K. S. The rise of graphene. *Nat. Mater.* **6**, 183–191 (2007).

5. Hollister, S. J. Porous scaffold design for tissue engineering. *Nat. Mater.* **4**, 518–524 (2005).

6. Holzinger, M., Le Goff, A. & Cosnier, S. Nanomaterials for biosensing applications: a review. *Frontiers in Chemistry.* **2**, 63 (2014).

7. Schwierz, F. Graphene transistors. *Nat. Nanotechnol.* **5**, 487–496 (2010).

8. Neto, A. C., Guinea, F. & Peres, N. M. Drawing conclusions from graphene. *Phys. World* **19**, 33-36, (2006).

9. Sutter, P. How silicon leaves the scene. *Nat. Mater.* **8**, 171–172 (2009).

10. Strudwick, A. J. *et al.* Chemical Vapor Deposition of High Quality Graphene Films from Carbon Dioxide Atmospheres. *ACS Nano* **9**, 31–42 (2015).

11. Rao, C. N. R., Matte, H. S. S. R. & Subrahmanyam, K. S. Synthesis and Selected Properties of Graphene and Graphene Mimics. *Acc. Chem. Res.* **46**, 149–159 (2013).

12. Kim, J. H. *et al.* Large-Scale Plasma Patterning of Transparent Graphene Electrode on Flexible Substrates. *Langmuir* **31**, 2914–2921 (2015).

13. Sur, U. K. Graphene: A Rising Star on the Horizon of Materials Science. *Int. J. Electrochem.* **2012**, 237689 (2012).

14. Soldano, C., Mahmood, A. & Dujardin, E. Production, properties and potential of graphene. *Carbon N. Y.* **48**, 2127–2150 (2010).

15. Castro Neto, A. H., Guinea, F., Peres, N. M. R., Novoselov, K. S. & Geim, A. K. The electronic properties of graphene. *Rev. Mod. Phys.* **81**, 109–162 (2009).

16. Mayorov, A. S. *et al.* Micrometer-Scale Ballistic Transport in Encapsulated Graphene at Room Temperature. *Nano Lett.* **11**, 2396–2399 (2011).

17. Falkovsky, L. A. Optical properties of graphene. *J. Phys. Conf. Ser.* **129**, 12004 (2008).

18. Yang, G., Li, L., Lee, W. B. & Ng, M. C. Structure of graphene and its disorders: a review. *Sci. Technol. Adv. Mater.* **19**, 613–648 (2018).

19. Li, X. L. *et al.* Layer-Number Dependent Optical Properties of 2D Materials and Their Application for Thickness Determination. *Adv. Funct. Mater.* **27**, 1604468, (2017).

20. Laturia, A., Van de Put, M. L. & Vandenberghe, W. G. Dielectric properties of hexagonal boron nitride and transition metal dichalcogenides: from monolayer to bulk. *npj 2D Mater. Appl.* **2**, 6 (2018).

21. Gao, Q., Zhao, X., Xiao, Y., Zhao, D. & Cao, M. A mild route to mesoporous Mo2C-C hybrid nanospheres for high performance lithium-ion batteries. *Nanoscale* **6**, 6151–6157 (2014).

22. Haldar, D., Dinda, D. & Saha, S. K. High selectivity in water soluble $MoS_2$ quantum dots for sensing nitro explosives. *J. Mater. Chem. C* **4**, 6321–6326 (2016).

23. Splendiani, A. *et al.* Emerging photoluminescence in monolayer $MoS_2$. *Nano Lett.* **10**, 1271–1275 (2010).

24. Zhang, Y., Tan, Y.-W., Stormer, H. L. & Kim, P. Experimental observation of the quantum Hall effect and Berry's phase in graphene. *Nature* **438**, 201–204 (2005).

25. Index. in *Woodhead Publishing Series in Electronic and Optical Materials* (eds. Lawrence, J. & Waugh, D. G. B. T.-L. S. E.) 677–694 (Woodhead Publishing, 2015). doi:https://doi.org/10.1016/B978-1-78242-074-3.09991-8

26. Wu, T., Liu, S., Li, H., Wang, L. & Sun, X. Production of reduced graphene oxide by UV irradiation. *J. Nanosci. Nanotechnol.* **11**, 10078–10081 (2011).

27. Liang, J. *et al.* Toward All-Carbon Electronics: Fabrication of Graphene-Based Flexible Electronic Circuits and Memory Cards Using Maskless Laser Direct Writing. *ACS Appl. Mater. Interfaces* **2**, 3310–3317 (2010).

28. Park, J. B., Yoo, J.-H. & Grigoropoulos, C. P. Multi-scale graphene patterns on arbitrary substrates via laser-assisted transfer-printing process. *Appl. Phys. Lett.* **101**, 43110

(2012).

29. Leon, J. A. *et al.* Rapid fabrication of bilayer graphene devices using direct laser writing photolithography. *J. Vac. Sci. Technol. B* **29**, 21204 (2011).

30. L., Kymakis, E., Petridis, C., Anthopoulos, T. D. & Stratakis, E. Laser-Assisted Reduction of Graphene Oxide. *IEEE*, **20**, 106-115 (2014).

31. Trusovas, R. *et al.* Reduction of graphite oxide to graphene with laser irradiation. *Carbon N. Y.* **52**, 574–582 (2013).

32. Kang, S. *et al.* Pulsed laser ablation based synthetic route for nitrogen-doped graphene quantum dots using graphite flakes. *Appl. Surf. Sci.* **506**, 144998 (2020).

33. Santiago, S. R. M. *et al.* Synthesis of N-doped graphene quantum dots by pulsed laser ablation with diethylenetriamine (DETA) and their photoluminescence. *Phys. Chem. Chem. Phys.* **19**, 22395–22400 (2017).

34. Sharma, P. & Vatsa, R. K. Chapter 16 - Nanoclusters Under Extreme Ionization Conditions. in (eds. Tyagi, A. K. & Banerjee, S. B. T.-M. U. E. C.) 575–613 (Elsevier, 2017). doi:https://doi.org/10.1016/B978-0-12-801300-7.00016-4

35. Ibrahim, K. H. *et al.* Simultaneous Fabrication and Functionalization of Nanoparticles of 2D Materials with Hybrid Optical Properties. **1701365**, 1–7 (2018).

36. Wang, Y. & Ni, Y. Molybdenum Disulfide Quantum Dots as a Photoluminescence Sensing Platform for 2,4,6-Trinitrophenol Detection. *Anal. Chem.* **86**, 7463–7470 (2014).

37. Jung, J. H. *et al.* Defect engineering route to boron nitride quantum dots and edge-hydroxylated functionalization for bio-imaging. *RSC Adv.* **6**, 73939–73946 (2016).

38. Li, Z. & Wong, S. L. Functionalization of 2D transition metal dichalcogenides for biomedical applications. *Mater. Sci. Eng. C* **70**, 1095–1106 (2017).

39. An, V. & Irtegov, Y. Tribological Properties of Nanolamellar $MoS_2$ Doped with Copper Nanoparticles. *J. Nanomater.* **2014**, 731073 (2014).

40. Jiang, Y. *et al.* Broadband and enhanced nonlinear optical response of $MoS_2$/graphene nanocomposites for ultrafast photonics applications. *Sci. Rep.* **5**, 16372 (2015).

41. Chen, X. & McDonald, A. R. Functionalization of Two-Dimensional Transition-Metal Dichalcogenides. *Adv. Mater.* **28**, 5738–5746 (2016).

42. Voiry, D. *et al.* Covalent functionalization of monolayered transition metal dichalcogenides by phase engineering. *Nat. Chem.* **7**, 45–49 (2015).

43. Paredes, J. I. *et al.* Impact of Covalent Functionalization on the Aqueous Processability, Catalytic Activity, and Biocompatibility of Chemically Exfoliated $MoS_2$ Nanosheets. *ACS Appl. Mater. Interfaces* **8**, 27974–27986 (2016).

44. Vishnoi, P., Sampath, A., Waghmare, U. V & Rao, C. N. R. Covalent Functionalization of Nanosheets of $MoS_2$ and $MoSe_2$ by Substituted Benzenes and Other Organic Molecules. *Chem. – A Eur. J.* **23**, 886–895 (2017).

45. Presolski, S. *et al.* Functional Nanosheet Synthons by Covalent Modification of Transition-Metal Dichalcogenides. *Chem. Mater.* **29**, 2066–2073 (2017).

46. Canton-Vitoria, R. *et al.* Integrating Water-Soluble Polythiophene with Transition-Metal Dichalcogenides for Managing Photoinduced Processes. *ACS Appl. Mater. Interfaces* **11**, 5947–5956 (2019).

47. Cho, K. *et al.* Electrical and Optical Characterization of $MoS_2$ with Sulfur Vacancy Passivation by Treatment with Alkanethiol Molecules. *ACS Nano* **9**, 8044–8053 (2015).

48. Satheeshkumar, E. *et al.* One-Step Simultaneous Exfoliation and Covalent Functionalization of $MoS_2$ by Amino Acid Induced Solution Processes. *ChemNanoMat* **3**, 172–177 (2017).

49. Garnett, E. C., Brongersma, M. L., Cui, Y. & McGehee, M. D. Nanowire Solar Cells. *Annu. Rev. Mater. Res.* **41**, 269–295 (2011).

50. Musselman, K. P. *et al.* Strong Efficiency Improvements in Ultra-low-Cost Inorganic Nanowire Solar Cells. *Adv. Mater.* **22**, E254–E258 (2010).

51. Könenkamp, R., Word, R. C. & Schlegel, C. Vertical nanowire light-emitting diode. *Appl. Phys. Lett.* **85**, 6004–6006 (2004).

52. Arafat, M. M., Dinan, B., Akbar, S. A. & Haseeb, A. S. M. A. Gas sensors based on one dimensional nanostructured metal-oxides: a review. *Sensors (Basel).* **12**, 7207–7258 (2012).

53. He, W. & Ye, C. Flexible Transparent Conductive Films on the Basis of Ag Nanowires: Design and Applications: A Review. *J. Mater. Sci. Technol.* **31**, 581–588 (2015).

54. Bellet, D. *et al.* Transparent Electrodes Based on Silver Nanowire Networks: From Physical Considerations towards Device Integration. *Materials* **10**, 570, (2017).

55. Song, Y., Fang, W., Brenes, R. & Kong, J. Challenges and opportunities for graphene as transparent conductors in optoelectronics. *Nano Today* **10**, 681–700 (2015).

56. Hecht, D. S., Hu, L. & Irvin, G. Emerging Transparent Electrodes Based on Thin Films of Carbon Nanotubes, Graphene, and Metallic Nanostructures. *Adv. Mater.* **23**, 1482–1513 (2011).

57. Wu, Z. *et al.* Transparent, Conductive Carbon Nanotube Films. *Science.* **305**, 1273 LP – 1276 (2004).

58. Zhang, D. *et al.* Transparent, Conductive, and Flexible Carbon Nanotube Films and Their Application in Organic Light-Emitting Diodes. *Nano Lett.* **6**, 1880–1886 (2006).

59. Duan, J. *et al.* Inorganic perovskite solar cells: an emerging member of the photovoltaic community. *J. Mater. Chem. A* **7**, 21036–21068 (2019).

60. Zhou, D., Zhou, T., Tian, Y., Zhu, X. & Tu, Y. Perovskite-Based Solar Cells: Materials, Methods, and Future Perspectives. *J. Nanomater.* **2018**, 8148072 (2018).

61. Suhaimi, S. *et al.* Critical analysis of stability and performance of organometal halide perovskite solar cells via various fabrication method (Review). *EPJ Web Conf.* **162**, (2017).

62. Snaith, H. J. *et al.* Anomalous Hysteresis in Perovskite Solar Cells. *J. Phys. Chem. Lett.* **5**, 1511–1515 (2014).

63. Liu, C. *et al.* Hysteretic Behavior upon Light Soaking in Perovskite Solar Cells Prepared via Modified Vapor-Assisted Solution Process. *ACS Appl. Mater. Interfaces* **7**, 9066–9071 (2015).

64. Zhao, C. *et al.* Perovskite Solar Cells: Revealing Underlying Processes Involved in Light Soaking Effects and Hysteresis Phenomena in Perovskite Solar Cells (Adv. Energy Mater. 14/2015). *Adv. Energy Mater.* **5**, (2015).

65. Yuan, Y. & Huang, J. Ion Migration in Organometal Trihalide Perovskite and Its Impact on Photovoltaic Efficiency and Stability. *Acc. Chem. Res.* **49**, 286–293 (2016).

66. Shao, Y. *et al.* Grain boundary dominated ion migration in polycrystalline organic–

inorganic halide perovskite films. *Energy Environ. Sci.* **9**, 1752–1759 (2016).

67. Levine, I. *et al.* Interface-Dependent Ion Migration/Accumulation Controls Hysteresis in MAPbI3 Solar Cells. *J. Phys. Chem. C* **120**, 16399–16411 (2016).

68. Law, C. *et al.* Performance and Stability of Lead Perovskite/TiO2, Polymer/PCBM, and Dye Sensitized Solar Cells at Light Intensities up to 70 Suns. *Adv. Mater.* **26**, 6268–6273 (2014).

69. Niu, G. *et al.* Study on the stability of CH3NH3PbI3 films and the effect of post-modification by aluminum oxide in all-solid-state hybrid solar cells. *J. Mater. Chem. A* **2**, 705–710 (2014).

70. Philippe, B. *et al.* Chemical and Electronic Structure Characterization of Lead Halide Perovskites and Stability Behavior under Different Exposures—A Photoelectron Spectroscopy Investigation. *Chem. Mater.* **27**, 1720–1731 (2015).

71. Rong, Y., Liu, L., Mei, A., Li, X. & Han, H. Beyond Efficiency: the Challenge of Stability in Mesoscopic Perovskite Solar Cells. *Adv. Energy Mater.* **5**, 1501066 (2015).

72. Yang, J., Siempelkamp, B. D., Liu, D. & Kelly, T. L. Investigation of CH3NH3PbI3 Degradation Rates and Mechanisms in Controlled Humidity Environments Using in Situ Techniques. *ACS Nano* **9**, 1955–1963 (2015).

73. Leguy, A. M. A. *et al.* Reversible Hydration of CH3NH3PbI3 in Films, Single Crystals, and Solar Cells. *Chem. Mater.* **27**, 3397–3407 (2015).

74. Frost, J. M. *et al.* Atomistic Origins of High-Performance in Hybrid Halide Perovskite Solar Cells. *Nano Lett.* **14**, 2584–2590 (2014).

75. Kawamura, Y., Mashiyama, H. & Hasebe, K. Structural Study on Cubic–Tetragonal Transition of CH3NH3PbI3. *J. Phys. Soc. Japan* **71**, 1694–1697 (2002).

76. Foley, B. J. *et al.* Temperature dependent energy levels of methylammonium lead iodide perovskite. *Appl. Phys. Lett.* **106**, 243904 (2015).

77. Misra, R. K. *et al.* Temperature- and Component-Dependent Degradation of Perovskite Photovoltaic Materials under Concentrated Sunlight. *J. Phys. Chem. Lett.* **6**, 326–330 (2015).

78. Han, Y. *et al.* Degradation observations of encapsulated planar CH3NH3PbI3 perovskite

solar cells at high temperatures and humidity. *J. Mater. Chem. A* **3**, 8139–8147 (2015).

79. Mubeen, S., Zhang, T., Yoo, B., Deshusses, M. A. & Myung, N. V. Palladium Nanoparticles Decorated Single-Walled Carbon Nanotube Hydrogen Sensor. *J. Phys. Chem. C* **111**, 6321–6327 (2007).

80. Sarkar, D. *et al.* Functionalization of transition metal dichalcogenides with metallic nanoparticles: Implications for doping and gas-sensing. *Nano Lett.* **15**, 2852–2862 (2015).

81. Hong, X. *et al.* Ultrafast charge transfer in atomically thin $MoS_2$/$WS_2$ heterostructures. *Nat. Nanotechnol.* **9**, 682 (2014).

82. Eda, G. *et al.* Photoluminescence from Chemically Exfoliated $MoS_2$. *Nano Lett.* **11**, 5111–5116 (2011).

83. Jiang, Y. *et al.* Broadband and enhanced nonlinear optical response of $MoS_2$/graphene nanocomposites for ultrafast photonics applications. *Sci. Rep.* **5**, 1–12 (2015).

84. Atkin, P. *et al.* 2D $WS_2$/carbon dot hybrids with enhanced photocatalytic activity. *J. Mater. Chem. A* **4**, 13563–13571 (2016).

85. Peimyoo, N. *et al.* Photocontrolled Molecular Structural Transition and Doping in Graphene. *ACS Nano* **6**, 8878–8886 (2012).

86. Ramasubramaniam, A. Large excitonic effects in monolayers of molybdenum and tungsten dichalcogenides. *Phys. Rev. B* **86**, 115409 (2012).

87. Solozhenko, V. L., Lazarenko, A. G., Petitet, J.-P. & Kanaev, A. V. Bandgap energy of graphite-like hexagonal boron nitride. *J. Phys. Chem. Solids* **62**, 1331–1334 (2001).

88. Tetsuka, H. *et al.* Optically Tunable Amino-Functionalized Graphene Quantum Dots. *Adv. Mater.* **24**, 5333–5338 (2012).

89. Zhang, X. & Lu, G. The spin-orbit coupling induced spin flip and its role in the enhancement of the photocatalytic hydrogen evolution over iodinated graphene oxide. *Carbon N. Y.* **108**, 215–224 (2016).

90. Šimek, P. *et al.* Towards graphene iodide: iodination of graphite oxide. *Nanoscale* **7**, 261–270 (2015).

91. Paredes, J. I. *et al.* Impact of Covalent Functionalization on the Aqueous Processability,

Catalytic Activity, and Biocompatibility of Chemically Exfoliated $MoS_2$ Nanosheets. *ACS Appl. Mater. Interfaces* **8**, 27974–27986 (2016).

92. Knirsch, K. C. *et al.* Basal-Plane Functionalization of Chemically Exfoliated Molybdenum Disulfide by Diazonium Salts. *ACS Nano* **9**, 6018–6030 (2015).

93. Manjunatha, S., Rajesh, S., Vishnoi, P. & Rao, C. N. R. Reaction with organic halides as a general method for the covalent functionalization of nanosheets of 2D chalcogenides and related materials. *J. Mater. Res.* **32**, 2984–2992 (2017).

94. Pramoda, K., Kaur, M., Gupta, U. & Rao, C. N. R. Nanocomposites of 2D-$MoS_2$ nanosheets with the metal–organic framework, ZIF-8. *Dalt. Trans.* **45**, 13810–13816 (2016).

95. Jeong, M., Kim, S. & Ju, S.-Y. Preparation and characterization of a covalent edge-functionalized lipoic acid–$MoS_2$ conjugate. *RSC Adv.* **6**, 36248–36255 (2016).

96. Liu, M. *et al.* Boron Nitride Quantum Dots with Solvent-Regulated Blue/Green Photoluminescence and Electrochemiluminescent Behavior for Versatile Applications. *Adv. Opt. Mater.* **5**, 1600661 (2017).

97. Lin, H. *et al.* Colloidal synthesis of $MoS_2$ quantum dots: size-dependent tunable photoluminescence and bioimaging. *New J. Chem.* **39**, 8492–8497 (2015).

98. Tang, X. *et al.* Fluorination-Enhanced Ambient Stability and Electronic Tolerance of Black Phosphorus Quantum Dots. *Adv. Sci.* **5**, 1800420 (2018).

99. Sun, Z. *et al.* TiL4-Coordinated Black Phosphorus Quantum Dots as an Efficient Contrast Agent for In Vivo Photoacoustic Imaging of Cancer. *Small* **13**, 1602896 (2017).

100. Alekseev, S. *et al.* Size and Surface Chemistry Tuning of Silicon Carbide Nanoparticles. *Langmuir* **33**, 13561–13571 (2017).

101. Shayeganfar, F., Rahimi Tabar, M. R., Simchi, A. & Beheshtian, J. Effects of functionalization and side defects on single-photon emission in boron nitride quantum dots. *Phys. Rev. B* **96**, 165307 (2017).

102. Scotognella, F., Kriegel, I. & Sassolini, S. Covalent functionalized black phosphorus quantum dots. *Opt. Mater. (Amst).* **75**, 521–524 (2018).

103. Xu, Y., Wang, X., Zhang, W. L., Lv, F. & Guo, S. Recent progress in two-dimensional

inorganic quantum dots. *Chem. Soc. Rev.* **47**, 586–625 (2018).

104. Zhou, J., Yang, Y. & Zhang, C. A low-temperature solid-phase method to synthesize highly fluorescent carbon nitride dots with tunable emission. *Chem. Commun.* **49**, 8605–8607 (2013).

105. Wu, Y. *et al.* High-frequency, scaled graphene transistors on diamond-like carbon. *Nature* **472**, 74–78 (2011).

106. Young, R. J., Kinloch, I. A., Gong, L. & Novoselov, K. S. The mechanics of graphene nanocomposites: A review. *Compos. Sci. Technol.* **72**, 1459–1476 (2012).

107. Bae, S.-H. *et al.* Graphene-based transparent strain sensor. *Carbon N. Y.* **51**, 236–242 (2013).

108. Yang, D., Yang, R., Priya, S. & Liu, S. (Frank). Recent Advances in Flexible Perovskite Solar Cells: Fabrication and Applications. *Angew. Chemie Int. Ed.* **58**, 4466–4483 (2019).

109. Zhang, H., Nazeeruddin, M. K. & Choy, W. C. H. Perovskite Photovoltaics: The Significant Role of Ligands in Film Formation, Passivation, and Stability. *Adv. Mater.* **31**, 1805702 (2019).

110. Wang, P. *et al.* Solution-Processable Perovskite Solar Cells toward Commercialization: Progress and Challenges. *Adv. Funct. Mater.* **29**, 1807661 (2019).

111. Hu, X., Li, F. & Song, Y. Wearable Power Source: A Newfangled Feasibility for Perovskite Photovoltaics. *ACS Energy Lett.* **4**, 1065–1072 (2019).

112. Bernardi, M., Palummo, M. & Grossman, J. C. Extraordinary Sunlight Absorption and One Nanometer Thick Photovoltaics Using Two-Dimensional Monolayer Materials. *Nano Lett.* **13**, 3664–3670 (2013).

113. You, P., Tang, G. & Yan, F. Two-dimensional materials in perovskite solar cells. *Mater. Today Energy* **11**, 128–158 (2019).

114. Singh, E., Kim, K. S., Yeom, G. Y. & Nalwa, H. S. Atomically thin-layered molybdenum disulfide ($MoS_2$) for bulk-heterojunction solar cells. *ACS Appl. Mater. Interfaces* **9**, 3223–3245 (2017).

115. Wen, X., Wu, J., Gao, D. & Lin, C. Interfacial engineering with amino-functionalized graphene for efficient perovskite solar cells. *J. Mater. Chem. A* **4**, 13482–13487 (2016).

116. Cao, J. *et al.* Efficient, Hysteresis-Free, and Stable Perovskite Solar Cells with ZnO as Electron-Transport Layer: Effect of Surface Passivation. *Adv. Mater.* **30**, 1–9 (2018).

117. Wang, B. *et al.* The charge carrier dynamics, efficiency and stability of two-dimensional material-based perovskite solar cells. *Chem. Soc. Rev.* **48**, 4854–4891 (2019).

118. Mei, A. *et al.* A hole-conductor–free, fully printable mesoscopic perovskite solar cell with high stability. *Science (80-. ).* **345**, 295 LP – 298 (2014).

119. Zhang, C. *et al.* Efficient stable graphene-based perovskite solar cells with high flexibility in device assembling: Via modular architecture design. *Energy Environ. Sci.* **12**, 3585–3594 (2019).

120. You, P., Liu, Z., Tai, Q., Liu, S. & Yan, F. Efficient Semitransparent Perovskite Solar Cells with Graphene Electrodes. *Adv. Mater.* **27**, 3632–3638 (2015).

121. Lee, D. Y., Na, S. I. & Kim, S. S. Graphene oxide/PEDOT:PSS composite hole transport layer for efficient and stable planar heterojunction perovskite solar cells. *Nanoscale* **8**, 1513–1522 (2016).

122. Intemann, J. J. *et al.* Highly efficient inverted organic solar cells through material and interfacial engineering of indacenodithieno[3,2-b]thiophene-based polymers and devices. *Adv. Funct. Mater.* **24**, 1465–1473 (2014).

123. Ray, R., Sarkar, A. S. & Pal, S. K. Improving performance and moisture stability of perovskite solar cells through interface engineering with polymer-2D $MoS_2$ nanohybrid. *Sol. Energy* **193**, 95–101 (2019).

124. Yeo, J. S. *et al.* Highly efficient and stable planar perovskite solar cells with reduced graphene oxide nanosheets as electrode interlayer. *Nano Energy* **12**, 96–104 (2015).

125. Yan, K. *et al.* High-Performance Graphene-Based Hole Conductor-Free Perovskite Solar Cells: Schottky Junction Enhanced Hole Extraction and Electron Blocking. *Small* **11**, 2269–2274 (2015).

126. Chandrasekhar, P. S. & Komarala, V. K. Graphene/ZnO nanocomposite as an electron transport layer for perovskite solar cells; The effect of graphene concentration on photovoltaic performance. *RSC Adv.* **7**, 28610–28615 (2017).

127. Wang, J. T.-W. *et al.* Low-Temperature Processed Electron Collection Layers of

Graphene/TiO2 Nanocomposites in Thin Film Perovskite Solar Cells. *Nano Lett.* **14**, 724–730 (2014).

128. Wu, Z. *et al.* Efficient planar heterojunction perovskite solar cells employing graphene oxide as hole conductor. *Nanoscale* **6**, 10505–10510 (2014).

129. Han, G. S. *et al.* Reduced Graphene Oxide/Mesoporous TiO2 Nanocomposite Based Perovskite Solar Cells. *ACS Appl. Mater. Interfaces* **7**, 23521–23526 (2015).

130. Umeyama, T. *et al.* Boosting of the Performance of Perovskite Solar Cells through Systematic Introduction of Reduced Graphene Oxide in TiO2 Layers. *Chem. Lett.* **44**, 1410–1412 (2015).

131. Sung, H. *et al.* Transparent Conductive Oxide-Free Graphene-Based Perovskite Solar Cells with over 17% Efficiency. *Adv. Energy Mater.* **6**, 1501873 (2016).

132. Luo, Q. *et al.* Iodide-reduced graphene oxide with dopant-free spiro-OMeTAD for ambient stable and high-efficiency perovskite solar cells. *J. Mater. Chem. A* **3**, 15996–16004 (2015).

133. Huang, P. *et al.* Water-Soluble 2D Transition Metal Dichalcogenides as the Hole-Transport Layer for Highly Efficient and Stable p–i–n Perovskite Solar Cells. *ACS Appl. Mater. Interfaces* **9**, 25323–25331 (2017).

134. Selvakumar, D., Murugadoss, G., Alsalme, A., Alkathiri, A. M. & Jayavel, R. Heteroatom doped reduced graphene oxide paper for large area perovskite solar cells. *Sol. Energy* **163**, 564–569 (2018).

135. Yu, J.-H., Lee, C.-H., Joh, H.-I., Yeo, J.-S. & Na, S.-I. Synergetic effects of solution-processable fluorinated graphene and PEDOT as a hole-transporting layer for highly efficient and stable normal-structure perovskite solar cells. *Nanoscale* **9**, 17167–17173 (2017).

136. Kakavelakis, G. *et al.* Extending the Continuous Operating Lifetime of Perovskite Solar Cells with a Molybdenum Disulfide Hole Extraction Interlayer. *Adv. Energy Mater.* **8**, 1702287 (2018).

137. Capasso, A. *et al.* Few-Layer $MoS_2$ Flakes as Active Buffer Layer for Stable Perovskite Solar Cells. *Adv. Energy Mater.* **6**, 1–12 (2016).

138. Li, H. *et al.* Enhancing Efficiency of Perovskite Solar Cells via Surface Passivation with Graphene Oxide Interlayer. *ACS Appl. Mater. Interfaces* **9**, 38967–38976 (2017).

139. Pazos-Outón, L. M. *et al.* Photon recycling in lead iodide perovskite solar cells. *Science (80-. ).* **351**, 1430 LP – 1433 (2016).

140. Conings, B. *et al.* Intrinsic Thermal Instability of Methylammonium Lead Trihalide Perovskite. *Adv. Energy Mater.* **5**, 1500477 (2015).

141. Supasai, T., Rujisamphan, N., Ullrich, K., Chemseddine, A. & Dittrich, T. Formation of a passivating CH3NH3PbI3/PbI2 interface during moderate heating of CH3NH3PbI3 layers. *Appl. Phys. Lett.* **103**, 183906 (2013).

142. Boyd, C. C. *et al.* Barrier Design to Prevent Metal-Induced Degradation and Improve Thermal Stability in Perovskite Solar Cells. *ACS Energy Lett.* **3**, 1772–1778 (2018).

143. Domanski, K. *et al.* Not All That Glitters Is Gold: Metal-Migration-Induced Degradation in Perovskite Solar Cells. *ACS Nano* **10**, 6306–6314 (2016).

144. Kato, Y. *et al.* Silver Iodide Formation in Methyl Ammonium Lead Iodide Perovskite Solar Cells with Silver Top Electrodes. *Adv. Mater. Interfaces* **2**, 1500195 (2015).

145. Leijtens, T. *et al.* Overcoming ultraviolet light instability of sensitized TiO2 with meso-superstructured organometal tri-halide perovskite solar cells. *Nat. Commun.* **4**, 2885 (2013).

146. Juarez-Perez, E. J. *et al.* Photodecomposition and thermal decomposition in methylammonium halide lead perovskites and inferred design principles to increase photovoltaic device stability. *J. Mater. Chem. A* **6**, 9604–9612 (2018).

147. Wang, Q. *et al.* Scaling behavior of moisture-induced grain degradation in polycrystalline hybrid perovskite thin films. *Energy Environ. Sci.* **10**, 516–522 (2017).

148. Zuo, L. *et al.* Tailoring the Interfacial Chemical Interaction for High-Efficiency Perovskite Solar Cells. *Nano Lett.* **17**, 269–275 (2017).

149. Agresti, A. *et al.* Graphene–Perovskite Solar Cells Exceed 18 % Efficiency: A Stability Study. *ChemSusChem* **9**, 2609–2619 (2016).

150. Yu, J. H., Lee, C. H., Joh, H. I., Yeo, J. S. & Na, S. I. Synergetic effects of solution-processable fluorinated graphene and PEDOT as a hole-transporting layer for highly

efficient and stable normal-structure perovskite solar cells. *Nanoscale* **9**, 17167–17173 (2017).

151. Kim, G. H. *et al.* Fluorine Functionalized Graphene Nano Platelets for Highly Stable Inverted Perovskite Solar Cells. *Nano Lett.* **17**, 6385–6390 (2017).

152. Liu, Y. *et al.* Carbon nanorods. *Chem. Phys. Lett.* **331**, 31–34 (2000).

153. Rakha, S. A., Yu, G., Cao, J., He, S. & Zhou, X. Diamond-graphite nanorods produced by microwave plasma chemical vapor deposition. *Diam. Relat. Mater.* **19**, 284–287 (2010).

154. Cai, J. *et al.* Atomically precise bottom-up fabrication of graphene nanoribbons. *Nature* **466**, 470 (2010).

155. Pachfule, P., Shinde, D., Majumder, M. & Xu, Q. Fabrication of carbon nanorods and graphene nanoribbons from a metal–organic framework. *Nat. Chem.* **8**, 718 (2016).

156. Tian, Y. *et al.* A facile route to synthesis of $MoS_2$ nanorods. *Mater. Lett.* **59**, 3452–3455 (2005).

157. Lin, H., Chen, X., Li, H., Yang, M. & Qi, Y. Hydrothermal synthesis and characterization of $MoS_2$ nanorods. *Mater. Lett.* **64**, 1748–1750 (2010).

158. Zhang, C., Wu, H. Bin, Guo, Z. & Lou, X. W. (David). Facile synthesis of carbon-coated $MoS_2$ nanorods with enhanced lithium storage properties. *Electrochem. commun.* **20**, 7–10 (2012).

159. Tang, G., Tang, H., Li, C., Li, W. & Ji, X. Surfactant-assisted hydrothermal synthesis and characterization of $WS_2$ nanorods. *Mater. Lett.* **65**, 3457–3460 (2011).

160. Wu, Y., Liu, Z., Chen, J., Cai, X. & Na, P. Hydrothermal fabrication of hyacinth flower-like $WS_2$ nanorods and their photocatalytic properties. *Mater. Lett.* **189**, 282–285 (2017).

161. Kumar, P., Singh, M., Gopal, P. & Reddy, G. B. Sulfurization of $WO_3$ nanorods into $WS_2$ as a function of $H_2S$/Ar partial pressure. *AIP Conf. Proc.* **1953**, 30252 (2018).

162. Zhang, L. L., Tu, J. P., Wu, H. M. & Yang, Y. Z. $WS_2$ nanorods prepared by self-transformation process and their tribological properties as additive in base oil. *Mater. Sci. Eng. A* **454–455**, 487–491 (2007).

163. Zhang, H. Z., Phillips, M. R., Fitz Gerald, J. D., Yu, J. & Chen, Y. Patterned growth and cathodoluminescence of conical boron nitride nanorods. *Appl. Phys. Lett.* **88**, 93117

(2006).

164. Zhang, H., FitzGerald, J. D., Chadderton, L. T., Yu, J. & Chen, Y. Growth and structure of prismatic boron nitride nanorods. *Phys. Rev. B* **74**, 45407 (2006).

165. Zhang, H., Yu, J., Chen, Y. & Fitz Gerald, J. Conical Boron Nitride Nanorods Synthesized Via the Ball-Milling and Annealing Method. *J. Am. Ceram. Soc.* **89**, 675–679 (2006).

166. Museur, L. *et al.* Picosecond laser structuration under high pressures: Observation of boron nitride nanorods. *J. Appl. Phys.* **104**, 93504 (2008).

167. Russo, P., Hu, A., Compagnini, G., Duley, W. W. & Zhou, N. Y. Femtosecond laser ablation of highly oriented pyrolytic graphite: a green route for large-scale production of porous graphene and graphene quantum dots. *Nanoscale* **6**, 2381–2389 (2014).

168. Paradisanos, I., Kymakis, E., Fotakis, C., Kioseoglou, G. & Stratakis, E. Intense femtosecond photoexcitation of bulk and monolayer $MoS_2$. *Appl. Phys. Lett.* **105**, 41108 (2014).

169. Chen, K. *et al.* Lateral Built-In Potential of Monolayer $MoS_2$–$WS_2$ In-Plane Heterostructures by a Shortcut Growth Strategy. *Adv. Mater.* **27**, 6431–6437 (2015).

170. Pan, D., Zhang, J., Li, Z. & Wu, M. Hydrothermal Route for Cutting Graphene Sheets into Blue-Luminescent Graphene Quantum Dots. *Adv. Mater.* **22**, 734–738 (2010).

171. Cui, Z. M., Jiang, S. P. & Li, C. M. Highly dispersed $MoO_x$ on carbon nanotube as support for high performance Pt catalyst towards methanol oxidation. *Chem. Commun.* **47**, 8418–8420 (2011).

172. Gao, Q., Zhao, X., Xiao, Y., Zhao, D. & Cao, M. A mild route to mesoporous Mo2C–C hybrid nanospheres for high performance lithium-ion batteries. *Nanoscale* **6**, 6151–6157 (2014).

173. Huang, H. *et al.* A facile, green, and solvent-free route to nitrogen–sulfur-codoped fluorescent carbon nanoparticles for cellular imaging. *RSC Adv.* **4**, 11872–11875 (2014).

174. Zhang, Y., Wang, Y., Guan, Y. & Feng, L. Uncovering the pKa dependent fluorescence quenching of carbon dots induced by chlorophenols. *Nanoscale* **7**, 6348–6355 (2015).

175. Ito, Y., Cong, W., Fujita, T., Tang, Z. & Chen, M. High Catalytic Activity of Nitrogen and Sulfur Co-Doped Nanoporous Graphene in the Hydrogen Evolution Reaction. *Angew.*

*Chemie Int. Ed.* **54**, 2131–2136 (2015).

176. Yang, J. *et al.* Two-dimensional hybrid nanosheets of tungsten disulfide and reduced graphene oxide as catalysts for enhanced hydrogen evolution. *Angew. Chemie - Int. Ed.* **52**, 13751–13754 (2013).

177. Polcar, T., Gustavsson, F., Thersleff, T., Jacobson, S. & Cavaleiro, A. Complex frictional analysis of self-lubricant W-S-C/Cr coating. *Faraday Discuss.* **156**, 383–401 (2012).

178. Rodella, C. B. *et al.* Physical and chemical studies of tungsten carbide catalysts: effects of Ni promotion and sulphonated carbon. *RSC Adv.* **5**, 23874–23885 (2015).

179. Yang, J. *et al.* Two-Dimensional Hybrid Nanosheets of Tungsten Disulfide and Reduced Graphene Oxide as Catalysts for Enhanced Hydrogen Evolution. *Angew. Chemie Int. Ed.* **52**, 13751–13754 (2013).

180. Ding, Q. *et al.* Basal-Plane Ligand Functionalization on Semiconducting 2H-$MoS_2$ Monolayers. *ACS Appl. Mater. Interfaces* **9**, 12734–12742 (2017).

181. Wan, S., Yu, Y., Pu, J. & Lu, Z. Facile fabrication of boron nitride nanosheets–amorphous carbon hybrid film for optoelectronic applications. *RSC Adv.* **5**, 19236–19240 (2015).

182. Sahoo, M., Sreena, K. P., Vinayan, B. P. & Ramaprabhu, S. Green synthesis of boron doped graphene and its application as high performance anode material in Li ion battery. *Mater. Res. Bull.* **61**, 383–390 (2015).

183. Zhang, C. *et al.* Synthesis of Nitrogen-Doped Graphene Using Embedded Carbon and Nitrogen Sources. *Adv. Mater.* **23**, 1020–1024 (2011).

184. Dhakal, K. P. *et al.* Confocal absorption spectral imaging of $MoS_2$: optical transitions depending on the atomic thickness of intrinsic and chemically doped $MoS_2$. *Nanoscale* **6**, 13028–13035 (2014).

185. Liu, H., Ansah Antwi, K. K., Ying, J., Chua, S. & Chi, D. Towards large area and continuous $MoS_2$ atomic layers via vapor-phase growth: thermal vapor sulfurization. *Nanotechnology* **25**, 405702 (2014).

186. Zhang, L. *et al.* Electronic structure and chemical bonding of a graphene oxide–sulfur nanocomposite for use in superior performance lithium–sulfur cells. *Phys. Chem. Chem. Phys.* **14**, 13670–13675 (2012).

187. Dieterle, M., Weinberg, G. & Mestl, G. Raman spectroscopy of molybdenum oxides Part I. Structural characterization of oxygen defects in MoO3−x by DR UV/VIS, Raman spectroscopy and X-ray diffraction. *Phys. Chem. Chem. Phys.* **4**, 812–821 (2002).

188. Manjunatha, S., Rajesh, S., Vishnoi, P. & Rao, C. N. R. Reaction with organic halides as a general method for the covalent functionalization of nanosheets of 2D chalcogenides and related materials. *J. Mater. Res.* **32**, 2984–2992 (2017).

189. Lei, Z., Xu, S., Wan, J. & Wu, P. Facile preparation and multifunctional applications of boron nitride quantum dots. *Nanoscale* **7**, 18902–18907 (2015).

190. Li, Y. *et al.* Measurement of the optical dielectric function of monolayer transition-metal dichalcogenides: ${\mathrm{MoS}}_{2}$, $\mathrm{Mo}\mathrm{S}{\mathrm{e}}_{2}$, ${\mathrm{WS}}_{2}$, and $\mathrm{WS}{\mathrm{e}}_{2}$. *Phys. Rev. B* **90**, 205422 (2014).

191. Lu, J. *et al.* Temperature-dependent Raman spectra of bamboo-like boron nitride nanotubes. *Appl. Phys. Express* **7**, 22401 (2014).

192. Kozawa, D. *et al.* Photocarrier relaxation pathway in two-dimensional semiconducting transition metal dichalcogenides. *Nat. Commun.* **5**, 4543 (2014).

193. Butler, S. Z. *et al.* Progress, Challenges, and Opportunities in Two-Dimensional Materials Beyond Graphene. *ACS Nano* **7**, 2898–2926 (2013).

194. Choi, W. *et al.* High-Detectivity Multilayer $MoS_2$ Phototransistors with Spectral Response from Ultraviolet to Infrared. *Adv. Mater.* **24**, 5832–5836 (2012).

195. Wu, J.-Y., Zhang, X.-Y., Ma, X.-D., Qiu, Y.-P. & Zhang, T. High quantum-yield luminescent $MoS_2$ quantum dots with variable light emission created via direct ultrasonic exfoliation of $MoS_2$ nanosheets. *RSC Adv.* **5**, 95178–95182 (2015).

196. Li, B. L. *et al.* Electrochemically induced Fenton reaction of few-layer $MoS_2$ nanosheets: preparation of luminescent quantum dots via a transition of nanoporous morphology. *Nanoscale* **6**, 9831–9838 (2014).

197. Wang, Y. *et al.* Electrochemical Control of Photoluminescence in Two-Dimensional $MoS_2$ Nanoflakes. *ACS Nano* **7**, 10083–10093 (2013).

198. Dai, W. *et al.* Tunable Fabrication of Molybdenum Disulfide Quantum Dots for

Intracellular MicroRNA Detection and Multiphoton Bioimaging. *Small* **11**, 4158–4164 (2015).

199. Wang, Z. *et al.* CTAB-assisted synthesis of single-layer $MoS_2$–graphene composites as anode materials of Li-ion batteries. *J. Mater. Chem. A* **1**, 2202–2210 (2013).

200. Vattikuti, S. V. P. & Byon, C. Synthesis and Characterization of Molybdenum Disulfide Nanoflowers and Nanosheets: Nanotribology. *J. Nanomater.* **2015**, 710462 (2015).

201. Li, D., Müller, M. B., Gilje, S., Kaner, R. B. & Wallace, G. G. Processable aqueous dispersions of graphene nanosheets. *Nat. Nanotechnol.* **3**, 101–105 (2008).

202. Pandey, S. *et al.* Carbon dots functionalized gold nanorod mediated delivery of doxorubicin: tri-functional nano-worms for drug delivery, photothermal therapy and bioimaging. *J. Mater. Chem. B* **1**, 4972–4982 (2013).

203. Podila, R., Vedantam, P., Ke, P. C., Brown, J. M. & Rao, A. M. Evidence for Charge-Transfer-Induced Conformational Changes in Carbon Nanostructure–Protein Corona. *J. Phys. Chem. C* **116**, 22098–22103 (2012).

204. Gopalakrishnan, D. *et al.* Electrochemical synthesis of luminescent $MoS_2$ quantum dots. *Chem. Commun.* **51**, 6293–6296 (2015).

205. Zhang, Z., Zhang, J., Chen, N. & Qu, L. Graphene quantum dots: an emerging material for energy-related applications and beyond. *Energy Environ. Sci.* **5**, 8869–8890 (2012).

206. Štengl, V., Tolasz, J. & Popelková, D. Ultrasonic preparation of tungsten disulfide single-layers and quantum dots. *RSC Adv.* **5**, 89612–89620 (2015).

207. Pal, S., Tadi, K. K., Sudeep, P. M., Radhakrishnan, S. & Narayanan, T. N. Temperature assisted shear exfoliation of layered crystals for the large-scale synthesis of catalytically active luminescent quantum dots. *Mater. Chem. Front.* **1**, 319–325 (2017).

208. Lin, L. *et al.* Fabrication and Luminescence of Monolayered Boron Nitride Quantum Dots. *Small* **10**, 60–65 (2014).

209. Kumar, V., Nikhil, K., Roy, P., Lahiri, D. & Lahiri, I. Emergence of fluorescence in boron nitride nanoflakes and its application in bioimaging. *RSC Adv.* **6**, 48025–48032 (2016).

210. Li, X. *et al.* Flexible metal-semiconductor-metal device prototype on wafer-scale thick boron nitride layers grown by MOVPE. *Sci. Rep.* **7**, 786 (2017).

211. Schneider, C. A., Rasband, W. S. & Eliceiri, K. W. NIH Image to ImageJ: 25 years of image analysis. *Nat. Methods* **9**, 671–675 (2012).

212. Siokou, A. *et al.* Surface refinement and electronic properties of graphene layers grown on copper substrate: An XPS, UPS and EELS study. *Appl. Surf. Sci.* **257**, 9785–9790 (2011).

213. Zheng, J. *et al.* Production of Graphite Chloride and Bromide Using Microwave Sparks. *Sci. Rep.* **2**, 662 (2012).

214. Savastano, M. *et al.* Iodide and triiodide anion complexes involving anion–π interactions with a tetrazine-based receptor. *Dalt. Trans.* **46**, 4518–4529 (2017).

215. Li, Q. *et al.* Cooperativity between the halogen bond and the hydrogen bond in H3N...XY...HF complexes (X, Y=F, Cl, Br). *Chemphyschem* **9**, 2265–2269 (2008).

216. Li, B. *et al.* Photochemical Chlorination of Graphene. *ACS Nano* **5**, 5957–5961 (2011).

217. Mishra, A., Singh, V. K. & Mohanty, T. Coexistence of interfacial stress and charge transfer in graphene oxide-based magnetic nanocomposites. *J. Mater. Sci.* **52**, 7677–7687 (2017).

218. Shen, B., Chen, J., Yan, X. & Xue, Q. Synthesis of fluorine-doped multi-layered graphene sheets by arc-discharge. *RSC Adv.* **2**, 6761–6764 (2012).

219. Karlický, F., Kumara Ramanatha Datta, K., Otyepka, M. & Zbořil, R. Halogenated Graphenes: Rapidly Growing Family of Graphene Derivatives. *ACS Nano* **7**, 6434–6464 (2013).

220. Yoshimitsu, Z., Nakajima, A., Watanabe, T. & Hashimoto, K. Effects of Surface Structure on the Hydrophobicity and Sliding Behavior of Water Droplets. *Langmuir* **18**, 5818–5822 (2002).

221. Ouellette, R. J. & Rawn, J. D. 2 - Properties of Organic Compounds. in (eds. Ouellette, R. J. & Rawn, J. D. B. T.-P. of O. C.) 33–64 (Elsevier, 2015).

222. Papirer, E., Lacroix, R., Donnet, J.-B., Nansé, G. & Fioux, P. XPS study of the halogenation of carbon black—Part 2. Chlorination. *Carbon N. Y.* **33**, 63–72 (1995).

223. Zheng, Q. & Lü, C. Size Effects of Surface Roughness to Superhydrophobicity. *Procedia IUTAM* **10**, 462–475 (2014).

224. Colella, S. *et al.* MAPbI3-xClx mixed halide perovskite for hybrid solar cells: The role of chloride as dopant on the transport and structural properties. *Chem. Mater.* **25**, 4613–4618 (2013).

225. Jiao, Y. *et al.* Graphene-covered perovskites: an effective strategy to enhance light absorption and resist moisture degradation. *RSC Adv.* **5**, 82346–82350 (2015).

226. Zhu, Z. *et al.* Efficiency enhancement of perovskite solar cells through fast electron extraction: The role of graphene quantum dots. *J. Am. Chem. Soc.* **136**, 3760–3763 (2014).

227. Burschka, J. *et al.* Tris(2-(1H-pyrazol-1-yl)pyridine)cobalt(III) as p-Type Dopant for Organic Semiconductors and Its Application in Highly Efficient Solid-State Dye-Sensitized Solar Cells. *J. Am. Chem. Soc.* **133**, 18042–18045 (2011).

228. Leijtens, T., Lim, J., Teuscher, J., Park, T. & Snaith, H. J. Charge Density Dependent Mobility of Organic Hole-Transporters and Mesoporous TiO2 Determined by Transient Mobility Spectroscopy: Implications to Dye-Sensitized and Organic Solar Cells. *Adv. Mater.* **25**, 3227–3233 (2013).

229. Meng, G. *et al.* Theoretical insight into the carrier mobility anisotropy of hole transport material Spiro-OMeTAD. *Curr. Appl. Phys.* **17**, 1316–1322 (2017).

230. Taguchi, Y. *et al.* Polyyne formation by ns and fs laser induced breakdown in hydrocarbon gas flow. *Carbon N. Y.* **115**, 169–174 (2017).

231. Miura, K. Nanowire formation under femtosecond laser radiation in liquid. in (ed. Hirao, K.) Ch. 18 (IntechOpen, 2011). doi:10.5772/17720

232. Seideman, T. Revival Structure of Aligned Rotational Wave Packets. *Phys. Rev. Lett.* **83**, 4971–4974 (1999).

233. Seideman, T. On the dynamics of rotationally broad, spatially aligned wave packets. *J. Chem. Phys.* **115**, 5965–5973 (2001).

234. Stapelfeldt, H. & Seideman, T. Colloquium: Aligning molecules with strong laser pulses. *Rev. Mod. Phys.* **75**, 543–557 (2003).

235. Chatterley, A. S. *et al.* Long-lasting field-free alignment of large molecules inside helium nanodroplets. doi:10.1038/s41467-018-07995-0

236. Remskar, M. *et al.* Self-Assembly of Subnanometer-Diameter Single-Wall MoS&lt;sub&gt;2&lt;/sub&gt; Nanotubes. *Science (80-. ).* **292**, 479 LP – 481 (2001).

237. Wang, F. *et al.* Strain-induced phonon shifts in tungsten disulfide nanoplatelets and nanotubes. *2D Mater.* **4**, 15007 (2016).

238. Zhao, W. *et al.* Lattice dynamics in mono- and few-layer sheets of $WS_2$ and $WSe_2$. *Nanoscale* **5**, 9677–9683 (2013).

239. Reshmi, S. *et al.* Tailored $MoS_2$ nanorods: a simple microwave assisted synthesis. *Mater. Res. Express* **4**, 115012 (2017).

240. Yang, L. *et al.* Lattice strain effects on the optical properties of $MoS_2$ nanosheets. *Sci. Rep.* **4**, 5649 (2014).

241. Kiriya, D., Tosun, M., Zhao, P., Kang, J. S. & Javey, A. Air-Stable Surface Charge Transfer Doping of $MoS_2$ by Benzyl Viologen. *J. Am. Chem. Soc.* **136**, 7853–7856 (2014).

242. Wang, S. *et al.* Shape Evolution of Monolayer $MoS_2$ Crystals Grown by Chemical Vapor Deposition. *Chem. Mater.* **26**, 6371–6379 (2014).

243. Ibrahim, K. H. *et al.* A Novel Femtosecond Laser-Assisted Method for the Synthesis of Reduced Graphene Oxide Gels and Thin Films with Tunable Properties. *Adv. Mater. Interfaces* **3**, 1500864 (2016).

244. Li, H. *et al.* Tuning the Chemical Hardness of Boron Nitride Nanosheets by Doping Carbon for Enhanced Adsorption Capacity. *ACS Omega* **2**, 5385–5394 (2017).

245. Liu, Q. *et al.* Stable Metallic 1T-$WS_2$ Nanoribbons Intercalated with Ammonia Ions: The Correlation between Structure and Electrical/Optical Properties. *Adv. Mater.* **27**, 4837–4844 (2015).

246. Piao, M. *et al.* Hydrothermal synthesis of stable metallic 1T phase $WS_2$ nanosheets for thermoelectric application. *Nanotechnology* **29**, 25705 (2017).

247. Cheng, Y. *et al.* Passive Q-switching of a diode-pumped Pr:LiYF4 visible laser using $WS_2$ as saturable absorber. in *Advanced Solid State Lasers* ATh2A.10 (Optical Society of America, 2015). doi:10.1364/ASSL.2015.ATh2A.10

248. Wang, S. *et al.* Synthesis and Characterization of Cobalt-Doped $WS_2$ Nanorods for Lithium Battery Applications. *Nanoscale Res. Lett.* **5**, 1301 (2010).

249. Xu, F. *et al.* Multi-walled carbon/IF-$WS_2$ nanoparticles with improved thermal properties. *Nanoscale* **5**, 10504–10510 (2013).

250. Balendhran, S. *et al.* Atomically thin layers of $MoS_2$ via a two step thermal evaporation–exfoliation method. *Nanoscale* **4**, 461–466 (2012).

251. Xiong, J. *et al.* Carbon-doped porous boron nitride: metal-free adsorbents for sulfur removal from fuels. *J. Mater. Chem. A* **3**, 12738–12747 (2015).

252. Yuan, S. *et al.* Pure &amp; crystallized 2D Boron Nitride sheets synthesized via a novel process coupling both PDCs and SPS methods. *Sci. Rep.* **6**, 20388 (2016).

253. Bergin, S. M. *et al.* The effect of nanowire length and diameter on the properties of transparent, conducting nanowire films. *Nanoscale* **4**, 1996–2004 (2012).

254. Liu, C.-H. & Yu, X. Silver nanowire-based transparent, flexible, and conductive thin film. *Nanoscale Res. Lett.* **6**, 75 (2011).

255. Zeng, L. *et al.* High-responsivity UV-Vis Photodetector Based on Transferable $WS_2$ Film Deposited by Magnetron Sputtering. *Sci. Rep.* **6**, 20343 (2016).

256. Ma, R. *et al.* Direct Four-Probe Measurement of Grain-Boundary Resistivity and Mobility in Millimeter-Sized Graphene. *Nano Lett.* **17**, 5291–5296 (2017).

257. Parvez, K., Li, R. & Müllen, K. Graphene as Transparent Electrodes for Solar Cells. *Nanocarbons for Advanced Energy Conversion* (2015). doi:doi:10.1002/9783527680016.ch10

258. Osica, I. *et al.* Fabrication of Silica-Protein Hierarchical Nanoarchitecture with Gas-Phase Sensing Activity. *J. Nanosci. Nanotechnol.* **17**, 5908–5917 (2017).

259. Hellstern, T. R. *et al.* Investigating Catalyst–Support Interactions To Improve the Hydrogen Evolution Reaction Activity of Thiomolybdate [Mo3S13]2– Nanoclusters. *ACS Catal.* **7**, 7126–7130 (2017).

260. Cho, S.-Y. *et al.* Highly Enhanced Gas Adsorption Properties in Vertically Aligned $MoS_2$ Layers. *ACS Nano* **9**, 9314–9321 (2015).

261. Ting, L. R. L. *et al.* Catalytic Activities of Sulfur Atoms in Amorphous Molybdenum Sulfide for the Electrochemical Hydrogen Evolution Reaction. *ACS Catal.* **6**, 861–867 (2016).

262. Šljukić, B., Banks, C. E. & Compton, R. G. Iron Oxide Particles Are the Active Sites for

Hydrogen Peroxide Sensing at Multiwalled Carbon Nanotube Modified Electrodes. *Nano Lett.* **6**, 1556–1558 (2006).

263. Sanchez Esqueda, I. *et al.* Aligned Carbon Nanotube Synaptic Transistors for Large-Scale Neuromorphic Computing. *ACS Nano* **12**, 7352–7361 (2018).

264. Xiao, M., Shen, D., Musselman, K. P., Duley, W. W. & Zhou, Y. N. Oxygen vacancy migration/diffusion induced synaptic plasticity in a single titanate nanobelt. *Nanoscale* **10**, 6069–6079 (2018).

265. Xiao, M. *et al.* Ultrathin TiOx Interface-Mediated ZnO-Nanowire Memristive Devices Emulating Synaptic Behaviors. *Adv. Electron. Mater.* **5**, 1900142 (2019).

266. Singh, E., Singh, P., Kim, K. S., Yeom, G. Y. & Nalwa, H. S. Flexible Molybdenum Disulfide ($MoS_2$) Atomic Layers for Wearable Electronics and Optoelectronics. *ACS Appl. Mater. Interfaces* **11**, 11061–11105 (2019).

## Publications

### Refereed journals

1. **Khaled H Ibrahim**, Novodchuk, I., Mistry, K., Singh, M., Ling, C., Sanderson, J., Bajcsy, M., Yavuz, M., Musselman, K. P., Laser-Directed Assembly of Nanorods of 2D Materials. *Small* 2019, 1904415.
2. **Khaled H. Ibrahim**, Kevin Musselman, and Mustafa Yavuz. *"Research Update: Beyond graphene—Synthesis of functionalized quantum dots of 2D materials and their applications"* **APL Materials** 6, 120701 (2018); https://doi.org/10.1063/1.5067250.
3. I Novodchuk, M Irannejad, B Wales, **Khaled Ibrahim**, J Sanderson, M Bajcsy, M Yavuz. "*Controlled volume production of simultaneously B/N co-doped reduced graphene oxide nanoflakes using femtosecond laser ablation"* Materials Research Bulletin, November 2018, https://doi.org/10.1016/j.materresbull.2018.10.039
4. Abdullah H. Alshehri, **Khaled H. Ibrahim**, Kissan Mistry, Viet Nguyen, David Muñoz-Rojas, Mustafa Yavuz, Kevin P. Musselman. "*Quantum-Tunneling Metal-Insulator-Metal Diodes Made by Rapid Atmospheric Pressure Chemical Vapor Deposition"* **Advanced Functional Materials**, Volume29, Issue7, February 14, 2019, 1805533
5. **Khaled Ibrahim**, Mehrdad Irannejad, Benji Wales, Joe Sanderson, Mustafa Yavuz, Kevin Musselman. *"Simultaneous Fabrication and Functionalization of Nanoparticles of Two-Dimensional Materials with Hybrid Optical Properties"* **Advanced Optical Materials**, Accepted 23 February 28, 2018 In press with Communication, No. adom.201701365R1.
6. **Khaled H Ibrahim,** Mehrdad Irannejad, Benji Wales, Joseph Sanderson, Kevin Musselman, Mustafa Yavuz. *"The effect of varying ultrafast pulse laser energies on the electrical properties of reduced graphene oxide sheets in solution."* **Journal of Electronic Materials**. October 2017. DOI: https://doi.org/10.1007/s11664-017-5866-1
7. Abdallah El Shehri, Nelson Fitzpatrick , **K.H.Ibrahim**, Mustafa Yavuz, K. Musselman, *"A Simple Plasma Assisted Atomic Layer Deposition (PAALD) Technique for High Substitutional Nitrogen Doping of TiO2"* **Journal of Vacuum Science and Technology** Accepted and in press 26 February 2018. Article number: JVSTA-A-17-435R
8. **Khaled H. Ibrahim**, M. Irannejad, Mojtaba H., Ali Ramadhan, Kevin P. Musselman, Joseph Sanderson, and Mustafa Yavuz, (2016) *A novel femtosecond laser assisted method for the synthesis of reduced graphene oxide gel and thin films with tunable properties*. **Advanced Materials Interfaces**. Volume 3, Issue 14 .DOI: 10.1002/admi.201500864.
9. D.Alsaedi, M.Irannejad , **K.H.Ibrahim**, A.AlMutairi, K. Musselman, O.Rahami, M.Yavuz, 2017,*"High-Responsivity Reduced Graphene Oxide Gel Photodetector for Visible-Light Detection with Large Detection Area and End-Contact Interface".* **Journal of Materials Chemistry C**. J. Mater. Chem. C, 2017,5, 882-888. DOI: 10.1039/C6TC04784J
10. **Khaled Ibrahim**, Mehrdad Irannejad, Wadha Alyalak, Ali Ramadhan, Joe Sanderson, Bo Cui, Andrew Brzezinski, Mustafa Yavuz. *"Ultrafast light interaction with Graphene oxide aqueous solution.* (2014) **IEEE** 14th International Conference in Nanotechnology. Pages 800-801, DOI: 10.1109/NANO.2014.6968088.
11. D.Alsaedi, M.Irannejad , **K.H.Ibrahim**, A.AlMutairi, K. Musselman, O.Rahami, M.Yavuz, 2017 *"**High Operation Stability and Different Sensing Mechanisms in Graphene Oxide Gel Photodetectors Utilizing Thin Polymeric layer**".* Under review, **APL Materials** with submission number:#APL18-AR-00047.
12. Inna Novodchuk; Muhammed Kayaharman; Sahr Al-Tuairqi; **Khaled Ibrahim**; Mehrdad Irannejad; Eihab Abdel-Rahman; Joseph Sanderson; Michal Bajcsy; Mustafa Yavuz B/N co-doped graphene oxide gel with extremely-high mobility and ION/IOFF for large-area field effect transistors, **Carbon** 2019, In Press, with submission number CARBON-D-19-03634.